Searching for High Energy Neutrinos with the AMANDA-II detector

by

Jodi Ann Cooley-Sekula

A dissertation submitted in partial fulfillment of the

requirements for the degree of

Doctor of Philosophy

(Physics)

at the

University of Wisconsin – Madison

2003

Searching for High Energy Neutrinos with the AMANDA-II detector

Jodi Ann Cooley-Sekula

Under the supervision of Professor Albrecht Karle

At the University of Wisconsin — Madison

The Antarctic Muon and Neutrino Detector Array (AMANDA) is designed to detect high energy neutrinos from extragalactic sources. It uses the south polar ice cap as both a target and medium for detecting Cherenkov radiation from the charged particles left after a neutrino collides with a nucleus.

Many models predict a flux of neutrinos from diffuse extragalactic sources (such as active galactic nuclei). In this work, a search is performed in data taken during the austral winter of 2000 by the AMANDA detector. The search finds 4 events on a predicted background of 3.26 events. Therefore, for an assumed E^{-2} spectrum a 90% classical confidence belt upper limit on the flux is set at $4.8 \times 10^{-7}\,\mathrm{cm}^{-2}\,\mathrm{s}^{-1}\,\mathrm{sr}^{-1}\,\mathrm{GeV}$ for neutrinos in the energy range 12-2000 TeV. This is currently the most stringent limit placed on this flux by any experiment.

Albrecht Karle (Adviser)

To Mom and Dad who inspired me to dream.

Acknowledgments

This work would not be possible without years of support and help from many people whom I am proud to acknowledge. First, I'd like to thank my adviser Albrecht Karle, who has offered me guidance, supported me through my years at the University of Wisconsin and believed in me.

I would also like to thank the members of the AMANDA collaboration who have built and maintained the experiment.

Closer to home, I would like to thank the "penguins" group who not only offered their support and useful suggestions, but became good friends. I would especially like to thank Gary Hill for his infinite motivation and patience, never giving up on me, and always offering his help and support. I would also like to thank Paolo Desiati for all expertise and encouragement. Of course, I can not forget to acknowledge Bob Morse for keeping the whole thing running, Francis Halzen for his motivation and eternal excitement, and Darryn Schneider for keeping the computers running.

With all my heart I would like to thank my parents, Richard and Ann "Tootie" Cooley and my siblings, Jackie, Jerry, and Jolene Cooley. Their love, support, and encouragement has kept me moving toward my dreams ever since I

was a child.

Finally, I would like to thank my husband, Steve Sekula who puts up with it all and still has time to inspire me.

Contents

List of Tables

List of Figures

Chapter 1

Introduction

Mankind has long looked with curiosity at the night sky. Stars and planets provided not only a source of myths, but also served as valuable navigational tools. This is likely the reason astronomy is among the oldest of sciences.

Up until the turn of the twentieth century, the only means of observing the sky was with photons at optical wavelengths. During the twentieth century photon astronomy expanded to new wavelengths. Modern astronomy looks at the sky in every band from radio waves to gamma rays. These new ways of seeing the universe paved the way for discovery. New objects and undreamed phenomena, such as pulsars, active galaxies, gamma ray bursts, and more were revealed.

A defining development for astronomy came in 1912 when Victor Hess discovered cosmic rays. This led to the use of protons and other nuclei as messengers from space. These new messengers brought with them a whole host of questions such as concerning their origin and the mechanism that accelerates them. These questions still puzzle scientists today.

In the past decades a new particle, the neutrino, has lent itself to probing

solutions to these questions. As messengers from space, neutrinos have advantages over photons and cosmic rays since they are not absorbed or deflected at high energies. The distance a photon can travel through space falls quickly at PeV energies as its mean free path length is limited to the Mpc scale [1] while cosmic rays are deflected by magnetic fields as they travel through space.

The idea of using oceans as sites for large neutrino detector date back to the 1960s [2, 3, 4]. Early attempts to use neutrinos as messengers from space started with the DUMAND project [5] in 1975. At the time of this thesis, there were three operational neutrino telescopes (ANTARES, AMANDA-II, and Baikal) and two neutrino telescopes in the development and prototyping stage, IceCube and NESTOR.

Much time and care has gone into understanding how to calibrate and analyze the data from the AMANDA experiment. These analyses have been the topic of many theses and papers. The first result, a glimpse of the atmospheric neutrino spectrum as seen by the AMANDA detector, was published in a letter to Nature in 2000 [6]. Since that time, AMANDA has further established itself as a landmark scientific experiment and has published results of analyses on neutrino point sources [7], diffuse flux muon and electron neutrinos [8, 9], WIMPs [10], and supernova [11].

This work has helped to pave the way for the topic of this thesis: the first search for muon neutrinos from diffuse astronomical sources with the AMANDA-II detector.

Chapter 2

High Energy Neutrino Physics and Astrophysics

2.1 Cosmic Rays

Cosmic rays are perhaps one of the oldest, most puzzling creatures known to Man. They are known to consist of mostly protons and also heavier atomic nuclei, yet their origin is not yet fully understood. However, it is clear that nearly all cosmic rays come from outside the solar system, but from within the galaxy. The most prevalent theory is that most cosmic rays are accelerated by supernovae explosions. The case for supernovae explosions is strengthened by the realization that the first order Fermi acceleration at a strong shock naturally produces a spectrum of cosmic rays consistent with what is observed.

The energy spectrum of cosmic rays is well described by the power-law

$$\frac{dN}{dE} \propto E^{-\alpha} \tag{2.1}$$

where α is the spectral power index. The value of the spectral index is constant

at $\alpha = 2.7$ for most energies. However, around 3 PeV, the region known as "the knee", the slope steepens to a value of $\alpha = 3.0$. Observations above 5 EeV, the region known as "the ankle", indicate a flatter spectrum. Figure 2.1 shows the differential energy spectrum of cosmic rays.

The same engines that produce the highest energy cosmic rays may also produce neutrinos. Hence, the search for the origin of the highest energy cosmic rays and the search for high energy neutrinos are intimately related.

2.1.1 Fermi Acceleration

Fermi acceleration [13, 14] is commonly accepted as the most plausible explanation for the particle acceleration as it can reproduce the observed spectrum of cosmic rays. The acceleration of particles to non-thermal energies takes place in supersonic shock waves. These accelerated particles are theorized to be present in supernovae, jets produced by active galactic nuclei (AGN), and other violent astronomical objects.

Particles gain energy in Fermi acceleration through the transfer of kinetic energy from shocked material in repeated "encounters" with the material. First-order Fermi acceleration describes the interaction of particles with a plane shock front, while second-order Fermi acceleration describes interactions of particles with moving clouds of plasma. These scenarios are illustrated in Fig. 2.2 and Fig 2.3. The main difference between the two cases is that in second-order Fermi acceleration particles can gain or lose energy in a given encounter. However, after many encounters there is a net gain in second-order Fermi acceleration. The

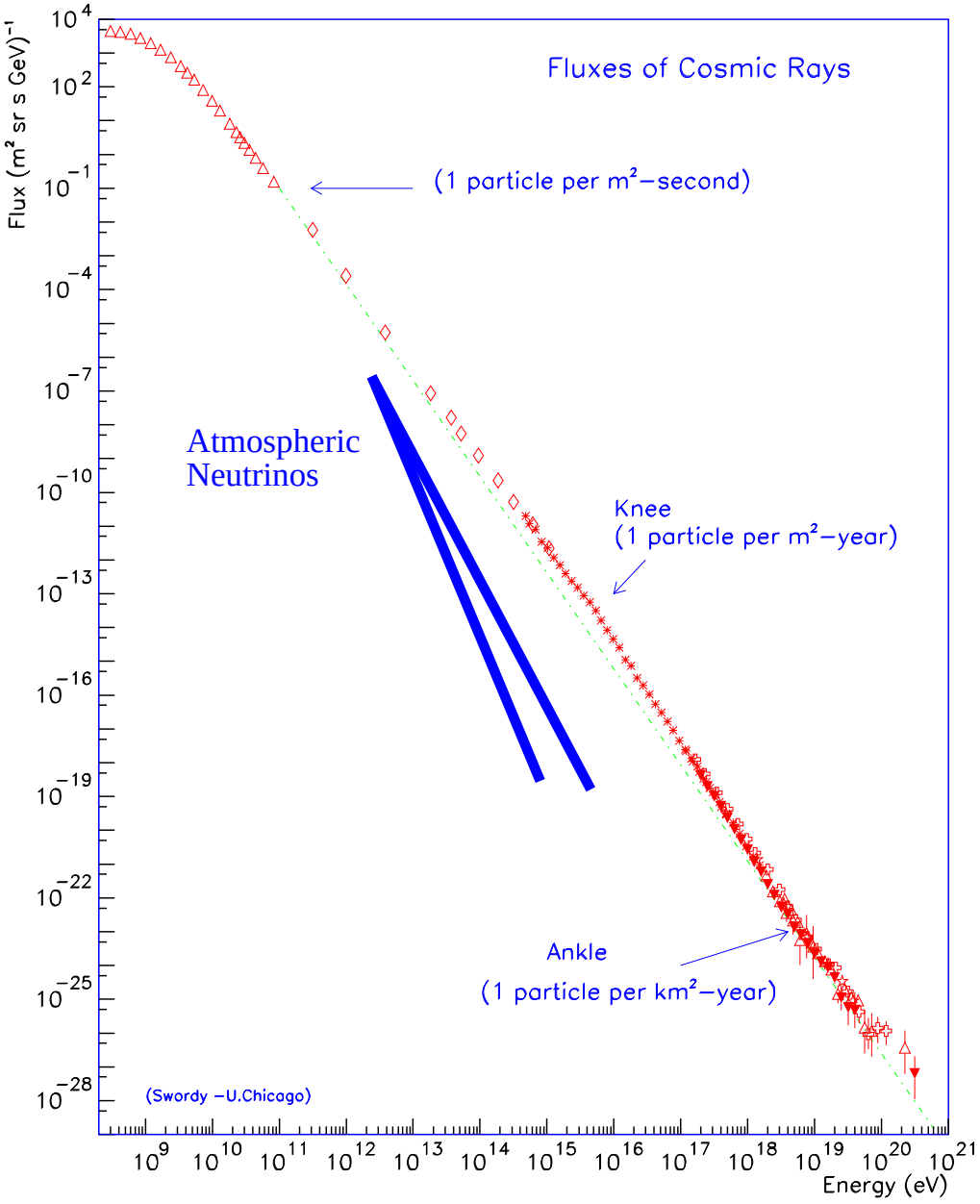

Figure 2.1: The cosmic ray spectrum adapted from [12].

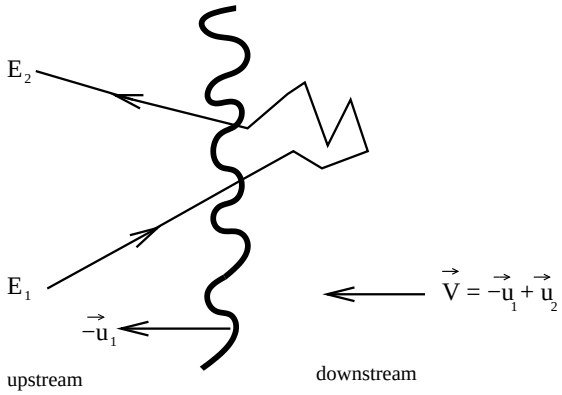

Figure 2.2: First order Fermi acceleration by a plane shock front. Adapted from [15].

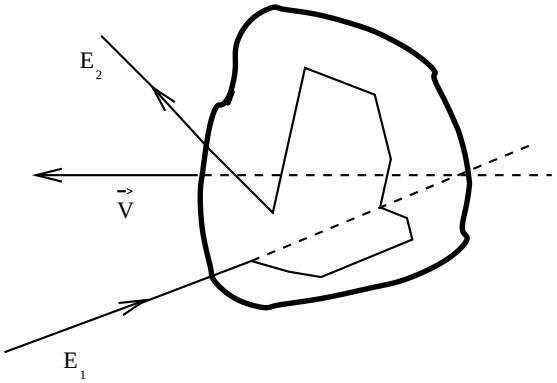

Figure 2.3: Second order Fermi acceleration by moving, partially ionized gas cloud. Adapted from [15].

following derivation for first-order Fermi acceleration follows that given in [15].

Consider a relativistic particle with energy E_1 that encounters a plane shock front at an angle θ_1 as shown in Fig 2.2. In the rest frame of the shock, the particle has an energy

$$E_1^{'} = \Gamma E_1(1 - \beta \cos\theta_1) \tag{2.2}$$

where Γ and $\beta \equiv V/c$ are the Lorentz factor and velocity of the shock respectively and the primes denote the quantities measured in the frame moving with the

shock. Transforming the energy to the rest frame of the particle gives

$$E_2 = \Gamma E_2^{'}(1 + \beta \cos\theta_2^{'}). \tag{2.3}$$

Since magnetic fields in the shock field produce elastic scattering, $E_2^{'} = E_1^{'}$. Thus, the energy change, ΔE, for the encounter described by θ_1 and θ_2 is given by

$$\frac{\Delta E}{E_1} = \frac{1 - \beta\cos\theta_1 + \beta\cos\theta_2^{'} - \beta^2\cos\theta_1\cos\theta_2^{'}}{1 - \beta^2} - 1. \tag{2.4}$$

Averaging over $\cos\theta_1$ and $\cos\theta_2^{'}$ gives $\Delta E \sim (4/3)\beta E_1 = \epsilon E_1$. Thus, a particle encountering a shock increases its energy in proportion to its original energy. After n encounters, the particle's energy is given by

$$E_n = E_0(1 + \epsilon)^n \tag{2.5}$$

where E_0 is the energy of the particle before the encounter. The number of particles to reach an energy E is then given by

$$n = \frac{\log\frac{E}{E_0}}{1 + \epsilon}. \tag{2.6}$$

If the probability of particles escaping the acceleration region is given by P_{esc}, then after n encounters the escape probability is given by

$$P_n = (1 - P_{esc})^n. \tag{2.7}$$

The number of particles accelerated to energies greater than E is then

$$N(> E) \propto \sum_{m=n}^{\infty}(1 - P_{esc})^m = \frac{(1 - P_{esc})^n}{P_{esc}}. \tag{2.8}$$

Substituting n gives

$$N(>E) \propto \frac{1}{P_{esc}} \left(\frac{E}{E_0}\right)^{-\gamma} \tag{2.9}$$

where

$$\gamma = \frac{log\frac{1}{1-P_{esc}}}{log1+\epsilon}. \tag{2.10}$$

For a differential spectrum equation 2.9 takes the form

$$\frac{dN}{dE} \propto \frac{1}{\gamma}\frac{1}{P_{esc}} \left(\frac{E}{E_0}\right)^{-(\gamma+1)} \tag{2.11}$$

As shown in [15] for shock fronts the spectral index can be approximated as

$$\gamma = 1 + \frac{4}{M^2} \tag{2.12}$$

where M = the Mach number $\gg 1$. In this case, the spectral index tends to $\gamma \sim 1$ which corresponds to a differential index of $(\gamma + 1) \sim 2$ at the source. Neutrinos that result from Fermi accelerated protons/pions are expected to have this energy spectrum, E^{-2}, when they reach the earth.

This simplified derivation uses the test particle assumption, meaning the particles being accelerated did not affect the conditions in the acceleration region. More detailed calculations can result in $\gamma \approx 2.0 - 2.4$. Taking into account the known energy-dependent leakage of cosmic rays out of the galaxy modifies the spectrum by $\delta\gamma$ of 0.3 to 0.6. This leads to a final spectral index for first order Fermi accelerations is $\gamma \sim 2.7$ for cosmic rays [15].

2.2 Neutrinos as a Source of Information

The universe has been explored throughout the electromagnetic spectrum, from radio waves to high energy gamma rays. However, it has not been until recently that we have been able to examine the universe with a new particle, the neutrino.

The advantages of using neutrinos as information carriers is demonstrated in Fig. 2.4. Foremost, neutrinos are not absorbed at high energies by ambient matter or photon fields like their photon counterparts. Photon absorption happens at the Mpc scale [1] and is the limiting adversary faced by gamma ray astronomy. Secondly, unlike cosmic rays, which are deflected by magnetic fields as they travel through space, neutrinos always point directly back to their source.

Astrophysical sources produce high energy gamma rays primarily by radiative processes from accelerated electrons, such as Compton scattering and synchrotron radiation, as well as the decay of pions:

$$\begin{aligned} p + \gamma &\longrightarrow p + \pi^0 \\ &\longmapsto 2\gamma. \end{aligned} \tag{2.13}$$

In contrast, neutrinos are produced via hadronic processes. The primary sources of these neutrinos are through the decay of pions and kaons:

$$\begin{aligned} p + X &\longrightarrow \pi^{\pm} + Y \\ &\longmapsto \mu^{\pm} + \nu_{\mu}\,(\bar{\nu_{\mu}}) \\ &\longmapsto e^{\pm} + \nu_e(\bar{\nu}_e) + \bar{\nu}_{\mu}(\nu_{\mu}) \end{aligned} \tag{2.14}$$

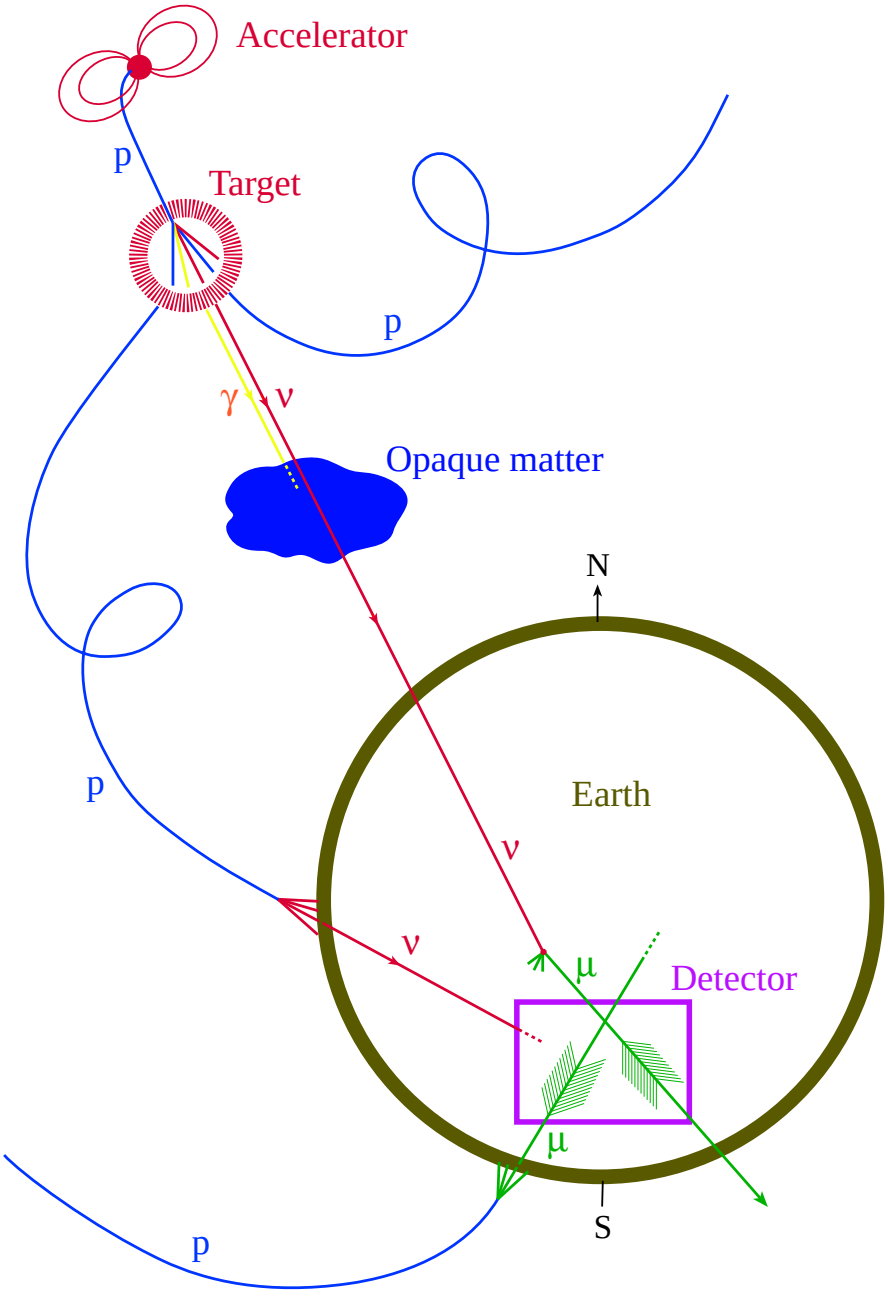

Figure 2.4: Neutrinos can travel from greater distances than photons because they are not absorbed by ambient matter or photon fields. Furthermore, neutrinos are not deflected by magnetic fields and always point directly back to their source, unlike cosmic rays [16].

$$\begin{aligned} p + X &\longrightarrow K^{\pm} + Y \\ &\longmapsto \mu^{\pm} + \nu_{\mu}(\bar{\nu}_{\mu}) \\ &\longmapsto e^{\pm} + \nu_e(\bar{\nu}_e) + \bar{\nu}_{\mu}(\nu_{\mu}) \end{aligned} \tag{2.15}$$

$$\begin{aligned} p + X &\longrightarrow K^0_L + Y \\ &\longmapsto \pi^{\pm} + \mu^{\pm} + \nu_{\mu}(\bar{\nu}_{\mu}). \\ &\longmapsto \pi^{\pm} + e^{\pm} + \nu_e(\bar{\nu}_e) \end{aligned} \tag{2.16}$$

Hence, high energy astronomy has the ability to differentiate between hadronic and electronic models of gamma ray emitters such as supernovae remnants, gamma ray bursts, or active galactic nuclei.

2.3 Expected Sources of Astronomical High Energy Neutrinos

2.3.1 The Atmosphere

Atmospheric neutrinos are produced in abundance in Earth's upper atmosphere. These neutrinos have energies that span a few MeV up to the highest energy cosmic rays. They serve as both a background and calibration beam in the search for extraterrestrial neutrinos.

Cosmic rays constantly bombard Earth's atmosphere, producing extensive air-showers when they interact with nuclei in the air. At the energies relevant to the AMANDA detector, cosmic rays consist of protons and helium nuclei with

some contributions from heavier nuclei. The spectrum of cosmic rays follows a power law, $E^{-2.7}$, in the energy range of interest for AMANDA.

Cosmic ray nuclei interact producing new particles, such as pions and kaons. Neutrinos arise primarily from the decay of these pions and kaons as described by equations 2.14 - 2.16. These neutrinos are referred to as atmospheric neutrinos because of their origin. The atmospheric neutrino spectrum follows a power law of $E^{-3.7}$, which is steeper than that of the cosmic rays they come from as shown in fig 2.1. The reason for this is that at high energies, pions tend to interact more often than they decay.

Another reaction that can create neutrinos in the atmosphere is the decay of charm particles, primarily D mesons. Charmed particles have a short lifetime. Consequently, the neutrinos that arise from these decays are referred to as *prompt neutrinos*. Prompt neutrinos constitute only a few percent of the neutrino flux at 1 TeV and become a dominant source of neutrinos in the atmosphere only at higher energies. The precise energy and flux of prompt neutrinos is heavily model-dependent.

Although the angular distribution of cosmic rays is isotropic, the spectrum of atmospheric neutrinos is dependent on zenith angle. Near the horizon the flux is more prominent. This is because pions, kaons, and muons produced nearly tangent to Earth have longer flight times through the atmosphere. Thus, they have more of a chance to decay into neutrinos. The effect is seen as a symmetric peak in zenith angle about the horizon in Fig 2.5.

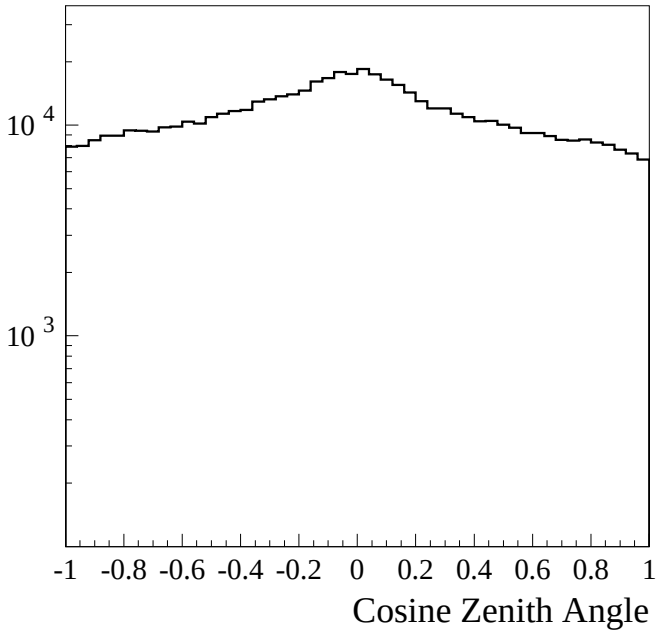

Figure 2.5: The atmospheric neutrino spectrum has a symmetric peak about the horizon.

2.3.2 The Galactic Disk

Galactic neutrinos are produced through the hadronic interactions that happen when cosmic rays diffuse though the interstellar medium. Most of the energy lost in these interactions goes into the production of mesons. These mesons subsequently decay into gamma rays and neutrinos. Since there is no atmosphere in the galactic disk, most of the mesons produced decay into neutrinos. Hence, the spectrum of gamma rays and neutrinos resembles that of the cosmic ray spectrum in the interstellar medium, $\frac{dN}{dE} = E^{-2.7}$. The flux of galactic neutrinos is small and they have a steep spectrum. Thus, they only become an issue above 1 PeV (see Fig. 2.7). Even then, the AMANDA detector's location at the south pole makes galactic neutrino detection challenging. Thus, they pose no background to this analysis.

2.3.3 Active Galactic Nuclei (AGN)

One promising source of extragalactic neutrinos is active galactic nuclei (AGN). AGN are among the most energetic objects in the universe. They emit as much energy as an entire galaxy, but are extremely compact. Their luminosities have been observed with flares extending over periods of days. The frequency of the flaring can vary from hours to years. All wavelengths of radiation from radio waves to TeV gamma rays are emitted from AGN.

AGN are believed to be powered by accreting super-massive black holes lurking in the centers of galaxies. There are two generic models for neutrino production in AGN: core models and jet models. The main difference in these

models is where the neutrinos are produced.

In core models, the neutrinos are believed to be produced in Fermi shocks of protons inside the accretion disk. The shocked protons interact with protons or photons in and around the disk producing neutrinos though pion decay as demonstrated in equation 2.14.

In AGN jet models some of the in-falling matter from the accretion disk is believed to be re-emitted and accelerated in highly energetic beamed jets that are aligned with the axis of rotation of the black hole as shown in Fig 2.6.

The particles in the relativistic jet are assumed to be accelerated by Fermi shocks in clumps or sheets of matter traveling along the jet with Lorentz factors of 10-100.

Gamma rays can be produced from electron acceleration by synchrotron radiation or Compton scattering. In the case of proton acceleration, the thermal ultraviolet photons or synchrotron photons provide the dominant target for pion production. These pions subsequently decay to gamma rays and neutrinos via equation 2.14. Different neutrino spectra are expected from electrons and photons and are the subject of debate. An observation of high energy neutrinos from these sources would help resolve the issue of particle acceleration.

2.3.4 Gamma Ray Bursts (GRB)

Gamma Ray Bursts (GRBs) are the most luminous cataclysmic phenomena in the universe. They can be characterized by their flares, which last from a few milliseconds to a few seconds and have short rise times on the order of a

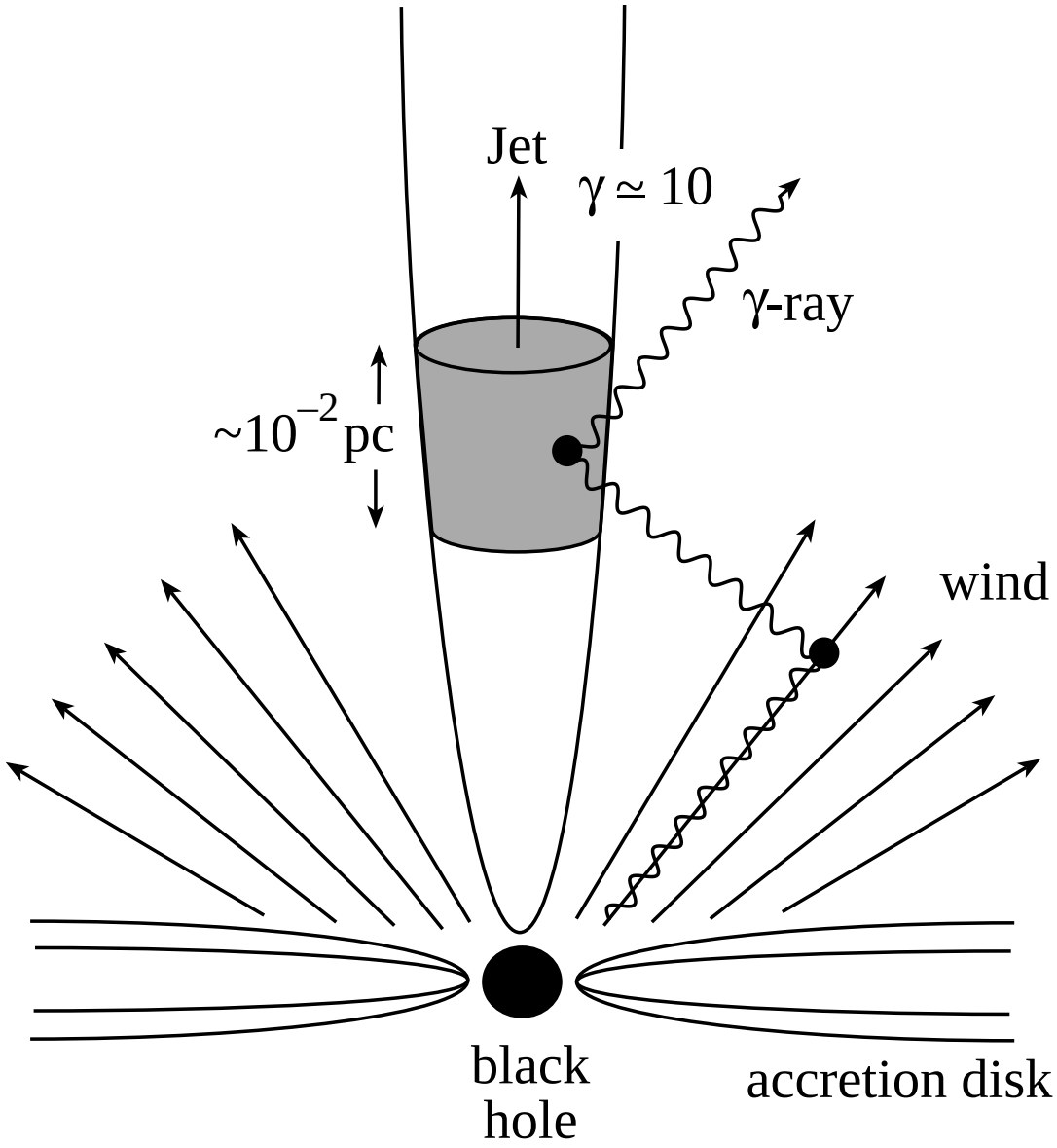

Figure 2.6: Possible production mechanism for AGN. Electrons and possibly protons, which are accelerated in sheets or blobs along the jet, interact with photons that are radiated by the accretion disk or produced in the magnetic field of the jet. Taken from [17].

millisecond followed by an exponential decay. GRBs are randomly distributed across the sky.

Although the powering process behind a GRB is still unknown, the short rise time indicates that they originate from compact objects with diameter of tens of kilometers. Possible sources of such objects are hyper-novae which result from the fusion of neutron stars or super-massive star collapse.

The bursts are believed to be produced by the dissipation of the kinetic energy of a relativistically expanding fireball. Gamma rays could be produced by the decay of neutral pions or emission of synchrotron radiation (possibly followed by inverse Compton scattering) by relativistic electrons accelerated in the dissipation shocks.

In this model, the ultra-relativistic expansion of electron-positron plasma forms a shock wave. Protons may also be accelerated by Fermi acceleration in the same region the electrons are accelerated. Neutrinos would then be created by photo-meson production of pions in interactions between the fireball γ-rays and accelerated protons.

It is interesting to note that the energy released in a GRB is about the same needed to produce the highest energy cosmic rays, whose origin are still unknown.

2.3.5 Exotic Phenomena

The highest energy cosmic rays observed have energies above 100 EeV and are difficult to explain using conventional Fermi acceleration models of charged particles. Some models [18, 19] suggest that these ultra-high energy cosmic rays

are produced by the decay of super-massive "X" particles released from topological defects, such as cosmic strings and monopoles, created in cosmological phase transitions. "X" particles can be particles such as gauge or Higgs bosons or superheavy fermions. These particles typically decay into a lepton and a quark. The quark is then theorized to hadronize into nucleons and pions. The pions can then decay into photons, electrons, and neutrinos.

2.4 Diffuse Source

The most obvious way to search for the neutrino sources described above is to identify excesses of neutrinos coming from particular sources in the sky. However, individual sources of high energy neutrinos may not be bright enough to be resolved by the AMANDA-II telescope. Fortunately, there are a large number of sources. Thus, the sources produce an isotropic background of neutrinos with high energies. A large neutrino detector, such as AMANDA-II is sensitive to diffuse fluxes of neutrinos from unresolved sources. A measurement of this background could be the first evidence of neutrinos from hidden sources.

Searching for neutrinos from diffuse sources, which is the topic of this work, is much more difficult than looking for a particular point source in the sky as there is no directional information. However, high energy neutrinos predicted to come from diffuse sources have a much shallower energy spectrum, (E^{-2}), than the atmospheric neutrino background, ($E^{-3.7}$).

Theoretical bounds can be made on the diffuse flux of neutrinos from knowl-

edge of the diffuse flux of gamma rays and cosmic rays. In the case of proton acceleration, gamma rays and neutrinos are produced in parallel. Despite the fact that neutrinos escape the source with no further interactions while the gamma rays cascade to lower energies in the source or scatter with the cosmic infrared background, the integral energy of these particles is the same within a factor of two [21]. The EGRET experiment[20] aboard the Compton Gamma Ray Observatory measured the isotropic diffuse gamma ray background intensity as

$$\Phi(E > 30\,\mathrm{MeV}) = (1.37 \pm 0.06) \times 10^{-6} E^{-2.1\pm0.03}\,\mathrm{cm}^{-2}\,\mathrm{s}^{-1}\,\mathrm{sr}^{-1}\,\mathrm{GeV}. \qquad (2.17)$$

Taking into account the factor of two mentioned above, the upper theoretical bound of the neutrino flux is on the order of $10^{-6}\,\mathrm{cm}^{-2}\,\mathrm{s}^{-1}\,\mathrm{sr}^{-1}\,\mathrm{GeV}$. This limit can be seen in figure 2.7 as the straight upper boundary of the extragalactic region.

A similar argument can be made for sources where both gamma-ray and cosmic-ray nucleons escape. For an optically thick source, both protons and neutrons are trapped in the source and the gamma ray limit applies. However, for optically thin sources, it is possible for the neutrons to escape the source without energy loss and inversely β-decay into cosmic protons outside the source. These neutrons then travel unaffected by magnetic fields in the Universe. The neutrino upper bound for these sources is represented by the curved upper boundary of the extragalactic region in figure 2.7.

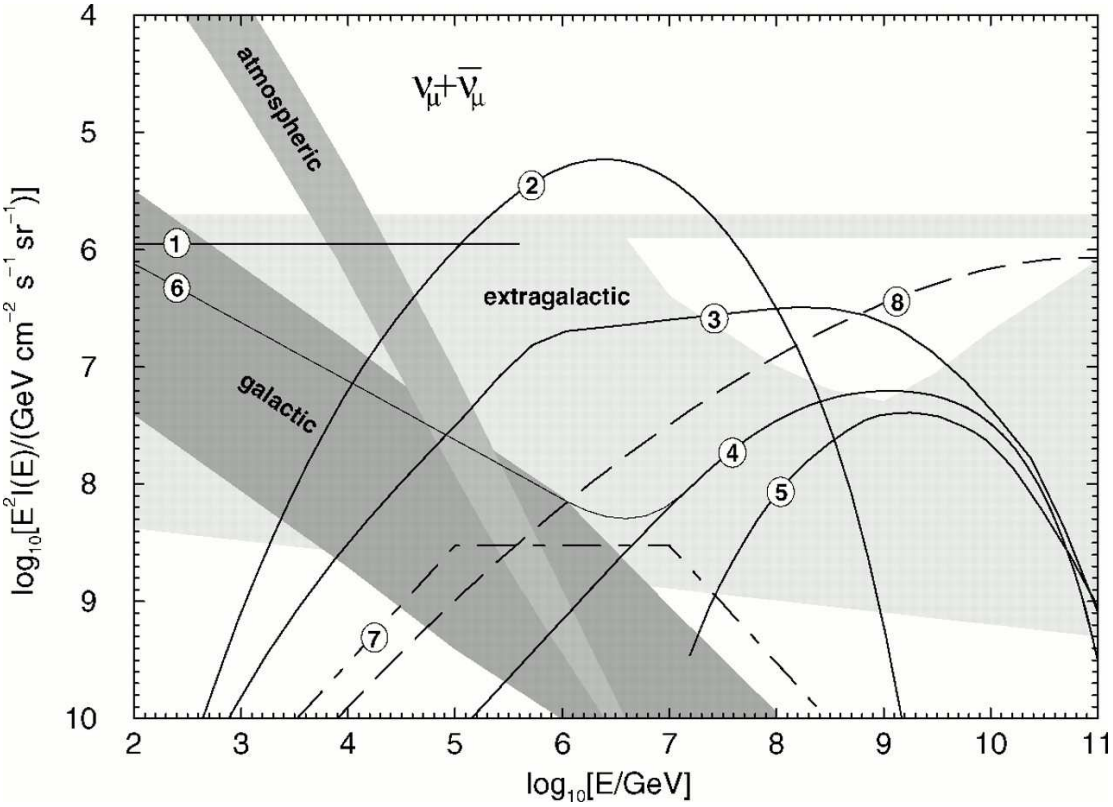

Figure 2.7: Expected fluxes of $\nu + \bar{\nu}$ intensities for emission from various diffuse sources taken from [21]. Fluxes 1-2 are predicted using the core model of emission from AGNs [22, 23], while fluxes 3-6 use the AGN jet (blazar) model [24, 25, 26, 27]. Flux 7 is a prediction of neutrinos from GRBs [28], while flux 8 is a neutrino prediction from topological defects [18, 19].

2.5 Neutrino Oscillations

Evidence from GeV scale atmospheric and MeV solar neutrino experiments, Super-Kamiokande [29] and Sudbury Neutrino Observatory (SNO) [30] strongly suggest that neutrinos oscillate from one flavor to another. The LSND accelerator experiment has also reported observing large neutrino oscillations [31]. This result is controversial and experiments are under way to confirm or refute it. In order to accommodate all three experiments a fourth neutrino, the sterile neutrino (ν_s), which does not interact has been postulated. The following discussion will consider the simplified case of two-flavor oscillations.

In order for neutrinos to oscillate from one flavor to another, neutrinos must be massive, and the eigenstates for weak interactions must be different than those for free neutrinos. The probability of a neutrino of flavor ℓ and energy E_ℓ that travels a distance L in vacuum to oscillate to a neutrino of flavor $\ell\prime$ is given by

$$P_{\nu_\ell \nu_{\ell\prime}} = sin^2 2\theta sin^2 \pi \frac{L}{L_{osc}} \tag{2.18}$$

where $sin^2 2\theta$ is the mixing angle between the two neutrinos and $L_{osc} = 4\pi E_\ell / \Delta m^2$ is the oscillation length in vacuum.

At their source, neutrinos are produced in the ratio $\nu_e : \nu_\mu : \nu_\tau \sim 1 : 2 : 0$. Due to oscillations as they travel through space, the ratio observed at Earth is $1 : 1 : 1$ [32]. Thus, muon neutrino fluxes predicted at their source would on Earth be observed as one-half the predicted flux at the source. This should be kept in mind when interpreting analysis results as many diffuse spectrum flux theories do not take this into account.

Chapter 3

Detection of Neutrinos

3.1 Neutrino-Nucleon Interactions

It is well known that neutrinos can not be directly detected. However, a neutrino or anti-neutrino traveling through matter has some small probability of interacting through charged-current scattering

$$\nu_l + N \rightarrow l^- + X \tag{3.1}$$

$$\bar{\nu}_l + N \rightarrow l^+ + X \tag{3.2}$$

where l is the lepton flavor, N is the target nucleon, and X is a combination of final state hadrons. At high energies, the lepton carries approximately half the energy of the neutrino. From the kinematics of this reaction, the neutrino and the lepton will be collinear to a mean deviation of

$$\sqrt{\langle \theta_2^{\mu\nu} \rangle} \approx \sqrt{m_p / E\nu} \tag{3.3}$$

which is about 1.75 degrees for a 1 TeV neutrino. The other half of the energy is released in the hadronic cascade, X, producing a bright, relativity localized flash

of light.

The cross section for the charged-current neutrino-nucleon interaction in the rest frame of the nucleon (assuming a relativistic outgoing lepton) is [33]

$$\frac{d^2\sigma}{dxdy} = \frac{2G_F^2 M_N E_\mu}{\pi}\left(\frac{M_W^2}{Q^2+M_W^2}\right)[xq(x,Q^2)+x\bar{q}(x,Q^2)(1-y^2)], \tag{3.4}$$

where $-Q^2$ is the invariant momentum transfer from the neutrino to the outgoing muon, q and $\bar{q}$ are the parton distribution functions of the nucleon, G_F is the Fermi constant for weak interactions and M_N and M_W are the masses of the nucleon and W boson. The Bjorken scaling variables, x and y, are given by

$$x = \frac{Q^2}{2M_N(E_{\nu_l}-E_l)} \tag{3.5}$$

and

$$y = 1 - \frac{E_l}{E_{\nu_l}}, \tag{3.6}$$

where x is the fraction of the nucleon's four-momentum carried by the interacting quark and y is the fraction of the neutrino's energy deposited in the interaction. At low energies, the neutrino cross section is four times greater than that of the anti-neutrino and the cross section is dominated by interactions with valence quarks. However, at high energies their cross sections become equal as they predominantly interact with sea quarks in the nucleon, shown in Fig 3.1.

At low energies, $-Q^2 \ll M_W$, and the term in parentheses in equation 3.4 can be neglected. In this region, the neutrino-nucleon cross section rises linearly with the neutrino energy. However, when Q^2 becomes comparable to M_W, the cross section grows more slowly, as seen in Figs. 3.3 and 3.2. This transition occurs

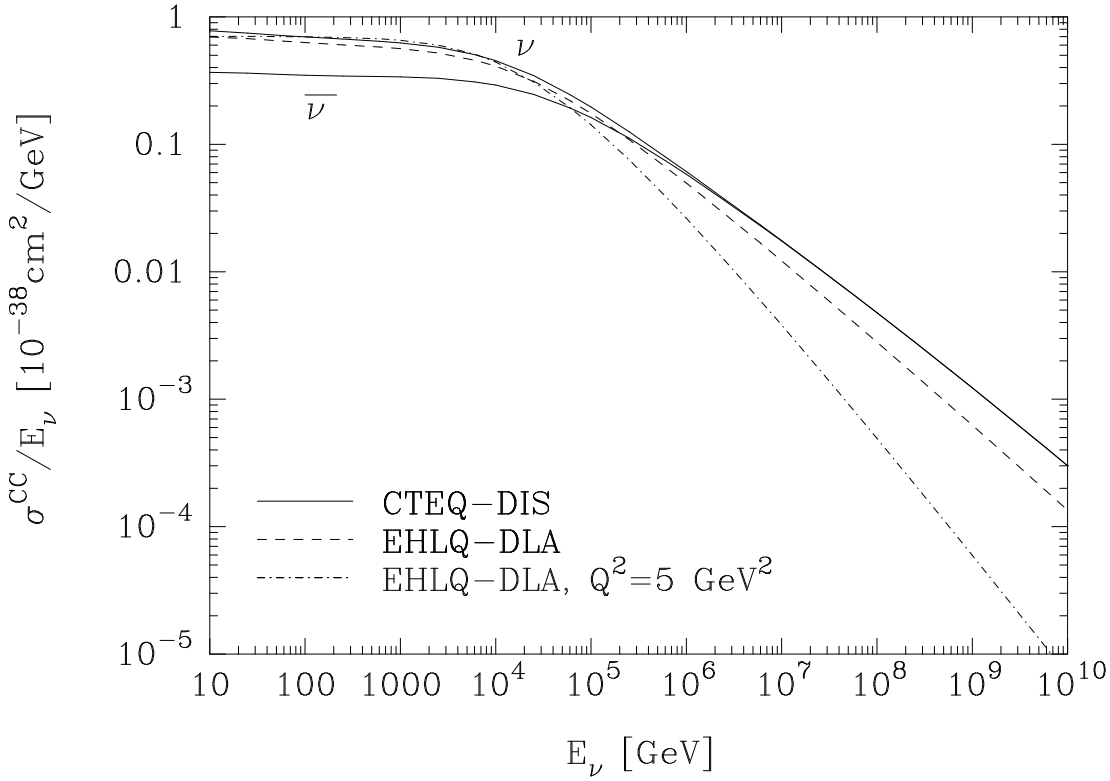

Figure 3.1: Charged-current neutrino cross sections as a function of energy [33]. The solid line is based on the CTEQ3 parton distributions. The dashed and dotted lines are from older measurements.

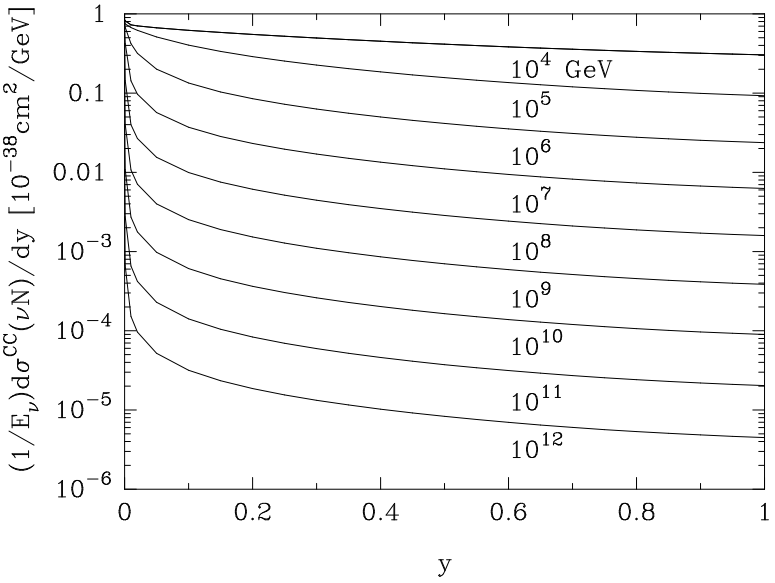

Figure 3.2: Differential cross section for neutrino-nucleon scattering for neutrino energies between 10^4 GeV and 10^{12} GeV from [33].

at approximately 3.6 TeV. In this same region the average value of y begins to fall which leads to an increase in the momentum transfer to the muon and, hence, a longer muon range. The longer muon range helps offset the slower growth in neutrino cross section.

3.2 Lepton Signatures

After a neutrino interacts with a nucleon it produces one of three different leptons. Each of these leptons leaves a distinct signature in neutrino detectors. Below the critical energy of about 600 GeV, secondary muons from muon neutrinos deposit their energy continuously at a rate of ~ 0.2 GeV per meter as they travel in a nearly straight line through the detector. The resulting experimental signature is a long linear deposition of light due to Cherenkov radiation, described in section

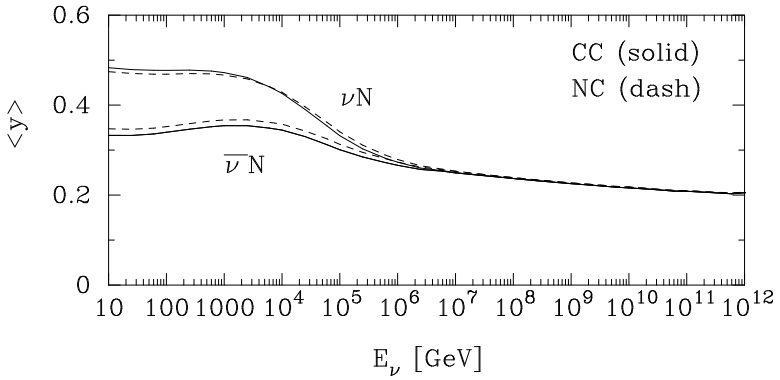

Figure 3.3: Energy dependence of the average in-elasticity of neutrino-nucleon interactions from [33].

3.3.1, that leaves a track with length of hundreds of meters, kilometers, or even tens of kilometers, depending on the initial energy of the muon. A typical muon signature in the AMANDA detector is shown in Fig. 3.4.

The signature for an event produced by interactions from an electron neutrino is a bright, spherical deposition of Cherenkov light generated by an electromagnetic cascade, and is shown in Fig. 3.5. Unlike muons, which have a long range, electrons quickly dissipate their energy by radiative processes such as bremsstrahlung and pair production. The electromagnetic cascade reaches its maximum after a few meters, a small distance compared to the spacing of the optical modules. Thus, an electron-neutrino event in the AMANDA detector looks like a point source of light.

The most striking lepton signature, not seen in AMANDA due to the detector's small size, is that of the tau neutrino. When a tau neutrino interacts with a nucleon, it produces a tau particle and a hadronic cascade at its interaction point. Subsequently, the tau particle will travel some distance and decay. This decay

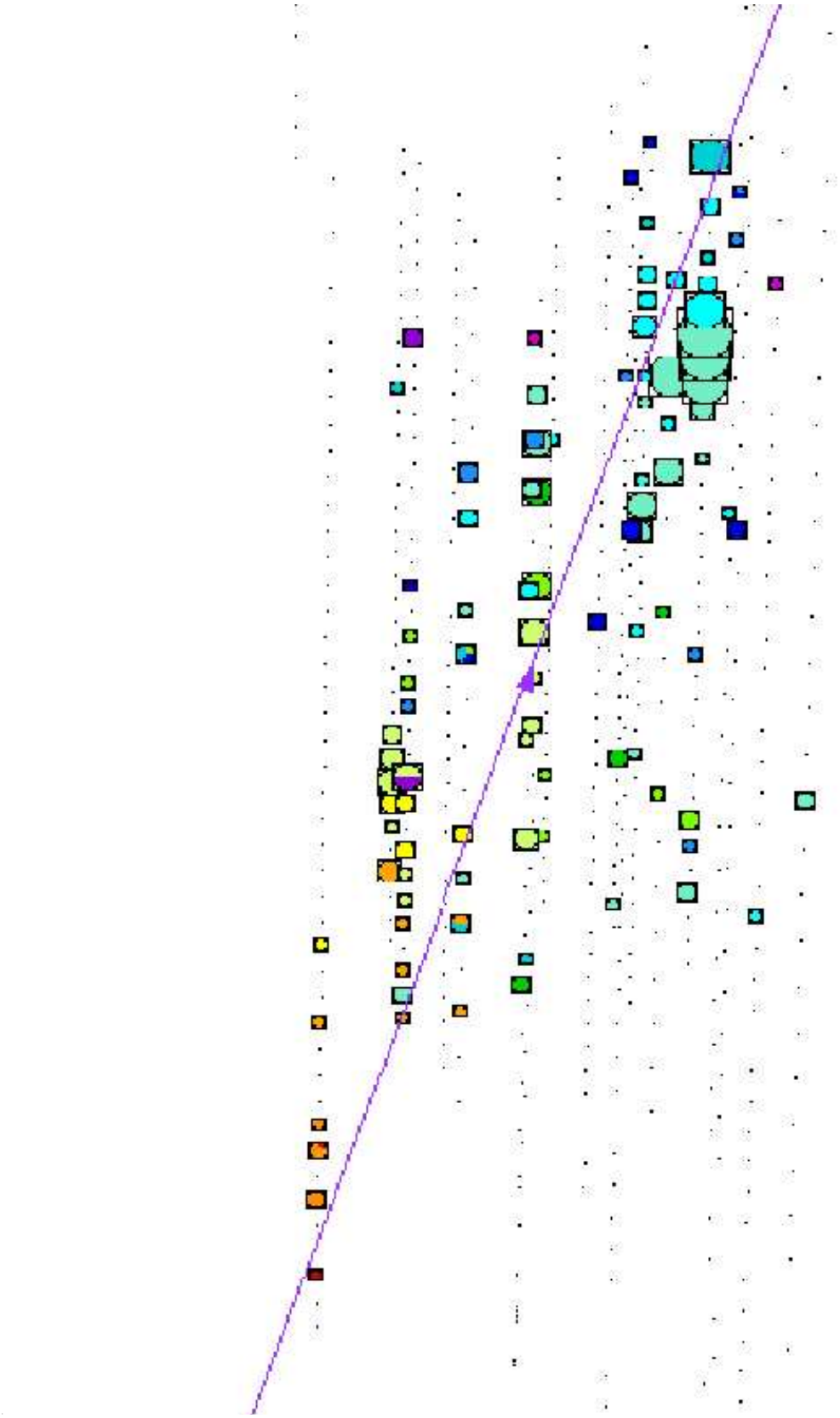

Figure 3.4: A muon event in the AMANDA detector. As the muon passes through the detector, light is emitted at a constant rate.

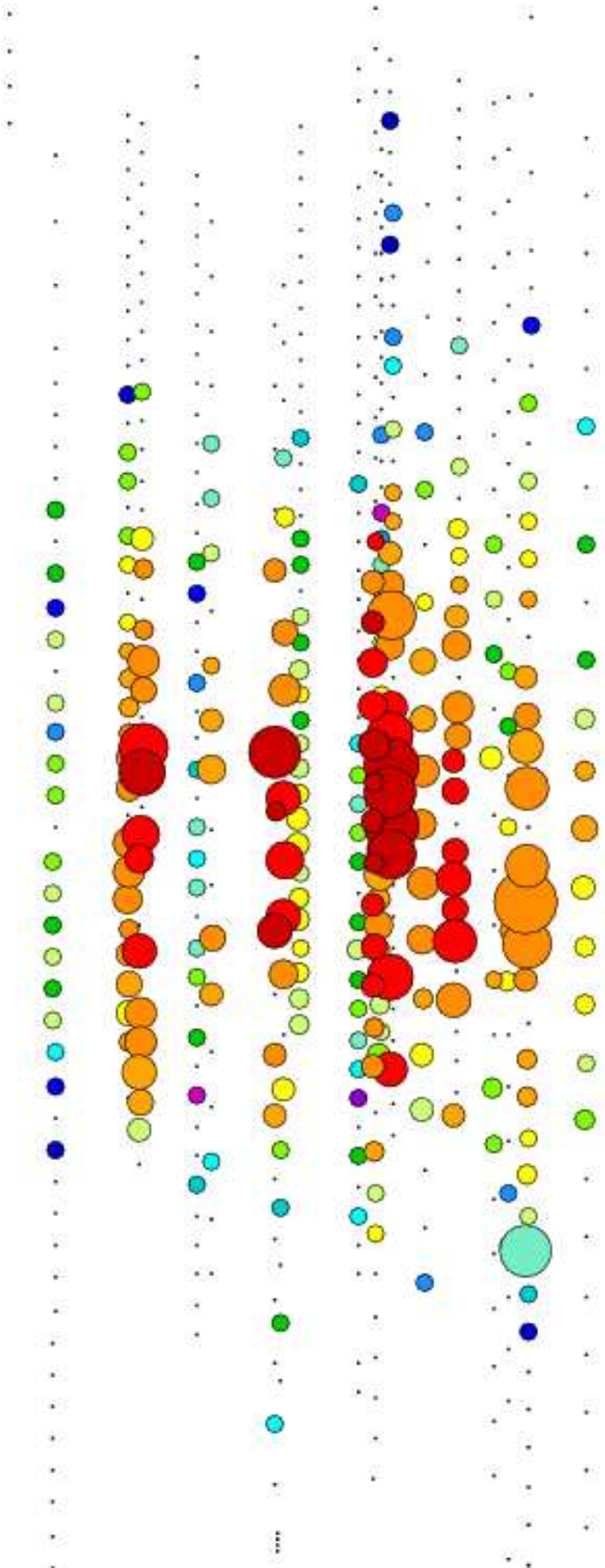

will produce a second hadronic cascade. This cascade is very difficult to resolve from the first, making it indistinguishable from a cascade produced by an electron, except at very high energies where the tau may travel hundreds of meters. For events that are contained within the detector, this "double bang" topology is a very distinctive signature, as seen in Fig. 3.6.

3.3 Muon Energy Loss

3.3.1 Cherenkov Radiation

A charged particle moving through a transparent medium with refractive index $n > 1$ with speed $v > c/n$ will produce Cherenkov radiation. Cherenkov radiation is emitted at an angle of

$$\cos\theta_C = \frac{1}{\beta n}. \tag{3.7}$$

For energies relevant to AMANDA, $\beta \sim 1$. The refractive index of ice is $n = 1.34$. Substituting these values into equation 3.7 yields

$$\Theta_c = 41^\circ. \tag{3.8}$$

The energy loss due to Cherenkov radiation is $\sim 10^3\,\mathrm{MeV/cm}$, relatively small compared to the total ionization loss of approximately $2\,\mathrm{MeV/cm}$ for minimally ionizing particles [35]. Nonetheless, a muon emits ~ 200 photons/cm, which is enough for detection [36].

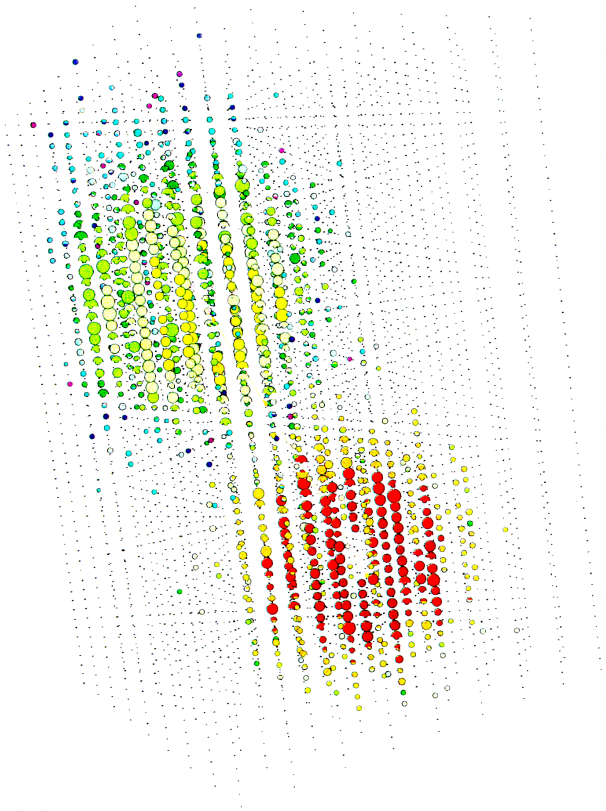

Figure 3.6: A tau event in the future IceCube detector. The two cascades of light are produced by the initial neutrino-nucleon interaction and subsequent decay of the tau particle.

3.3.2 Stochastic Energy Deposition

Muons can lose energy through several mechanisms: ionization, bremsstrahlung, pair production, and photo-nuclear processes. Ionization is a quasi-continuous process and can be treated continuously, while the others are stochastic in nature. The average rate of stochastic energy loss is nearly proportional to the muon energy. The total rate of energy loss of a muon traveling through ice per unit length can be parameterized by

$$-\frac{dE_\mu}{dx} = a(E_\mu) + b(E\mu) \cdot E_\mu \tag{3.9}$$

where a is the energy loss due to ionization and $b \cdot E$ is the energy loss due to stochastic processes [34].

In ice the value of a is approximately $0.2\,\mathrm{GeV/m}$ [34] and value of b is approximately $3.4 \times 10^{-4}\,\mathrm{m}^{-1}$. Thus, stochastic events are the main component of energy loss for muons above 600 GeV.

Chapter 4

The AMANDA Detector

AMANDA (the Antarctic Muon and Neutrino Detector Array) is an ice Cherenkov telescope located beneath the ice at the Amundsen-Scott South Pole Station. The detector is an array of 677 photomultiplier tubes and was built over the course of five years. Its primary mission is the detection of neutrinos originating from astrophysical sources.

4.1 History

The first effort to build an under-ice neutrino detector was in the austral summer of 1993/94. Four strings, each with 20 optical modules, were deployed at depths between 800 and 1000 meters. This detector became known as AMANDA-A. Studies of the ice properties at these depths showed the absorption length to be around 200 meters at the peak absorption of the photomultiplier tubes (PMTs) of 400 nm. At the same time, the scattering length was on the order of 10-20 cm, a value too small to allow the reconstruction of muon trajectories. The scattering length was dominated by tiny air bubbles trapped in the ice. It was thought

that these bubbles would be absent at 800 m as a result of the phase transition that occurs as the increasing pressure transform the air bubbles into air hydrate crystal. However, due to the low temperatures at the south pole, the diffusion of air molecules into the ice crystalline structure slows down. Thus, the bubbles only completely disappear at about 1300 m [37].

Learning from the experiences with the AMANDA-A array, the 19 strings of AMANDA-II were deployed at greater depths (1500m - 2000 m) in stages during the austral summers from 1995-2000.

4.2 The Detector

The AMANDA detector consists of a three-dimensional array of optical modules (OMs). Each OM consists of an 8" Hamamatsu PMT housed in a glass pressure sphere. The OMs are connected to the surface by an electrical cable which serves two purposes. The cable provides the high voltage necessary to operate the PMT and transmits signals from the PMTs back to the data acquisition (DAQ) system electronics at the surface.

As the AMANDA detector grew through years of deployment, the hardware used to construct the detector matured. The first 4 strings of what is now known as the AMANDA detector (then called AMANDA-B4) were deployed in the austral summer of 1995-96. These 86 OMs where connected to the surface by coaxial cable, which provided protection against electronic crosstalk in the cables. Unfortunately, coaxial cable has limitations. Coaxial cable is quite dispersive, resulting

in distortion during the course of transmission to the surface (10 ns PMT pulses arrive at the surface with a width of more than 400 ns). Coaxial cable is also quite thick, limiting the number of cables that could be bundled together.

For these reasons the next 6 strings, which were deployed during the austral summer of 1996-97, used twisted pair cables. These 6 strings brought the total number of OMs in the array to 302. This new array was named AMANDA-B10. The twisted pair cables had less dispersion (150 ns - 200 ns) and allowed more cables per string. However, a great deal of electronic crosstalk was observed in these strings.

During the austral summer of 1997-98 another 3 strings were deployed bringing the total number of OMs to 428. These strings had both optical fibers and traditional twisted pair cables. The optical fibers were essentially dispersion free and crosstalk free. However, they were quite fragile and nearly 10% were damaged during the refreeze process. Another change in the deployment of these three strings was that they were to lie at a depth between 1200 m - 2400 m in order to study the optical properties above and below the detector.

The last strings to be added to the array were strings 14-19 in the austral 1999-2000 summer. This marked the completion of the AMANDA-II detector. All OMs on these strings were connected to the surface via optical fibers and traditional twisted pair cables. Some of the modules deployed during this year contained experimental digital technologies under investigation for future ice-Cherenkov detectors. String 18 is comprised entirely of digital optical modules

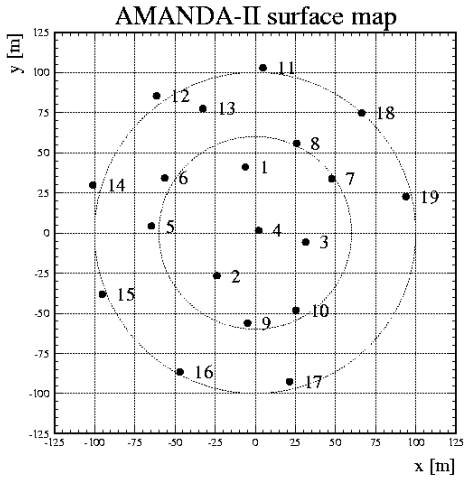

Figure 4.1: Top view of the AMANDA-II detector. The radius of the detector is approximately 100 meters.

(DOMs). These modules contained analog transient waveform digitizers (ATWDs) which record and digitize the signal *in situ* and then transmit them to the surface. This technology results in the full retention of waveform information without the need for optical fibers. However, the DAQ electronics are buried with the OMs in the ice, hence, beyond the possibility of repair or upgrade.

The complete AMANDA-II detector contains 19 strings, 677 OMs and instruments 0.015 km^3 of ice. It has a diameter of 200 m and a height of 500 m. The modules on each string are separated by 10 m - 20 m, depending on the string. The strings are arranged in three concentric circles and separated by 30 m - 60 m. Figures 4.1 and 4.2 show the layout of the AMANDA detector.

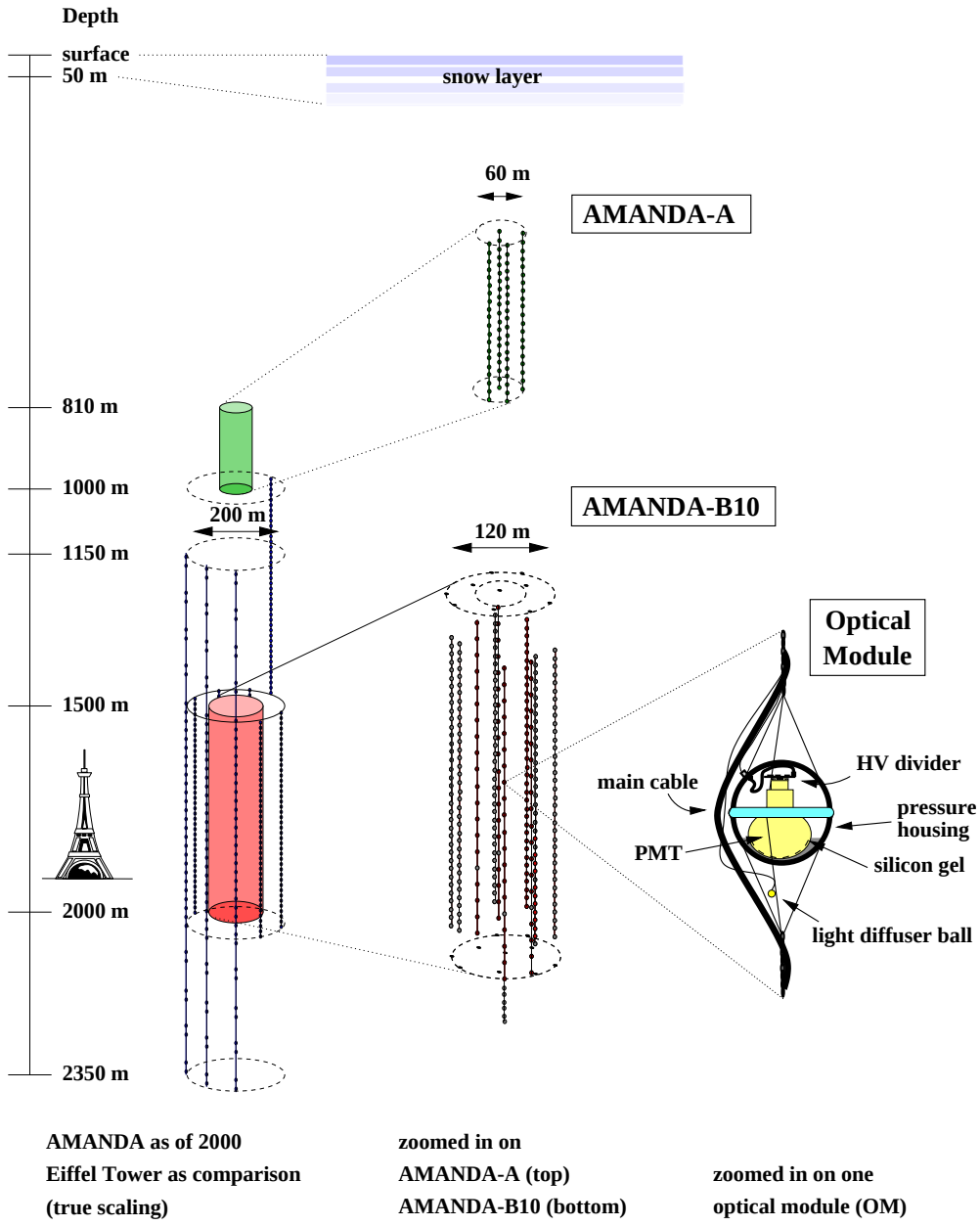

Figure 4.2: Schematic of the geometry of AMANDA-II. AMANDA-A and AMANDA-B10 are shown in expanded view in the center. An optical module is blown up on the right. The Eiffel Tower is shown to illustrate the scale.

The first strings of the IceCube detector are scheduled to be deployed in the austral summer of 2004-05. The entire IceCube array will contain some 4800 OMs, 80 strings and instrument 1 km^3 of ice. It is scheduled to be completed in 2009-10. All of the OMs in the IceCube array will use the DOM technology. IceCube will be deployed between the depths of 1400 m and 2400 m.

4.3 Data Acquisition

The AMANDA detector trigger can come from a variety of sources. In normal mode, the detector is triggered by the detection of photons by a set number of OMs in a preset window of time (majority trigger). For the AMANDA-II year 2000 data set, 24 OMs were required to receive at least 1 photo-electron in a 2.1 μsec time period. The trigger rate was approximately 100 Hz.

The data acquisition (DAQ) system, located on the surface, is responsible for reading out event information and storing it to disk. Information read and stored by the DAQ includes the leading edge time (LE) and the width or time-over-threshold (TOT) in the time window $\sim 22\,\mu sec$ before and $\sim 10\,\mu$sec after the trigger time. The DAQ also records the amplitude of pulses arriving from the OMs. The analog digital converter (ADC) information is recorded during a time window of $\pm 2\,\mu$sec around the trigger time. The event time is obtained from a Global Positioning System (GPS) unit.

A majority trigger in AMANDA is formed based on hit multiplicity. When an OM detects a photo-electron it sends a pulse to the surface where it is received

by a Swedish Amplifier (SWAMP) which amplifies the signal. A copy of the signal is then sent to discriminators where the signal is converted to a 2 μsec square pulse. The discriminator sends its output to the Digital Multiplicity Adders (DMAD) where multiple signals are summed and compared to a preset threshold. In 2000, this threshold was set at 24 channels. When the sum crosses the threshold, a stop signal is sent to all time digital converters (TDCs) and a veto of several μsec is sent to the trigger. All channels are then read out and the system reset.

4.4 Ice Properties

Understanding the properties of the ice is crucial for the operation of the AMANDA-II detector. Thus, the scattering and absorption properties, which affect the timing and number of photons that reach the OMs, must be throughly understood. Numerous studies using both *in-situ* light sources and atmospheric muons have been conducted to determine the ice properties.

The ice is characterized using three parameters: the scattering length λ_b (or the scattering coefficient $b = 1/\lambda_b$), the absorption length λ_a (or the absorption coefficient $a = 1/\lambda_a$), and the average of the cosine of the scattering angle ($\tau_s = \langle cos\theta \rangle$. The effective scattering length is then defined as $\lambda_b^{eff} = \lambda_s/(1-\tau_s)$ and its coefficient is $b_e = 1/\lambda_b^{eff}$. The effective scattering and absorption coefficients are shown in Figs. 4.3 and 4.4 as a function of wavelength.

Dust grains (about 0.04 microns in size) are the biggest contributors to scattering and absorption in the antarctic ice below 1400 meters. Air bubbles,

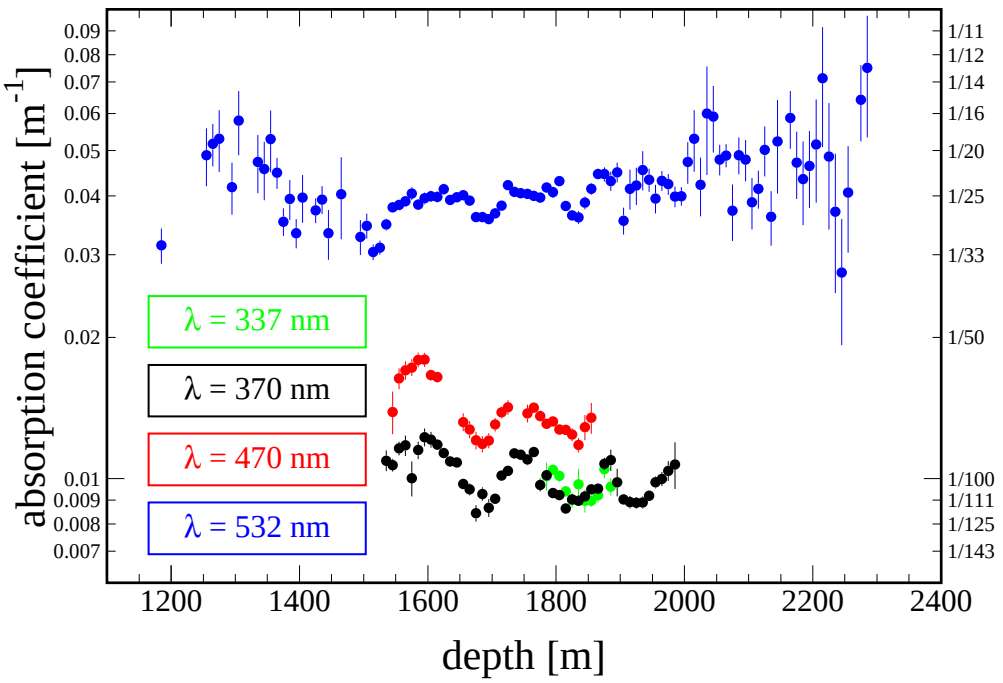

Figure 4.3: Absorption coefficients as a function of depth at various wavelengths [38].

which were the largest scatterers in the AMANDA-A detector, are squeezed into air hydrate crystals which have nearly the same index of refraction as ice at AMANDA-II depths and pose no problems to light detection.

Although the glacial ice in which AMANDA-II is embedded is nearly uniform, climatological events in Earth's past, such as ice ages, have left layers of impurities in the form of dust, soot, etc. These dust layers affect the optical properties of the ice and affect photon propagation.

The first measurements of the scattering and absorption coefficients of these layers was done using a YAG laser at a frequency of 532 nm. Figure 4.5 shows the effective scattering coefficient as a function of depth in the detector. The dust

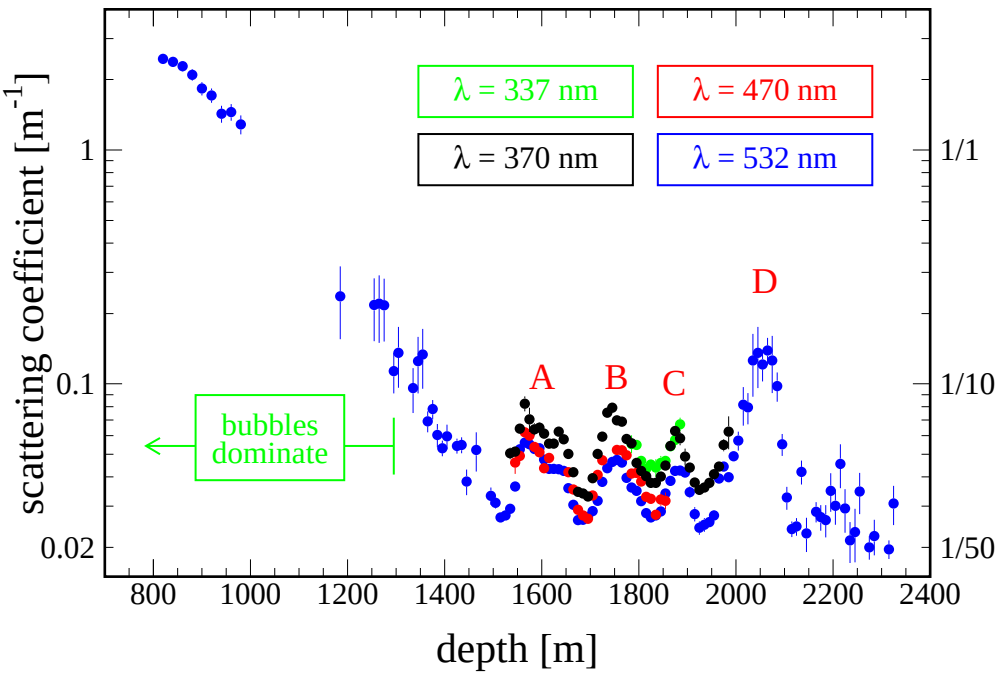

Figure 4.4: Scattering coefficients as a function of depth at various wavelengths [38].

layers are visible as peaks in the scattering coefficient while the clear layers are visible as valleys.

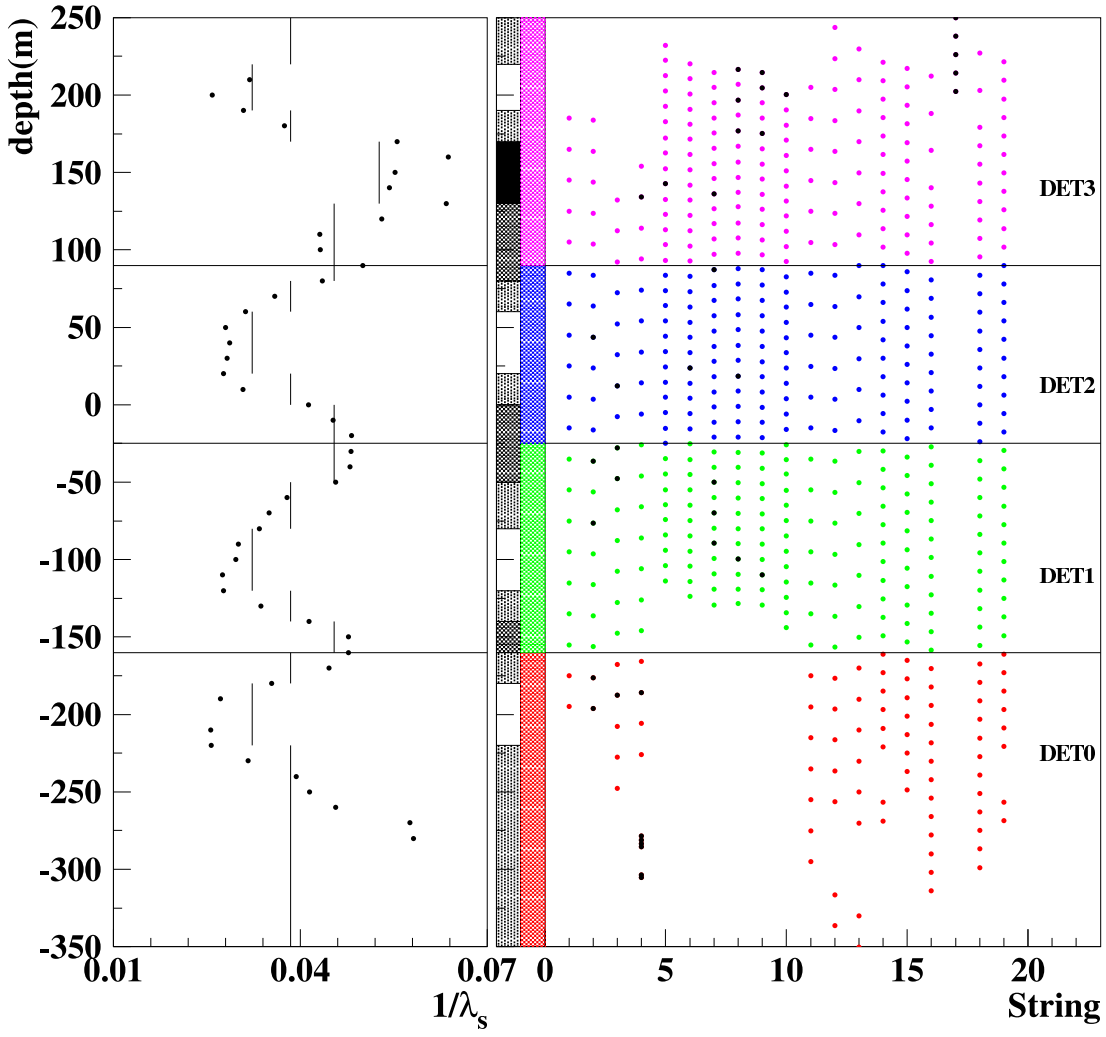

Figure 4.5: Scattering coefficient as a function of depth, indicating the presence of dust layers. On the left side of the plot the depth of the OMs in relation to the dust layers are shown [39].

Chapter 5

Event Reconstruction and Analysis Tools

Reconstruction algorithms in AMANDA, like the hardware used to build it, have developed over time. Reconstructions for both muon tracks and cascades are based on the principle of maximization of a likelihood function. Due to how sparsely the AMANDA detector is instrumented, only a limited set of parameters can be constrained for each event. For muons, these parameters are direction (θ, ϕ), position(x, y, z), and time (t).

5.1 Direct Walk Reconstruction

The direct walk [40, 41, 42] method of reconstruction is a *first guess method* of reconstruction based on pattern recognition of selected hits from photons that have not scattered much in the ice. First guess methods of reconstruction are very fast analytic algorithms that are used as initial track guesses for more complicated algorithms which will be described in the following sections.

The direct walk algorithm looks for track elements which are pairs of hits consistent with a close track such that

$$\left| \frac{|\vec{r_1} - \vec{r_2}|}{c} - |t_1 - t_2| \right| < 30\,\mathrm{ns} \tag{5.1}$$

where $\vec{r_i}$ is the position of the *ith* hit and t_i is the time of the *ith* hit. Associated hits, those with small time residuals and appropriate distance from the track element based on time residuals, are selected. Quality criteria such as the number of associated hits, the spread of associated hits, and the hit density along the track element are applied. Track elements that pass these criteria are called *track candidates*. The final first guess track is then found by searching for clusters in zenith angle of track candidates and calculating the mean of all track candidates belonging to the cluster.

5.2 Maximum Likelihood Reconstruction

The maximum likelihood method [42] is a generalization of the χ^2 method. In the limit of Gaussian uncertainties the likelihood, $\mathcal{L}$, is related to χ^2 by $-2\ln\mathcal{L} = \chi^2$. These methods attempt to find the track hypothesis that maximizes the likelihood by minimizing $-log\mathcal{L}$ with respect to the track parameters. In general, the likelihood for a given event E_0, which is a collection of detector responses $\mathcal{R}_i$ and a hypothesis H_j, is written as

$$\mathcal{L}\left(E_0|H_j\right) = \prod_i \mathcal{L}_i\left(\mathcal{R}_i|H_j\right). \tag{5.2}$$

If the hypothesis is true, it then generates the observed pattern of hits. The hypothesis is then allowed to vary and an optimization routine is used to find

the location H_0 of the global extremum of $\mathcal{L}$. The responses $\{R_i\}$ recorded by AMANDA are the time, t_i, and duration, TOT_i, of each PMT signal and the peak amplitude, A_i, of the largest pulse in each PMT.

In the case of muon reconstruction, one assumes that the Cherenkov radiation is generated by a single infinitely long muon track. This is a reasonable assumption for the energies of this analysis which simplifies and speeds up the calculation and optimization. For muons, this reduces the function H to six-dimensions $H = H(\vec{x}, \theta, \phi, t)$.

5.2.1 Time Likelihood

By applying the assumption of an infinitely long muon track we arrive at the simplified likelihood function. The function depends on the arrival time of the light,

$$\mathcal{L} = \prod_{i=1}^{nhits} p\left(t^i_{res} | d_i, \eta_i ...\right), \tag{5.3}$$

where t^i_{res} is the time delay, d_i is the distance of the OM from the track, and η_i is the orientation of the OM relative to the track. The probability density function of single photons, $p(t^i_{res}|d_i, \eta)$, was generated by parameterizing Monte Carlo simulations of photon propagation in ice [43].

The negative logarithm of the likelihood function, $-log\mathcal{L}$, is then minimized using a Simplex [44] algorithm in an iterative technique, which performs multiple reconstructions of the same event. Each reconstruction starts with a different initial track hypothesis. The results of all iterations are compared to each other.

The lowest value of $-log\mathcal{L}$ is taken as the reconstructed track.

5.2.2 Bayesian Likelihood

Bayes' theorem allows us to fold in information independent of the measurement into the likelihood function. The theorem states

$$P(A|B)\,P(B) = P(B|A)\,P(A)\,. \tag{5.4}$$

Identifying A with the hypothesis H and B with the hit pattern E and solving for $P(H|E)$ gives

$$P(H|E) = \frac{P(E|H)\,P(H)}{P(E)}. \tag{5.5}$$

The quantity $P(E|H)$ is the likelihood that the given set of hits would be generated by the hypothesis of interest. $P(E)$ is the probability that a given pattern of hits is observed. This quantity is independent of track parameters and is therefore constant. $P(H)$ is known as the *prior* and does not depend in any way on the measurement. It is the probability of observing the track and can be calculated prior to the measurement. Thus, $P(H|E)$ is the probability of the hypothesis after E is taken into account.

Bayesian event reconstruction [45] uses the prior probability function shown in Fig. 5.1. This function is flat over the up-going hemisphere and dependent on zenith angle in the down-going hemisphere. Reconstructing using this technique requires one to maximize the product of the probability density function and the prior. Similar to the time likelihood reconstruction, this is done using the Simplex minimizer and an interactive minimizing technique.

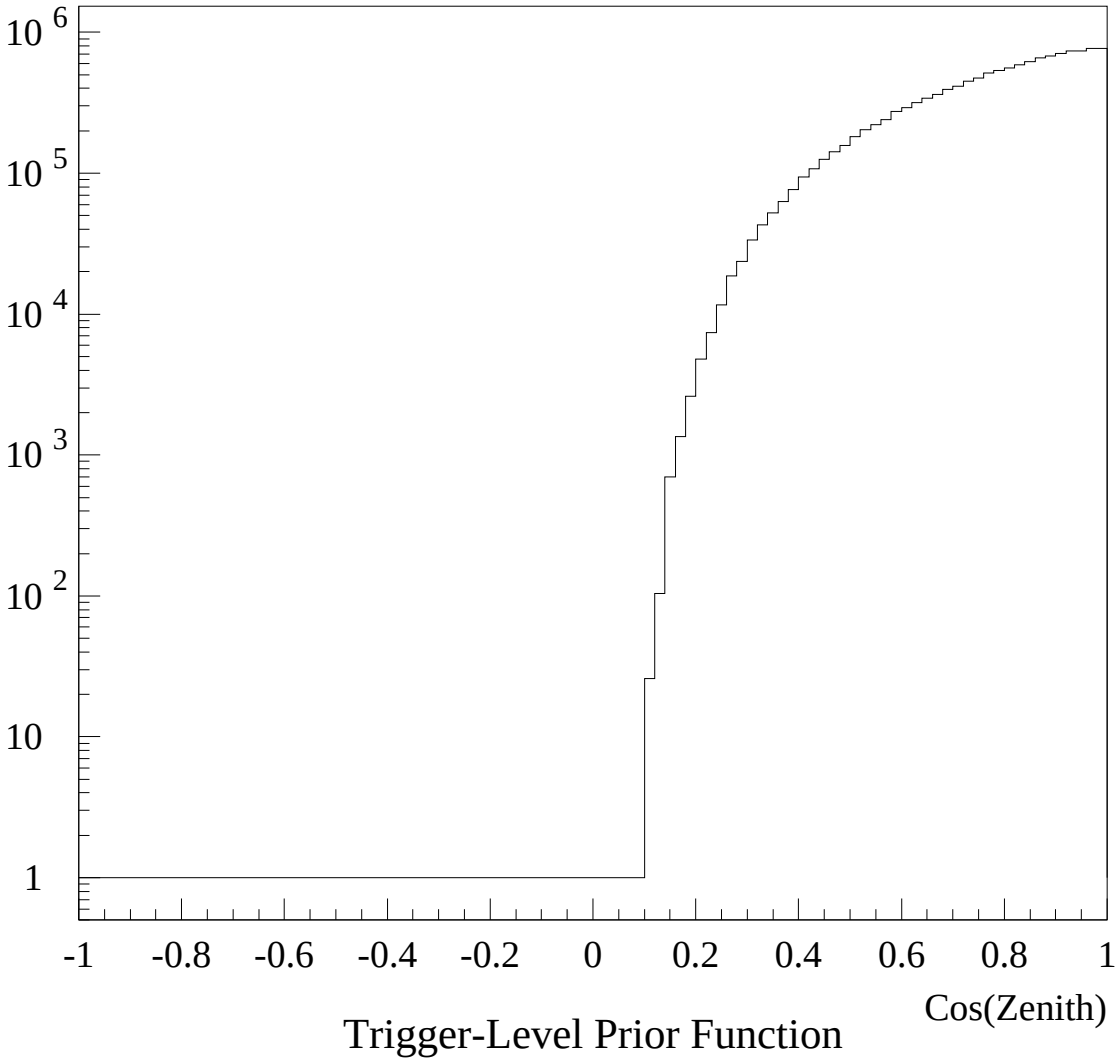

Figure 5.1: The prior function used is flat over the up-going hemisphere and dependent on zenith angle in the down-going hemisphere [36].

Near the horizon the effect of the Bayesian reconstruction is strongest. Since AMANDA-II is narrow, events coming in near the horizon have shorter track lengths, making it difficult to constrain the fit tightly. The prior indicates that tracks from atmospheric muons are more likely than neutrinos. Thus, the reconstruction properly chooses the down-going fit as being more likely.

5.3 Quality Parameters

Quality parameters are used for selection criteria during different stages of the analysis. Below are descriptions of the parameters that will be used for this analysis.

5.3.1 Likelihood Ratio

As discussed in the previous section, a Bayesian maximum likelihood fit is performed on the sample to fit muon tracks to the observed events. The functional form used is the negative logarithm of the likelihood. This analysis uses two likelihood ratios, up-to-down and track-to-cascade. The likelihood ratio for up-to-down going events is defined as

$$R_L^{u/d} = log(\frac{\mathcal{L}_{up}}{\mathcal{L}_{down}}) \tag{5.6}$$

and the likelihood ratio for track-like to shower-like events is defined as

$$R_L^{t/s} = log(\frac{\mathcal{L}_{track}}{\mathcal{L}_{shower}}). \tag{5.7}$$

$\mathcal{L}_{up}$ is the likelihood of the track being up-going and hence from a neutrino and $\mathcal{L}_{down}$ is the likelihood of the track being down-going and hence from a cosmic

ray. $\mathcal{L}_{track}$ is the likelihood of the event being from a muon and $\mathcal{L}_{shower}$ is the likelihood of the event being from a cascade.

The up/down likelihood ratio is the most powerful parameter for separating cosmic ray background events (down-going) from signal neutrinos (up-going).

5.3.2 Smoothness

"Smoothness" (S_{phit}) is a topological parameter that is defined by the distribution of hits along the track. It measures how consistent the observed pattern of hits is with the hypothesis of constant light emission by a muon.

5.3.3 Number of Direct Hits

A "direct hit" occurs when a photon is delayed little by scattering in the ice between production and detection. This delay is measured relative to the predicted arrival time of an unscattered Cherenkov photon emitted from the appropriate point along the track. Different delay windows exist for counting direct hits. For this analysis a hit is considered direct when it arrives in a window of [-15:75] nanoseconds. Thus, $N_{dir}^{[-15:75]}$, is defined as the number of direct hits in an event.

5.3.4 Track Length

The track length is determined by projecting each of the direct hits onto the reconstructed track and measuring the distance between the first and last hits. In this analysis, two different track lengths were defined. The first uses a stricter direct hit definition than described above. For this track length, the direct hits

are required to arrive in the time window [-15:25] nanoseconds

$$L_{dir}^{[15:25]} \tag{5.8}$$

and the second uses the definition of direct hits from above

$$L_{dir}^{[15:75]} \tag{5.9}$$

where direct hits were required to arrive in the [-15:75] nanosecond window.

5.3.5 Zenith Angle

In this analysis, the zenith angle of the best up-going fit and the zenith angle of the best down-going fit are also used in conjunction with the number of direct hits of the best up-going fit and the number of hits of the best down-going fit to remove coincident muon events from cosmic rays.

5.3.6 Center of Gravity

The center of gravity ($\overrightarrow{cog}$) of an event is defined as the mean position of all OMs hit by one or more photons in an event. It is represented mathematically as

$$\overrightarrow{cog} = \frac{1}{nch} \sum_{i=0}^{nch} \vec{r_i} \tag{5.10}$$

where nch is the number of OMs to receive at least one photon and $\vec{r_i}$ is the distance from the center of the detector to the center of the event.

5.4 The Model Rejection Potential

An upper limit on an expected flux can be derived from observation when an experiment fails to detect an expected flux. The method used in this thesis is

the *model rejection potential* [47]. It uses the method developed by Feldman and Cousins [46] to find the limit. In the Feldman and Cousins method, the upper limit, μ, is a function of the number of observed events, n_o, and the number of predicted background events, n_b,

$$\mu \equiv \mu\left(n_o, n_b\right). \tag{5.11}$$

The flux limit is then calculated by the formula

$$\Phi_{CL} = \Phi \times \left(\frac{\mu_{CL}}{n_s}\right) \tag{5.12}$$

where CL is the desired confidence level of the calculation, Φ is the expected flux, and n_s is the number of signal events predicted from that flux.

Since the actual upper limit cannot be known until looking at the data, simulations can be used to calculate the expected *average upper limit*. The average upper limit is the sum of the expected upper limits, weighted by their Poisson probability of occurrence. It can be written mathematically as

$$\bar{\mu}_{CL} = \sum_{n_{obs}=0}^{\inf} \mu_{CL}\left(n_{obs,n_b}\right) \frac{\left(n_b\right)^{n_{obs}}}{\left(n_{obs}\right)!} e^{-n_b}. \tag{5.13}$$

Using the average upper limit, one can find the optimal selection criteria for setting the best limit without using the data. When the optimal selection criteria are applied to the Monte Carlo simulations, they will yield the sensitivity of the experiment. Over an ensemble of identical experiments, the strongest constraint on the expected signal flux will correspond to the set of cuts that minimizes the *model rejection factor*. The model rejection factor is defined by

$$mrf \equiv \frac{\bar{\mu}_{CL}}{n_s} \tag{5.14}$$

where n_s is the predicted number of signal events from the expected flux.

The model rejection factor can then be used to find the expected upper limit (the sensitivity) defined by

$$\bar{\Phi}_{CL} = \Phi \times \left(\frac{\bar{\mu}_{CL}}{n_s} \right). \tag{5.15}$$

The actual experiment is not likely to yield exactly $\bar{\Phi}_{CL}$. This is because the limit in that case will be based on the observed number of events, which is subject to fluctuations in the background in that particular experiment. The sensitivity, which is the average flux upper limit, would give the average value expected over repeated runs of a real experiment.

Chapter 6

Data and Monte Carlo Simulations

6.1 Live-Time

The total data acquisition time for the year 2000 was 254.2 days. Taking into account the dead time of the data acquisition system, this corresponds to 211.5 days of detector live time. During that time there were a total of 1,444,252,130 triggers registered. Of those triggers, 90.7% were formed with the majority trigger, which required at least 24 OMs to have fired during the event.

File cleaning was performed to remove problematic files. A problematic file is one that has at least one of the following symptoms

$$N_{hot} > 5 \tag{6.1}$$

$$N_{dead} > 50 \tag{6.2}$$

$$N_{unstable} > 10 \tag{6.3}$$

where N_{hot} is the number of OMs with ADC and/or TDC rates greater than 30 Hz, N_{dead} is the number of OMs with ADC and/or TDC rates less than 0.5 Hz,

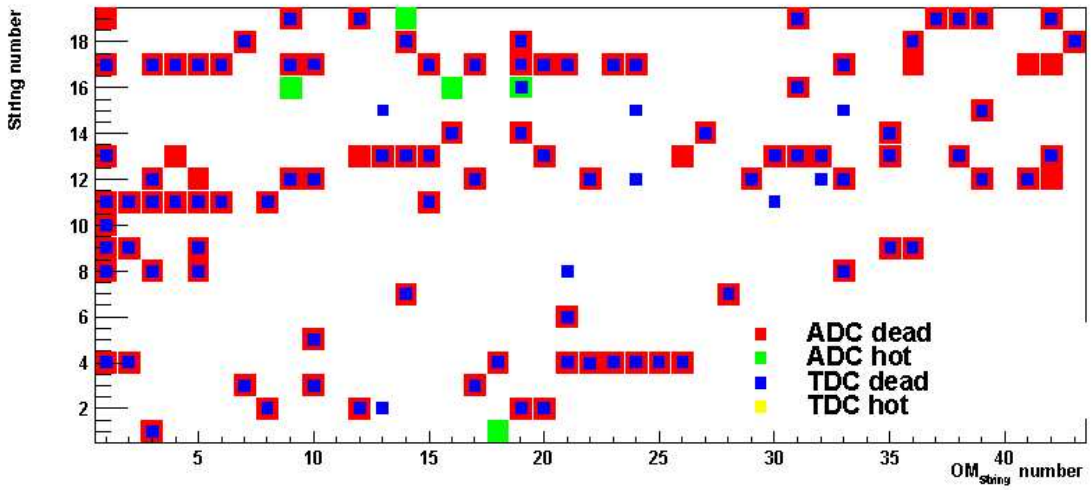

Figure 6.1: The optical modules excluded from the 2000 analysis and their status.

and $N_{unstable}$ are the number of OMs with unstable ADC and/or TDC rates. The file cleaning removed about four percent of the events and reduced the detector live time to 197 days for the year.

6.2 OM Selection

An OM is considered bad if the ADC and/or TDC rate is too high, too low or zero, or if the number of edges from the TDC is too high. Figure 6.1 shows the OMs excluded in 2000.

In addition to the OMs above, other OMs were excluded on a time-dependent basis in an attempt to increase the effective area of the detector. These OMs demonstrated transient behavior, meaning at certain times of the year the OM operated normally and at others the ADC/TDC rates demonstrated the behavior described above. In order to do this most efficiently, the year was divided into

three periods, with period 1 covering days 44 - 125, period 2 covering days 126 - 244, and period 3 covering days 245 - 315.

6.3 Hit Cleaning

The data recorded by the AMANDA detector are not perfect. Each event has apparent hits due to various types of noise. The OMs themselves produce some of this noise; there is dark noise from the PMTs and noise produced by the decay of the radioactive potassium isotope ^{40}K in the glass sphere which encases the PMT. The PMTs are also subject to pre-pulsing and after-pulsing. There is randomized cross-talk between OMs which can occur in the strings themselves or the surface electronics. In addition to all this, there is electronic noise in the DAQ.

Several criteria are used to reduce the number of hits due to noise. The calibrated amplitude is required to give a reasonable number of photoelectrons, $0.1\,\mathrm{pe} < \mathrm{ADC_{calib}} < 1000\,\mathrm{pe}$. To eliminate random noise at the beginning and after-pulsing at the end, the event duration window is reduced to $-2000\,\mathrm{ns} < \mathrm{LE} < 4500\,\mathrm{ns}$. Requirements of minimal amplitudes, $\mathrm{ADC} > 20\,\mathrm{mV}$, and time over thresholds, $124\,\mathrm{ns} < \mathrm{TOT_{elec}} < 2000\,\mathrm{ns}$ for electrical and $5\,\mathrm{ns} < \mathrm{TOT_{elec}} < 2000\,\mathrm{ns}$ for optically read out channels, reduces the electronic noise and electrical cross-talk. Finally, an isolation cut requiring a hit to be within 100 m and 500 ns of another hit eliminates hits due to random noise.

6.4 Filtering

The AMANDA data used in this thesis were recorded between February 13, 2000 and November 6, 2000. Over 1 billion events in 37,838 files took up 1.41 TB of disk space prior to filtering. Each file consists of approximately 10 minutes of data which were recorded by the DAQ electronics. The files were grouped into runs. Each run usually corresponds to one day of data taking. All files were then written to magnetic tape and transported north for final processing and storage.

The data used in this thesis were processed at the DESY Laboratory in Zeuthen Germany. Doing a complete 16-iteration maximum likelihood reconstruction as described in section 5.2 is not practical with AMANDA's current resources. A 16-iteration maximum likelihood reconstruction takes approximately 1 second per event. Processing all 1.4 billion events would take approximately 4 months with the current AMANDA resources. As a consequence the AMANDA data is put through a series of filtering levels described below.

6.4.1 Level 1

In lieu of the full maximum likelihood reconstruction, a quick direct walk reconstruction as described in section 5.1 is performed on all events. This is the first fit placed on the data. Only events which pass the following cut

$$\theta_{DW} > 70 \tag{6.4}$$

are allowed to remain in the data set.

A full 16-iteration maximum likelihood reconstruction is then performed on

the remaining events. Another cut is placed on the data set,

$$\theta_{fullfit} > 70. \tag{6.5}$$

The passing rate, after all selection criteria of level 1 are implemented, is 1%.

6.4.2 Level 2

The data set is reduced further at the second level of data filtering. The first step of the level 2 filter is to place the following cut to the data

$$\theta_{fullfit} > 80 \tag{6.6}$$

where $fullfit$ refers to the maximum likelihood reconstruction of level 1. Then six more reconstructions, including a multi-photon, a Bayesian, and several cascade reconstructions, are applied to the remaining data set. The passing rate of the level 2 filter is 0.4%

6.5 Background Reduction

After the general filtering and cleaning procedures were applied, there were still non-neutrino backgrounds remaining in the sample. Further cleanings were performed to remove these backgrounds. These backgrounds can be attributed to electronic cross talk, coincident muon events from cosmic rays, and mis-reconstructed cosmic rays. Details of the procedures are described below.

6.5.1 Level 3 - Electronic Cross-Talk and Muons from Cosmic Rays

At level three two cleanings were performed. The first cleaning was used to remove electronic cross talk that results from capacitive coupling between ca-

bles. Secondly, a cut was developed to further remove muons in the data sample resulting from mis-reconstructed cosmic rays at the horizon.

Electronic cross-talk is known to occur between OMs located on the same strings in the twisted quad cables used in strings 5 - 10 of the AMANDA detector. This cross-talk cannot always be removed using basic cleaning algorithms. For this reason, a special hit cleaning was developed.

The first improvement to be made was to increase the TOT cut for hybrid OMs. Sixteen OMs have hybrid bases that were used for experimenting with optical transmission of signal to the surface. For normal data taking purposes, these channels are read out using the electrical output rather than the optical output. The electrical signal output for these OMs is much wider than that of normal OMs. Therefore, the minimum TOT requirement was increased from 120 ns to 200 ns for hybrid OMs. Thus, for standard and hybrid OMs, the minimum TOT required corresponds to ~ 0.3 pe.

Cross-talk maps of the detector were made for the 2000 data using timing calibration data. Using these maps, the unphysical regions of the ADC versus TOT plots were cut out with the program xt-filt. Figure 6.2 demonstrates visually how this was done. The boundary between the physical and unphysical region in the ADC versus TOT space has been fit by an exponential function. A shift of 20 mV in ADC and 20 ns in TOT is added to the ADC versus TOT distribution boundary to account for any fluctuations. More details about cross-talk in AMANDA can be found in [48, 49].

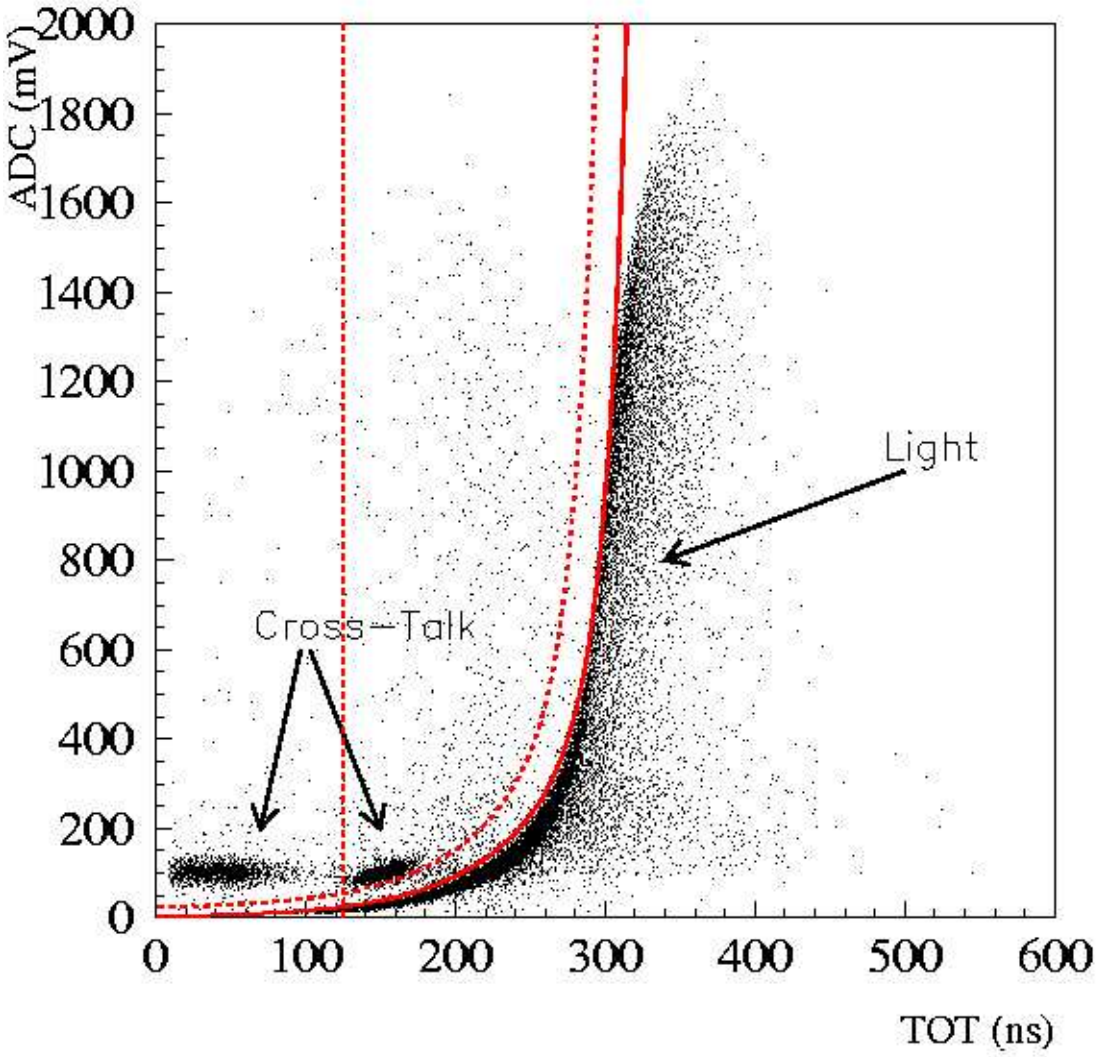

Figure 6.2: A demonstration of cross talk. The data points that cluster to the bottom-left of the solid curve are from cross talk. Taken from [48].

After the cross-talk cleaning was applied, two reconstructions were performed on the data. The first was the standard 16-iteration maximum likelihood reconstruction described in section 5.2. The second was a 16-iteration maximum likelihood reconstruction with a Bayesian weighted prior as described in section 5.2.2. Events that had a likelihood ratio $\mathcal{L}_{u/d} < 25$ (meaning they were more likely to have been produced by cosmic ray muons) were removed from the data sample.

The data passing rate after this level was 1.0×10^{-4} %. The events removed by this level were mostly mis-reconstructed muons from cosmic rays and those that were triggered by electrical crosstalk.

6.5.2 Level 4 - Coincident Muons

The raw trigger rate of cosmic rays is $\sim$ 100 Hz. That means every once in awhile two muons will enter the detector within a time scale of $\sim$ 5 μsec, close enough that they are treated as one "event" even though they are from two independent air showers. An example of a coincident muon event can be seen in Fig. 6.3. A detailed calculation of the rate at which these coincident muon events trigger the detector was performed in [50]. That rate was determined to be 0.69 per second.

At trigger level, the contribution from coincident muon events is quite low. Unfortunately, the criteria applied to events consider only a single muon hypothesis. This leads to an enhancement of the contribution from coincident muons at higher levels of the analysis. Therefore, a cut is applied at level 4 to reduce the

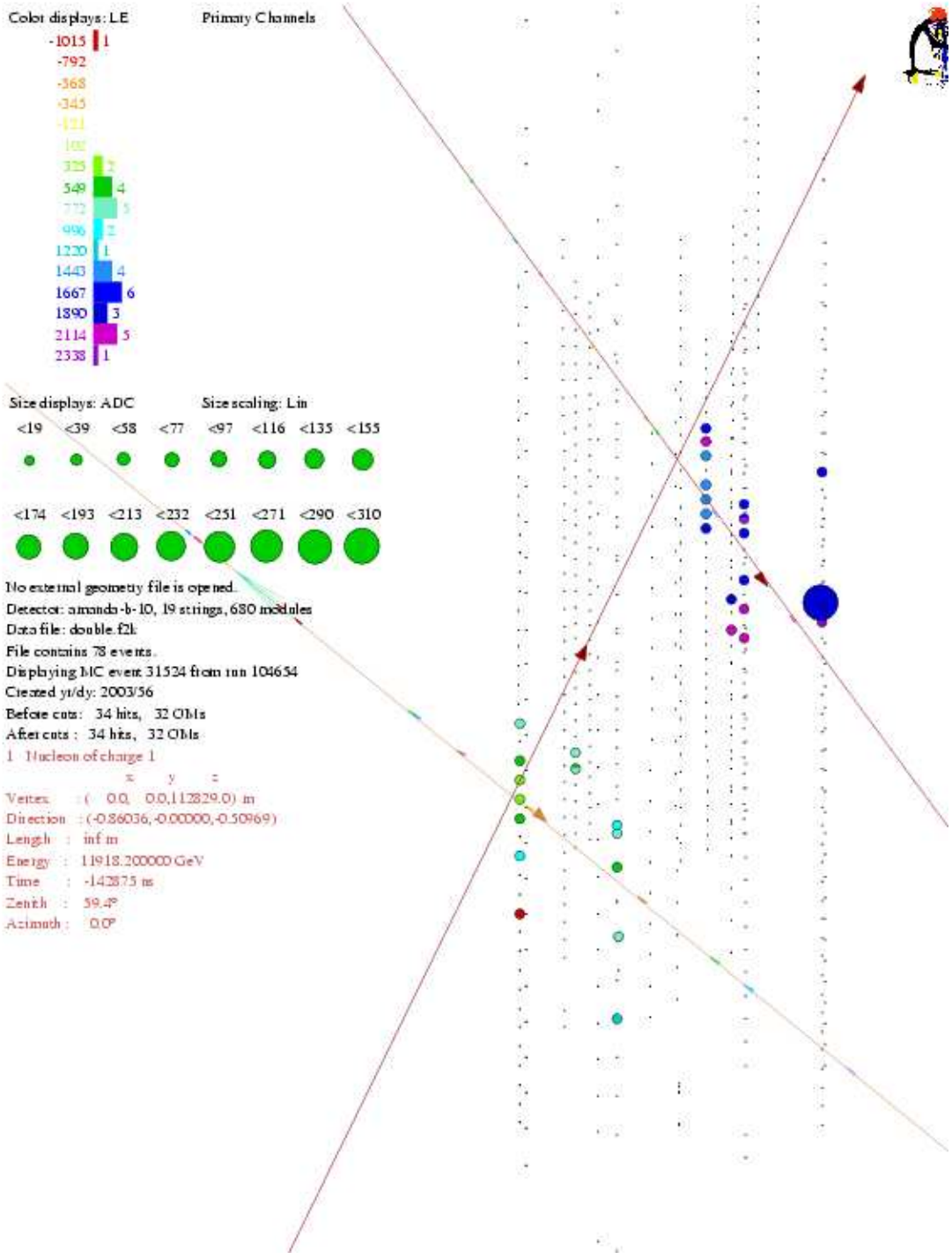

Figure 6.3: Example of a coincident muon event in the AMANDA-II detector.

coincident muon background contribution. That cut is a two-dimensional cut on zenith angle and the number of direct hits:

$$zenith(u) - zenith(d) < 18.0 \times [ndirc(u) - ndirc(d)] \tag{6.7}$$

where u represents the standard 16-iteration maximum likelihood reconstruction and d represents the Bayesian reconstruction. This cut is demonstrated in Fig. 8.1.

6.6 Simulations

Generation of events, both neutrino and cosmic ray, occurs in three steps. First muon and neutrino events are generated. Then they are propagated through the ice to the detector. Finally, the detector response is simulated.

6.6.1 Muon Generation

Atmospheric muons are simulated using the generator `CORSIKA` [51]. The cosmic ray spectrum was assumed to be isotropic with a spectral index of $\gamma = 2.73$ and energies between 8×10^2 to 1×10^9 GeV nucleon^{-1}. The interaction model used was `QGSJET`.

Simulating air showers requires an enormous amount of computer resources. The flux of cosmic ray primaries is isotropic and muons with energies above 600 GeV are deflected less than 1 degree. For these reasons, an event generated with `CORSIKA` is used multiple times by randomizing the azimuth angle and horizontal coordinates with respect to the detector. An oversampling factor of 100 was

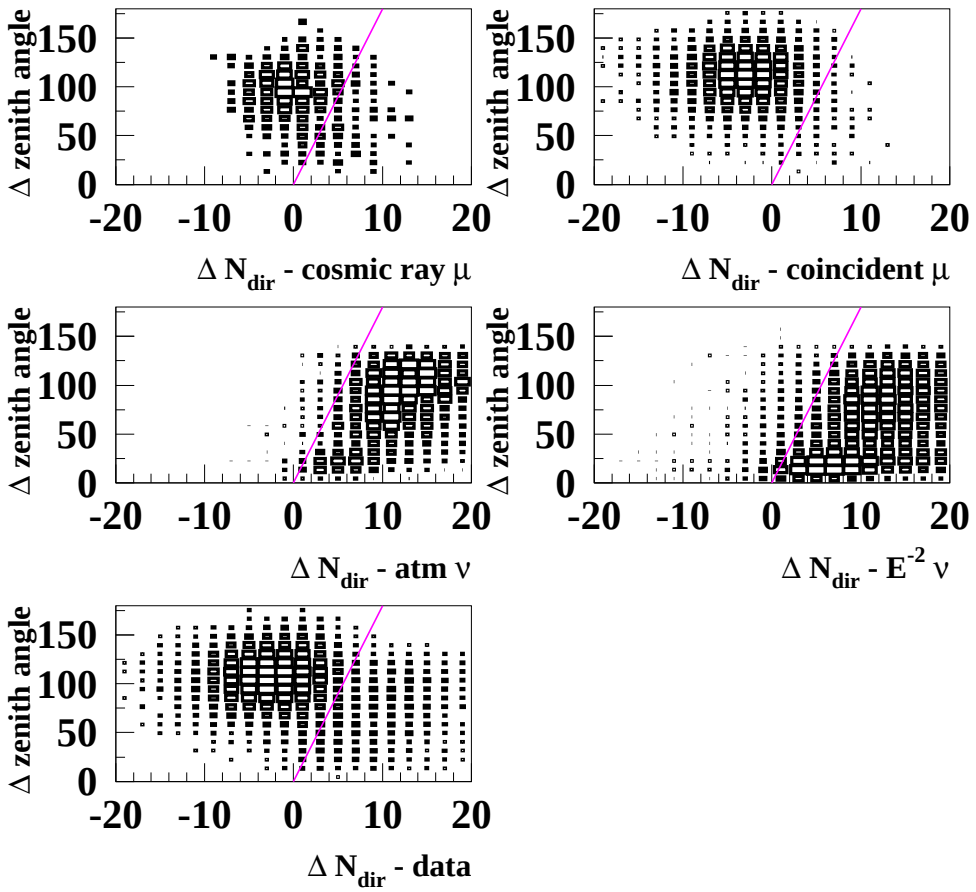

Figure 6.4: Events to the left of the line are primarily due to mis-reconstructed cosmic ray muons and coincident muons.

used for this work. Physics fluctuations due to this oversampling rate are small compared to fluctuations due to the geometry and photon propagation.

Muons from neutrino events with energies between 10 GeV and 10 PeV are generated using `NUSIM` [52]. Not only does `NUSIM` generate neutrinos, it also propagates the neutrinos through the earth and simulates their interactions with nucleons. If a neutrino-nucleon interaction takes place in the earth, `NUSIM` will also propagate the muon through the rock to the rock-ice boundary using the `MUDEDX` code, which is based on tables calculated by Lohmann in [53].

6.6.2 Photon Propagation

Photon propagation in AMANDA is done using the program `PTD` [43]. The results of this program, mean amplitudes and arrival time distributions as a function of relative distance and orientation of the receiver, are stored in large multi-dimensional archives. These archives are known as the photon tables.

6.6.3 Muon Propagation in Ice

Muons from both neutrinos and cosmic rays are propagated through the ice and detector using `MMC` [54]. This program is capable of propagating muons that have energies from 105.7 MeV to 10^{11} GeV. Stochastic and continuous energy losses are calculated for particles with $\Delta E > 100\,\text{MeV}$. If $\Delta E < 100\,\text{MeV}$ only continuous energy loss due to ionization is taken into account. Ideally, all energy losses would be treated stochastically. However, as the energy of the particle increases, the number of separate energy loss calculations increases, which increases

the computation time [55]. The calculation of the muon's energy loss as it travels through ice is valid to within 1%.

6.6.4 Detector Response

The detector response to muons beginning with the PMTs and ending with the DAQ system is simulated using `AMASIM` [56, 57]. Rather than generating the timing and number of photon information for each OM itself, `AMASIM` gathers this information from tables generated by PTD.

Simulated parts of DAQ include the OM itself, the cable connecting the OMs to the surface electronics, the SWAMPs (Swedish amplifiers), the discriminators, the TDCs, the peak-sensing ADCs, and the trigger logic. A complete list of detector details and parameters taken into account by `AMASIM` is too long to list here. Even though much care has gone into producing the details of the detector simulation, more work needs to be done.

Some of the parameters needed for the simulation of the detector include positions of the optical modules and cable lengths. For simulating the OMs themselves, one also needs the noise rate, relative sensitivity, 1 photo-electron level, and the after-pulse probability of each OM.

Chapter 7

Atmospheric Neutrinos

Before embarking on the task of searching for high energy neutrinos from diffuse astronomical sources, it is imperative to have an understanding of the diffuse flux of neutrinos produced in Earth's atmosphere. These atmospheric neutrinos are not only a background to any search for high energy neutrinos, they also provide a known source which can be used to further understand and calibrate the detector.

Figure 7.1 shows the energy and zenith angle distributions of atmospheric neutrinos for 197 days, which corresponds to the detector live-time of AMANDA-II for the year 2000. The energy spectrum of atmospheric neutrinos is steeper than that of their parent cosmic rays. The reason for this is that at high energies ($\sim$ TeV), the pions that decay to produce neutrinos at lower energies start to interact rather than decay. The zenith angle distribution shows a peak in the atmospheric neutrinos near the horizon due to the longer flight times through the atmosphere that mesons have near the horizon.

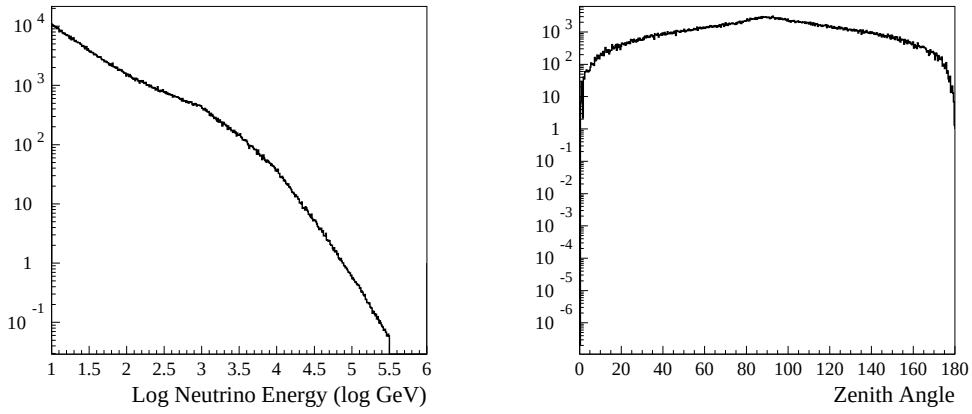

(a) Energy distribution of atmospheric neutrinos.

(b) Zenith distribution of atmospheric neutrinos.

Figure 7.1: The energy and zenith angle distributions of atmospheric neutrinos simulated for 197 days.

7.1 Level 5 - Event Quality

The basic tools used to determine the purity of any particular data set are simulations of cosmic ray muons, simulations of neutrinos, and the event viewer. Ideally, Monte Carlo simulations of down-going muons from cosmic rays and neutrinos alone would determine the purity. However, the simulations, although up-to-date with currently accepted theoretical models, are not accurate enough to be accepted at face value. One example of this is the atmospheric neutrino flux, which is input to the signal Monte Carlo. It has an uncertainty of 25% [58] at energies above 1 TeV.

The discrepancy between the Monte Carlo simulations and the data can be seen in Fig. 7.2. Plotted in this figure are the data and results from cosmic ray

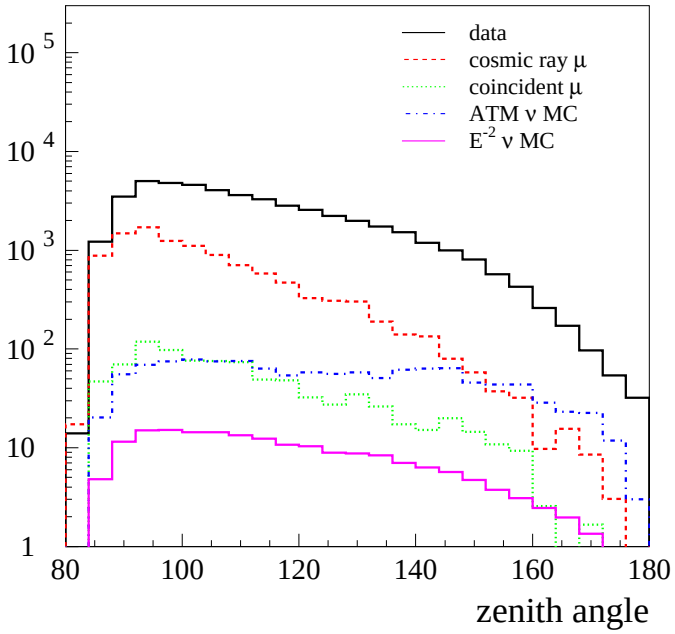

Figure 7.2: The zenith angle distribution plotted for events passing level 4 criteria.

muon, coincident muon, atmospheric neutrino, and E^{-2} neutrino Monte Carlo simulations. By summing the simulation results in this figure, it is clear that the simulations alone can not account for all of the data events.

For these reasons, the idea of *event quality* was developed and applied at level 5 of this analysis. At first the quality cuts are applied loosely and deemed level 5.1 (level 5 processing, quality level 1). The cuts are then gradually tightened until level 5.8 (level 5 processing, quality level 8), where there are a handful of the best neutrino candidates left. This method is independent of the normalization to the neutrino flux discussed in 7.2. Figures 7.3 and 7.4 show that as the quality parameters are tightened, the rate of change in the Monte Carlo and data begins to agree. This trend can also be seen in table 7.1.

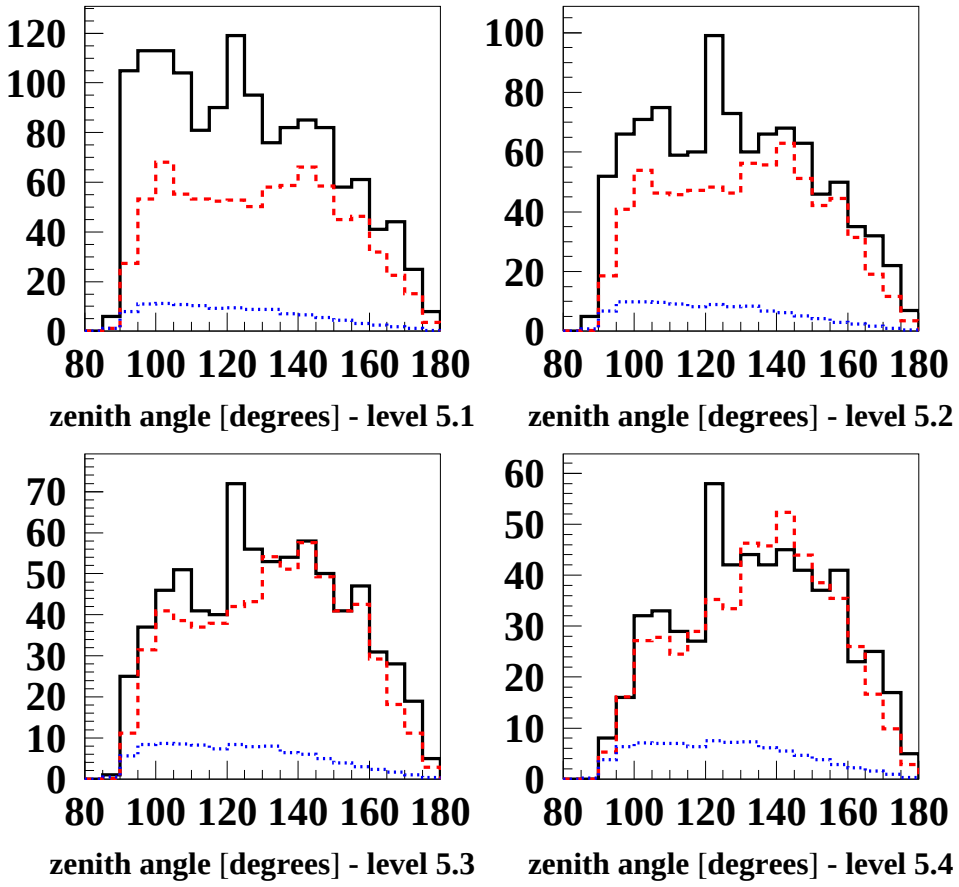

Figure 7.3: The zenith angle distribution plotted for levels 5.1 - 5.4 As quality parameters are tightened, data and Monte Carlo simulations come into agreement. The solid line represents data, the dashed line represents atmospheric Monte Carlo simulations, and the dotted line represents the E^{-2} Monte Carlo simulations.

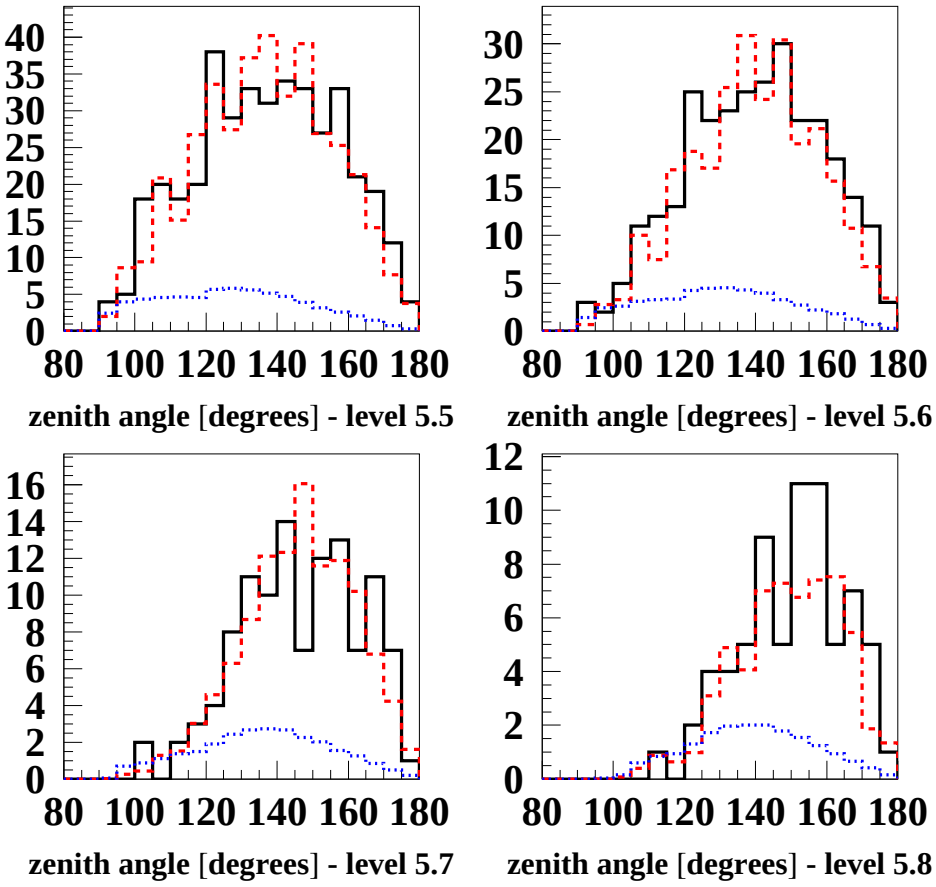

Figure 7.4: The zenith angle distribution plotted for levels 5.5 - 5.8 As quality parameters are tightened, data and Monte Carlo simulations come into agreement. The solid line represents data, the dashed line represents atmospheric Monte Carlo simulations, and the dotted line represents the E^{-2} Monte Carlo simulations.

Table 7.1: Passing rates of data and Monte Carlo simulations for various quality levels. The neutrino Monte Carlo has been normalized as described in 7.2.

Level	Data	Atm. MC	E^{-2} MC	Atm μ MC	Coinc. μ MC
5.1	1388	819	121	69	68
5.2	1009	726	111	33	38
5.3	755	639	101	13	17
5.4	565	516	88	6.1	9.8
5.5	400	391	66	0	3.1
5.6	287	265	50	0	0.7
5.7	112	113	27	0	0
5.8	70	60	18	0	0

Before discussing the cuts developed at this level, it should be mentioned that cuts for levels 5.1 - 5.5 were based on 16-iteration maximum likelihood and Bayesian reconstructions. The level 5.5 - 5.8 cuts were based on more accurate 64-iteration maximum likelihood and Bayesian reconstructions.

There are a total of 6 quality cuts used in this analysis. Four of these cuts are one-dimensional. They are used to remove mis-reconstructed cosmic rays and coincident muons. All cuts used are based on the quality parameters described in section 5.3.

$$R_L^{u/d} = \log \frac{\mathcal{L}_{up}}{\mathcal{L}_{down}} > 35 \tag{7.1}$$

$$L_{dir}^{[-15:25]} > 155 \tag{7.2}$$

$$|S_{phit}| < 0.275 \tag{7.3}$$

$$N_{dir}^{[15:75]} > 10 \tag{7.4}$$

Distributions comparing the data to Monte Carlo simulations of atmospheric

neutrinos and E^{-2} of the one-dimensional cuts are shown in Figs. 7.5 - 7.8. In each of these figures, all cuts are applied except the one plotted. A vertical solid line represents the level of cut selected for the quality parameter in each plot. These plots have been constructed using the 100 percent data sample at level 5.5. In each plot, the number of Monte Carlo events have been normalized (see section 7.2) to the number of data events observed.

In addition to the one-dimensional cuts described above, a pair of two-dimensional cuts are applied to the analysis. The first of these cuts was developed to remove unsimulated background events that fired more than 50 optical modules as they passed through the detector. This effect is shown in Fig. 7.9. Examining these events more closely revealed that they had positive values of the smoothness parameter as seen in Fig. 7.10. This meant that most of the light in the event was deposited in the second half of the track. The exact cause of these events is not fully understood. However, these events tend to be more spherical in nature (indicating shower-like behavior) and they also have shorter track lengths.

The following cut was developed to remove these events and is applied only to events that have more than 50 optical modules fired and positive smoothness.

$$L_{dir}^{[15:75]} < 4.3 * (\log \frac{\mathcal{L}_{track}}{\mathcal{L}_{shower}}) - 65 \tag{7.5}$$

The diagonal line in Figure 7.11 demonstrates the cut made to remove these events and figure 7.12 shows one of the events removed by this cut.

The final cuts were developed to ensure that events passing through only the very bottom or very top of the detector (where the optical modules are not

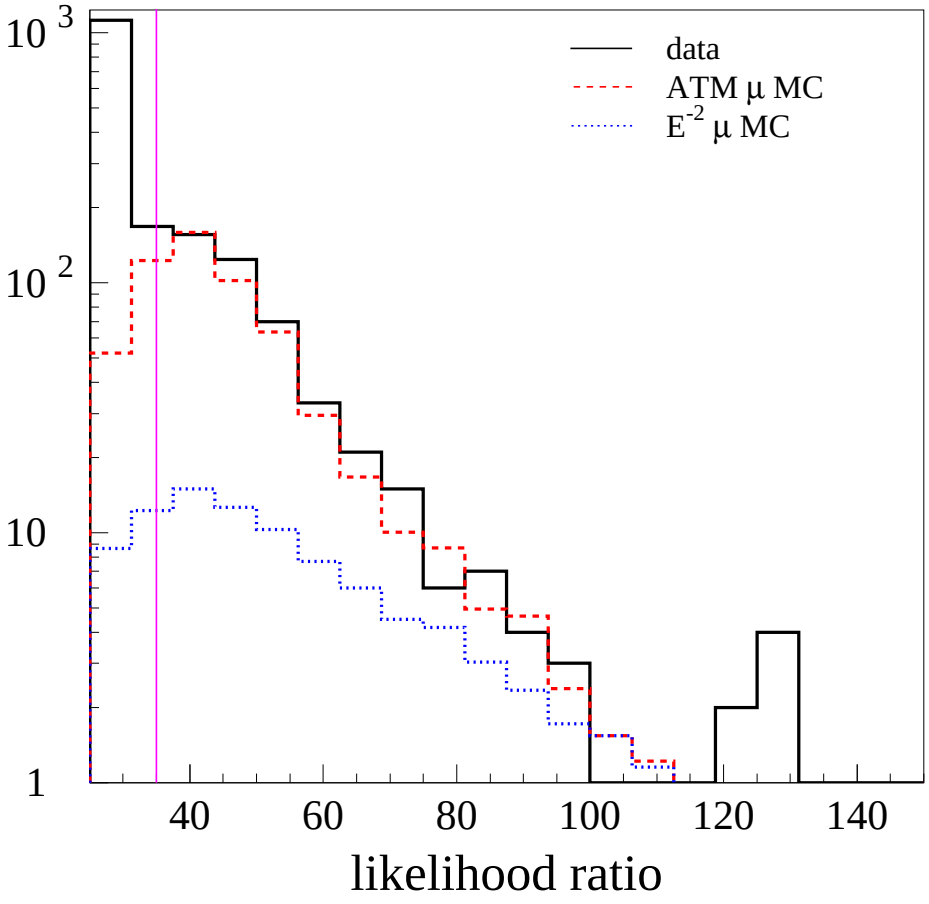

Figure 7.5: The likelihood of the events being up-going. Events to the right-hand side of the plot are most likely to be from up-going neutrinos. An excess of data events at lower values than the Monte Carlo simulations indicates that these events are likely to have been produced by down-going mis-reconstructed muons from cosmic rays rather than up-going neutrinos. Events to the left of the vertical solid line are removed.

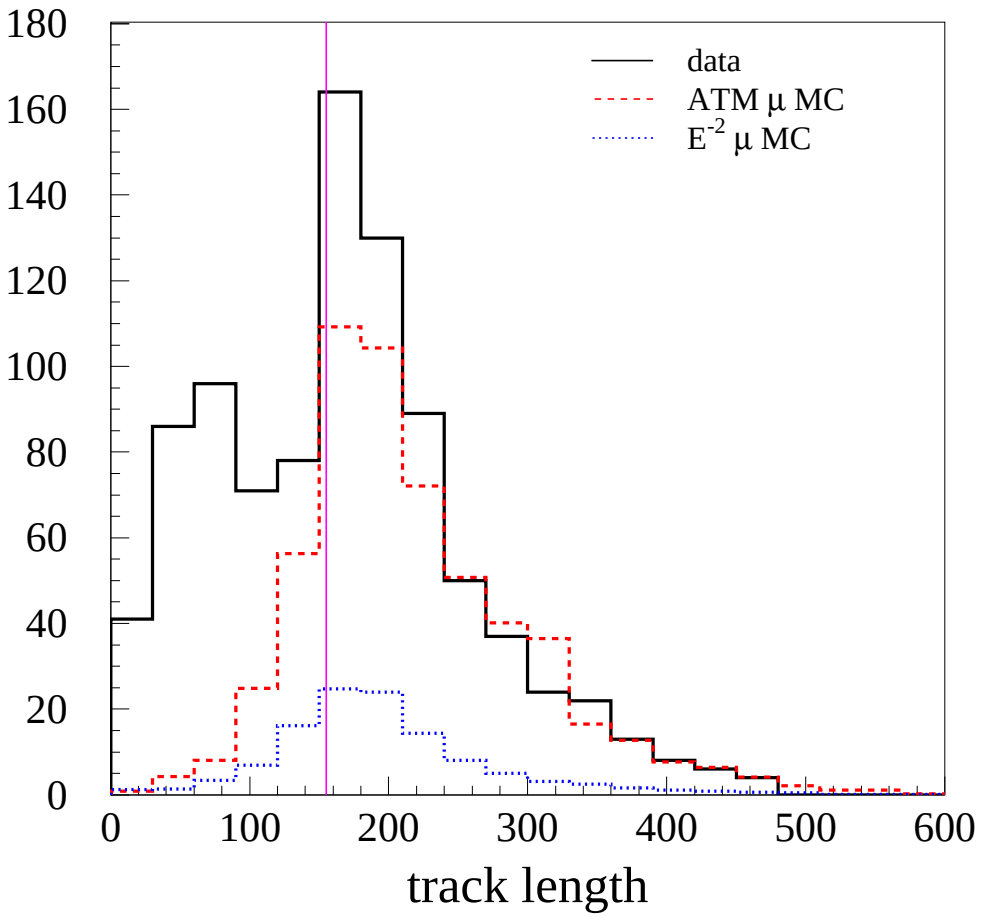

Figure 7.6: The distance covered by the muon passing through the detector. Many mis-reconstructed tracks have lengths less than 155 meters. Events to the left of the solid vertical line are removed.

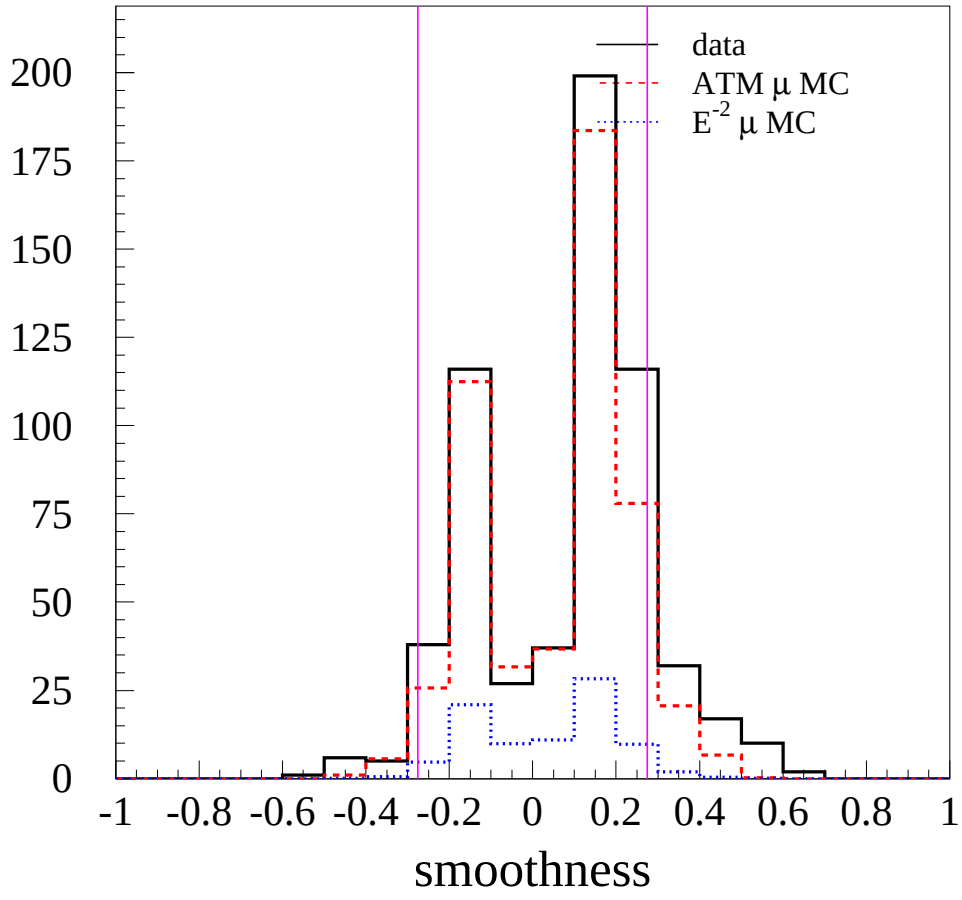

Figure 7.7: The distribution of the smoothness of the events in the detector. High quality tracks have smoothness values near 0. Events between the two solid vertical lines are kept.

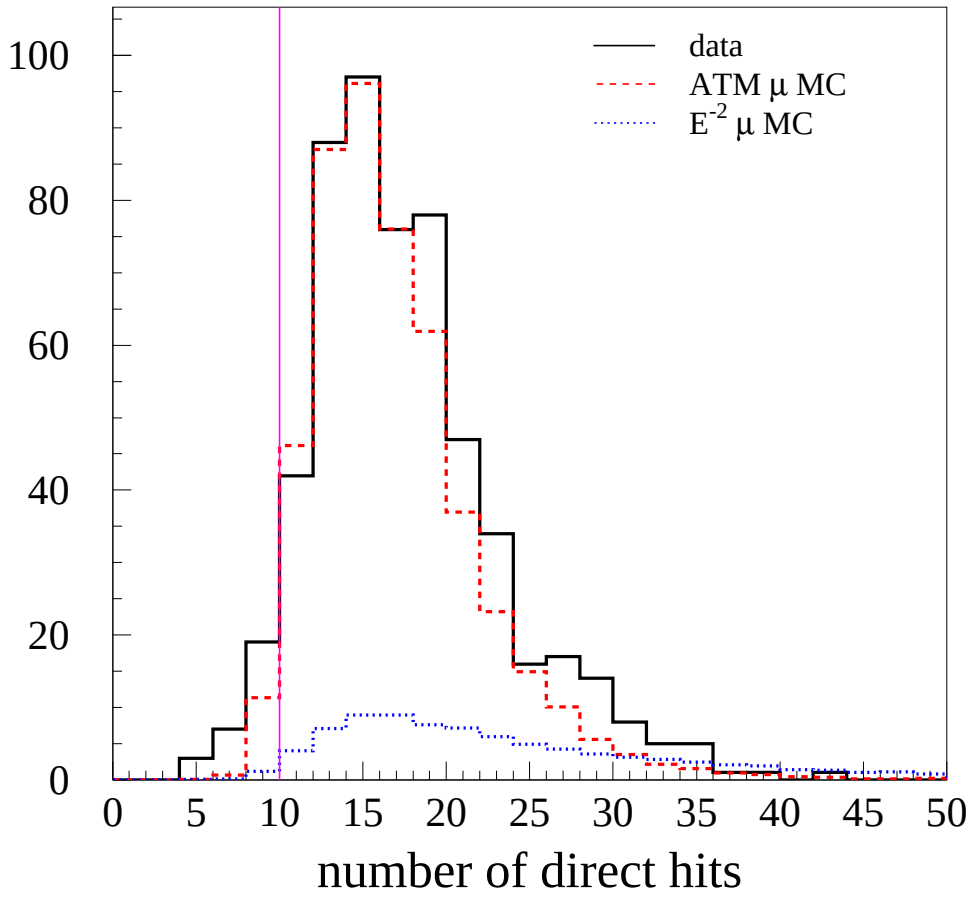

Figure 7.8: The number of hits in the detector with time residuals between -15 and 75 ns. A track with high quality would have many "direct" hits. Events to the left of the solid vertical line are removed.

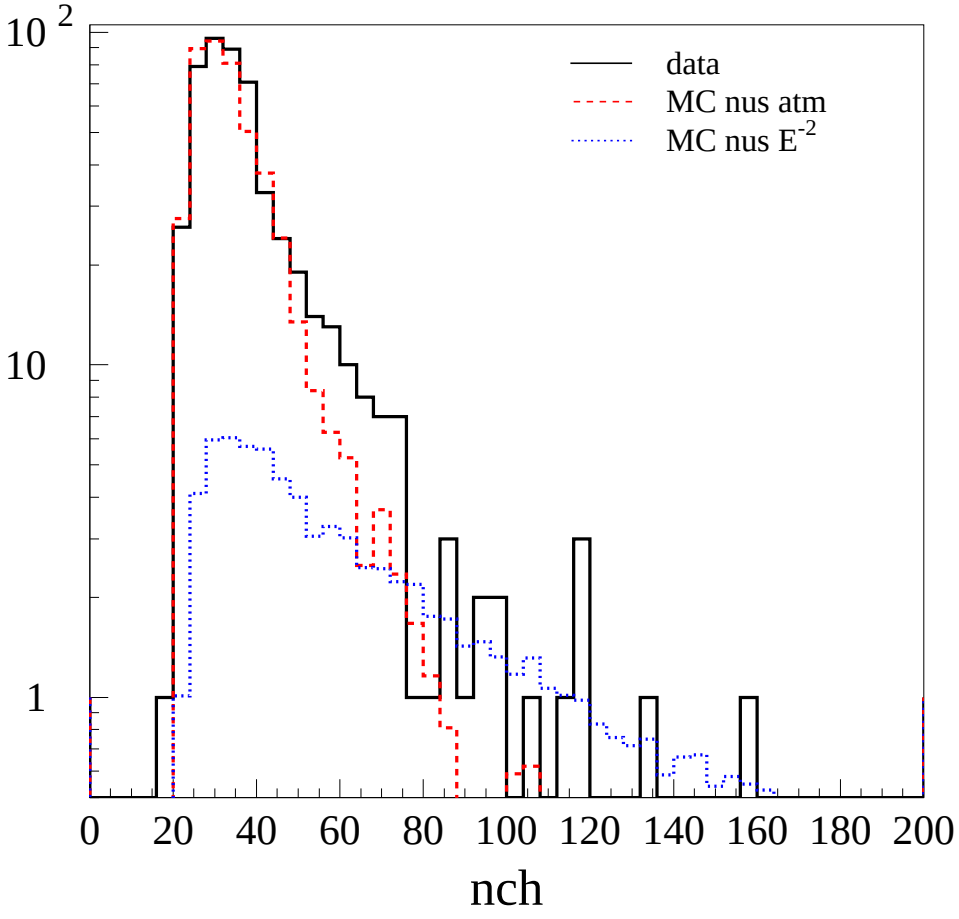

Figure 7.9: This figure demonstrates the disagreement between data and Monte Carlo simulations for events that have more than 50 optical modules fired.

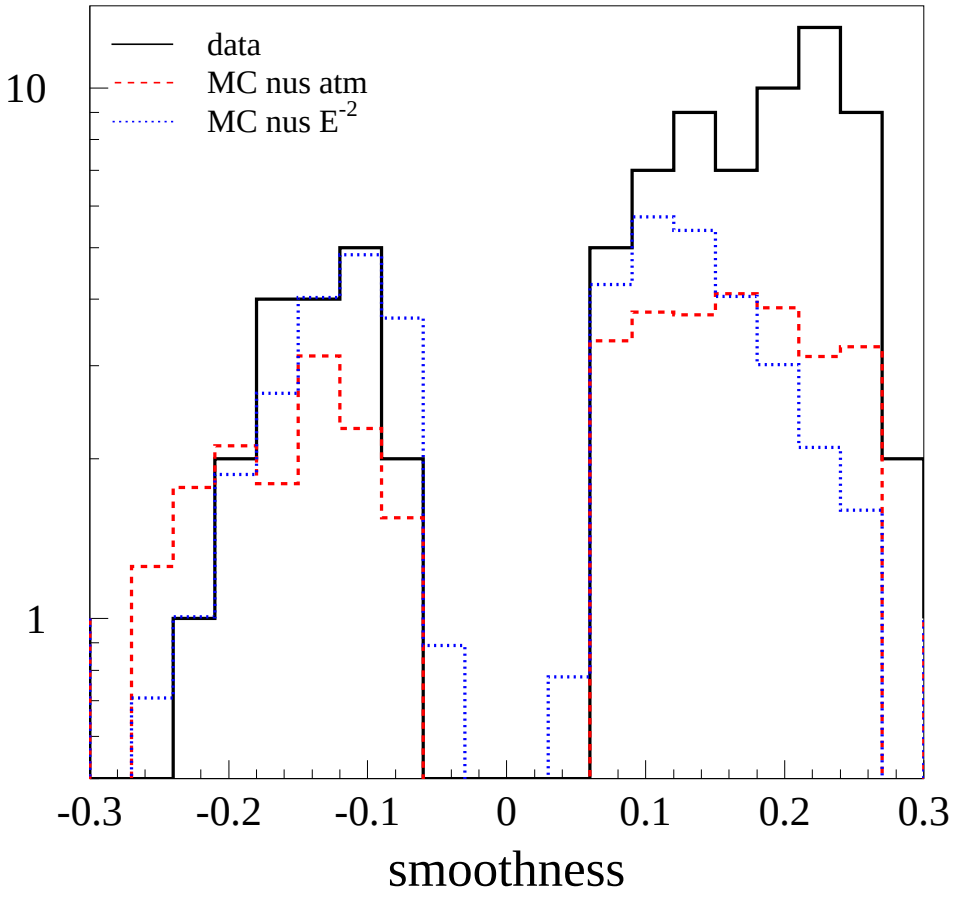

Figure 7.10: This figure shows the disagreement in the smoothness distribution for events that had more than 50 optical modules fired.

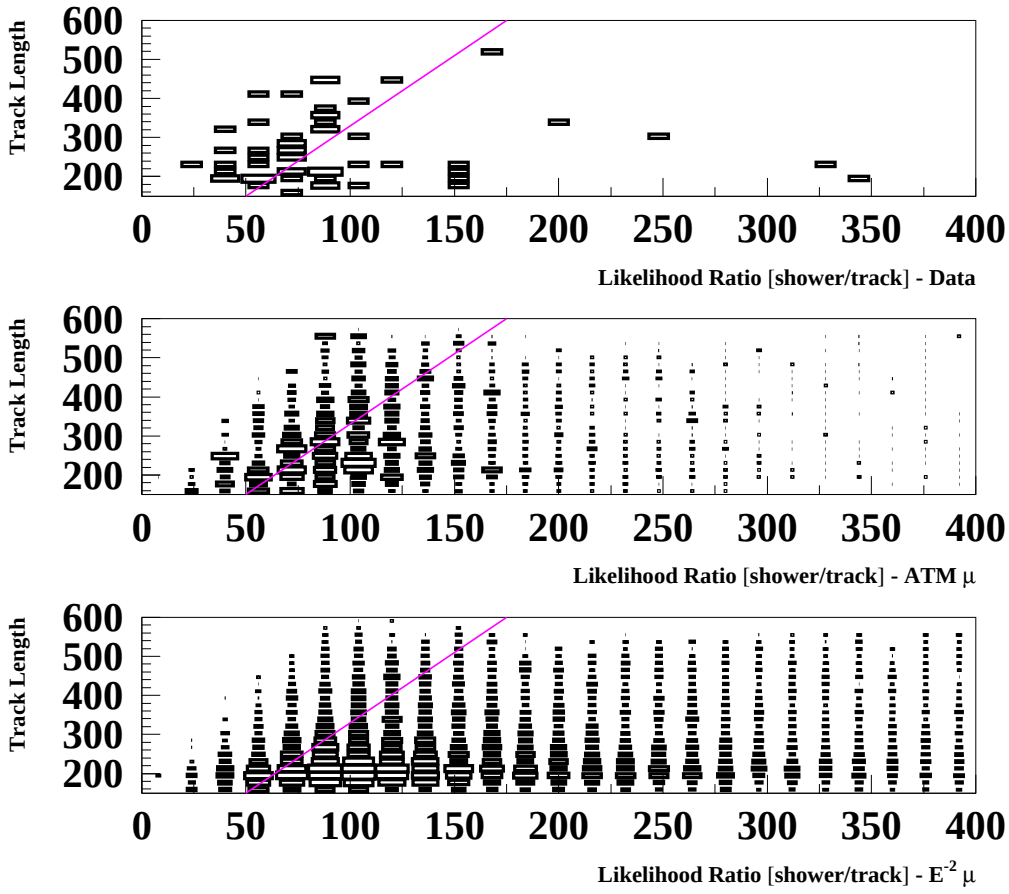

Figure 7.11: The direct length versus the negative log likelihood ratio of the the events being track-like to shower-like plotted for events with at least 50 optical modules fired and positive smoothness. Events above and to the left of the solid line are removed.

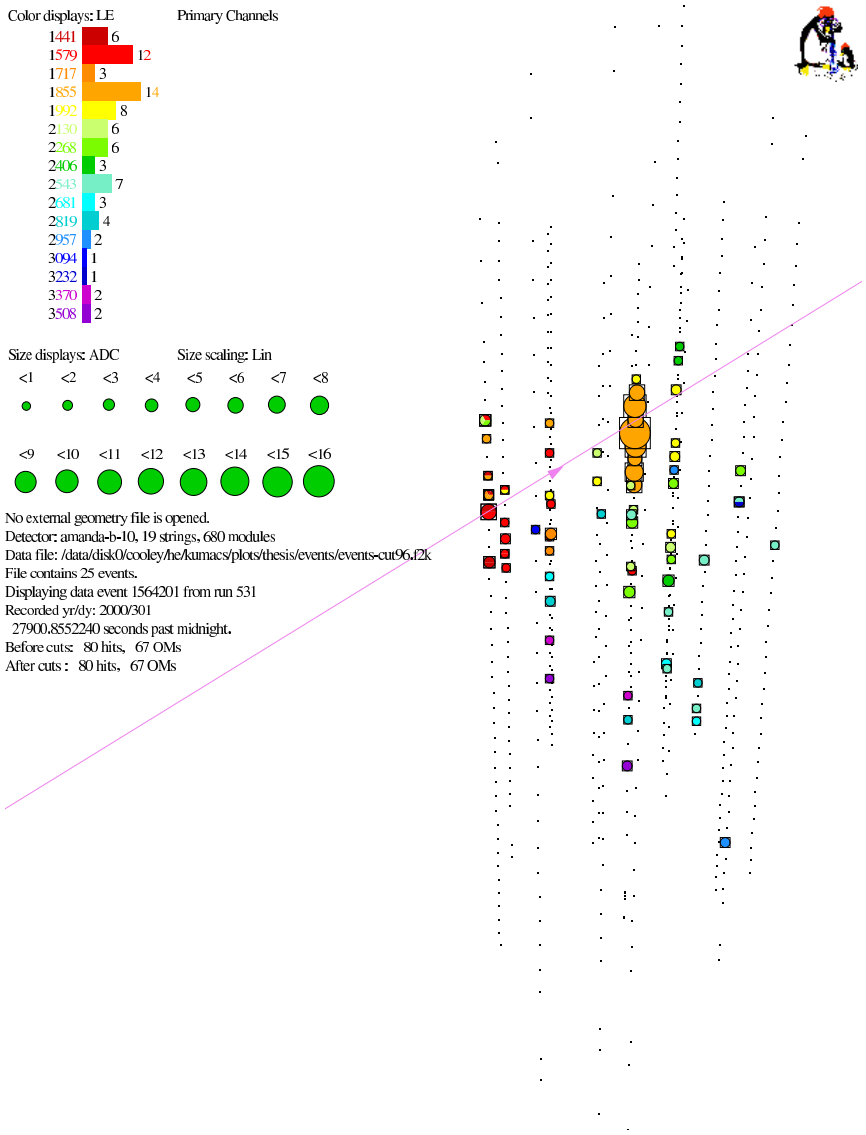

Figure 7.12: An event removed by the 2D cut on the length of the event versus the track-to-shower likelihood ratio applied to events with more than 50 optical modules fired which had a positive value of the smoothness parameter.

as evenly spaced as the middle of the detector) are from neutrinos and not misreconstructed comsic rays. These additional cuts were applied to tracks that had a zenith angle less than 120 degrees.

$$R_L^{t/s} = \log \frac{\mathcal{L}_{track}}{\mathcal{L}_{shower}} > -1.1 * cogz - 27.5 \tag{7.6}$$

$$cogz < 150. \tag{7.7}$$

These cuts are shown as solid lines in Fig 7.13.

7.2 Normalization

As mentioned in section 7.1, the flux of atmospheric neutrinos is known only to 25%. In order to account for this fact the simulated neutrino flux is normalized to the observed flux of neutrinos. The ratio of the number of data events to the number of simulated events is plotted as a function of quality level in Fig 7.14. At low event qualities (< 4), the data are contaminated by background. At higher quality levels the ratio stablizes at 0.70. This number agrees with the uncertainty in the atmospheric neutrino flux.

7.3 Other Atmospheric Neutrino Models

The model of atmospheric neutrinos used in this analysis was developed by Paolo Lipari [59] in 1992. His model uses analytic methods to compute the spectra of neutrinos and anti-neutrinos produced by cosmic rays in Earth's atmosphere.

In order to investigate the uncertainty introduced by the simulations of atmospheric neutrinos, two other atmospheric models were investigated for this

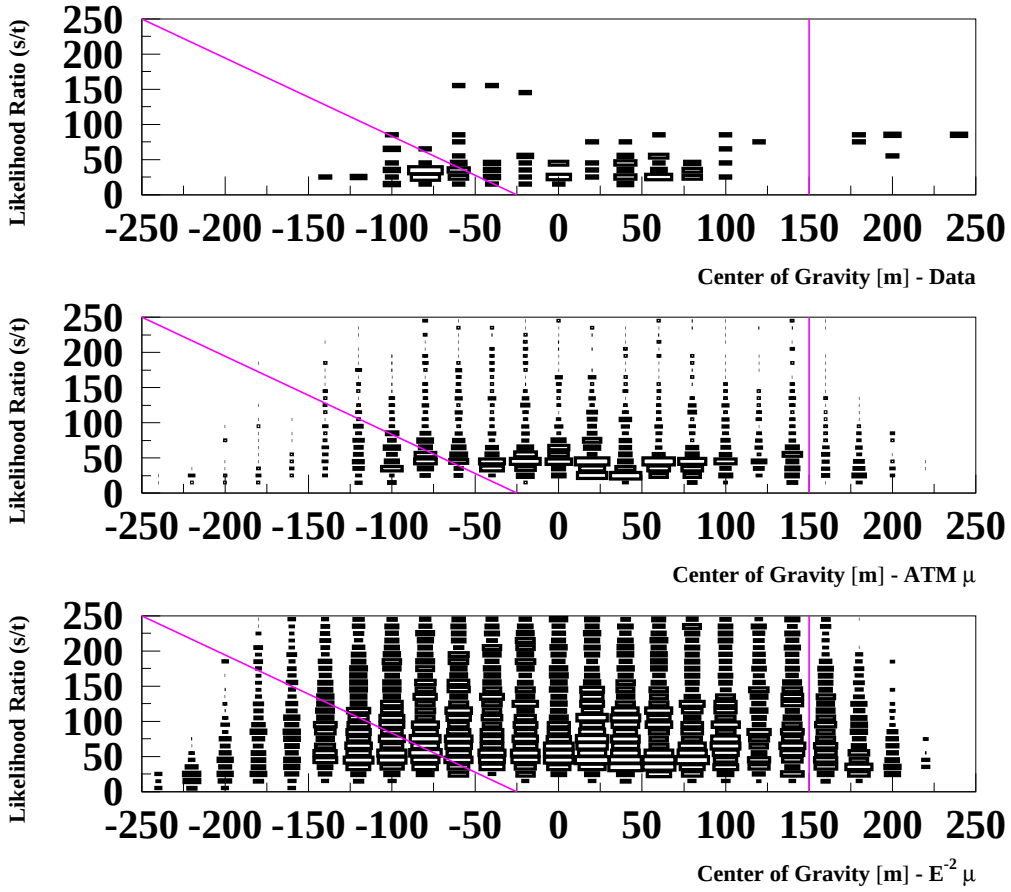

Figure 7.13: The track-to-shower likelihood ratio versus the center of gravity of the event. Events near the top and bottom of the detector, where optical modules are more sparsely placed, are required to demonstrate higher quality than events with center of gravities near the middle of the detector. Events below and to the left of the diagonal solid line and the events to the right of the vertical solid line are removed.

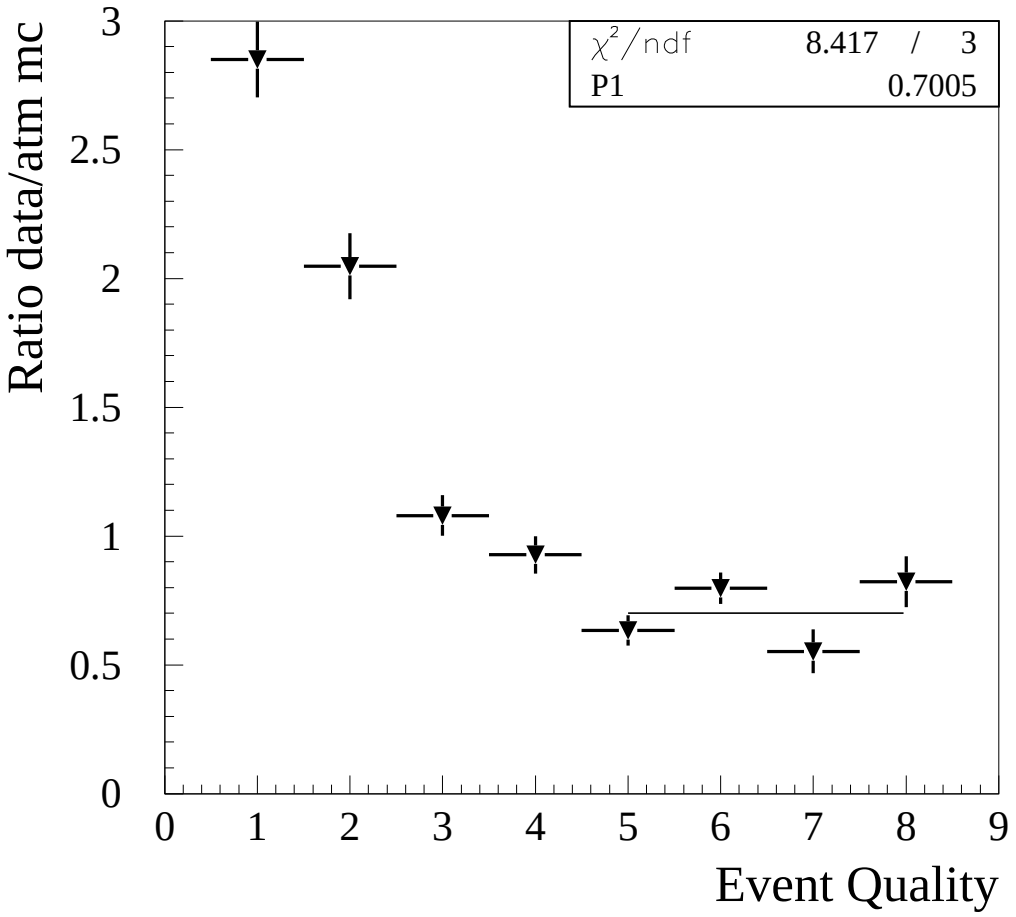

Figure 7.14: The ratio of number of events observed to the number predicted by Monte Carlo simulations of atmospheric neutrinos. The line fit at high event qualities shows the normalization factor used in this analysis.

analysis: one by Honda et al. [60] and the other by Agrawal et al. [61]. These fluxes are known as the "Honda" flux and the "Bartol" flux respectively. Both of these models use Monte Carlo simulations to determine their fluxes. The differences in the models primarily come from the assumed primary spectrum of cosmic rays and the hadronic interaction model in the atmosphere. In calculating the Honda flux, the authors use a higher primary spectrum normalization than that used by the authors of the Bartol flux.

The hadronic interaction model `TARGET` [62] used by the authors of the Bartol flux is a simple phenomenological representation of pion and kaon production in interactions of protons, pions, and kaons with light nuclei. The program uses parameterizations of accelerator data for hadron-nucleus collisions with emphasis on interaction energies around 20 GeV. The authors of the Honda flux used more sophisticated generators designed for studies at accelerators.

In their original work, the authors of the Honda flux calculated fluxes for neutrinos up to 31 TeV in energy and the authors of the Bartol flux calculated fluxes for neutrinos with energies up to 10 TeV, while the Lipari flux is calculated up to 316 TeV. Futher work by Gaisser [63] extended the Bartol flux up to 1 PeV making it easier to compare with the Lipari predictions and with the AMANDA data. Although the Honda flux predictions do not reach as high as those of Lipari and Bartol, one still can make comparisons of trends observed at lower energies. Figure 7.15 shows the absolute flux predictions, meaning the fluxes are not normalized. The difference in number of neutrinos predicted below 31 TeV

in energy between Lipari and Honda is 2.3 % while the difference between Lipari and Gaisser was found to be 23.9 %.

To properly compare the different models for this analysis first one must convert to the energy parameter used for this analysis, the number of optical modules fired. Because of the uncertainty in the prediction of primary cosmic rays that produce atmospheric neutrinos, the observable difference in the models that we are interested in is not the total number of neutrinos predicted, but the spectrum these models predict. Thus, for comparison purposes the models are normalized to each other. Finally, a cut must be placed at a neutrino energy of 31 TeV, since the Honda flux only predicts energies up to that value.

Figure 7.16 shows the results of this analysis. There is no observable difference in the energy parameter of this analysis for the three models tested. The data is plotted against the three different models in Fig. 7.17. The apparent deficit in high values of the number of optical modules fired parameter can be explained by the fact that no energy cut was made for this plot since it is not possible to know the true energy of the neutrino in the data.

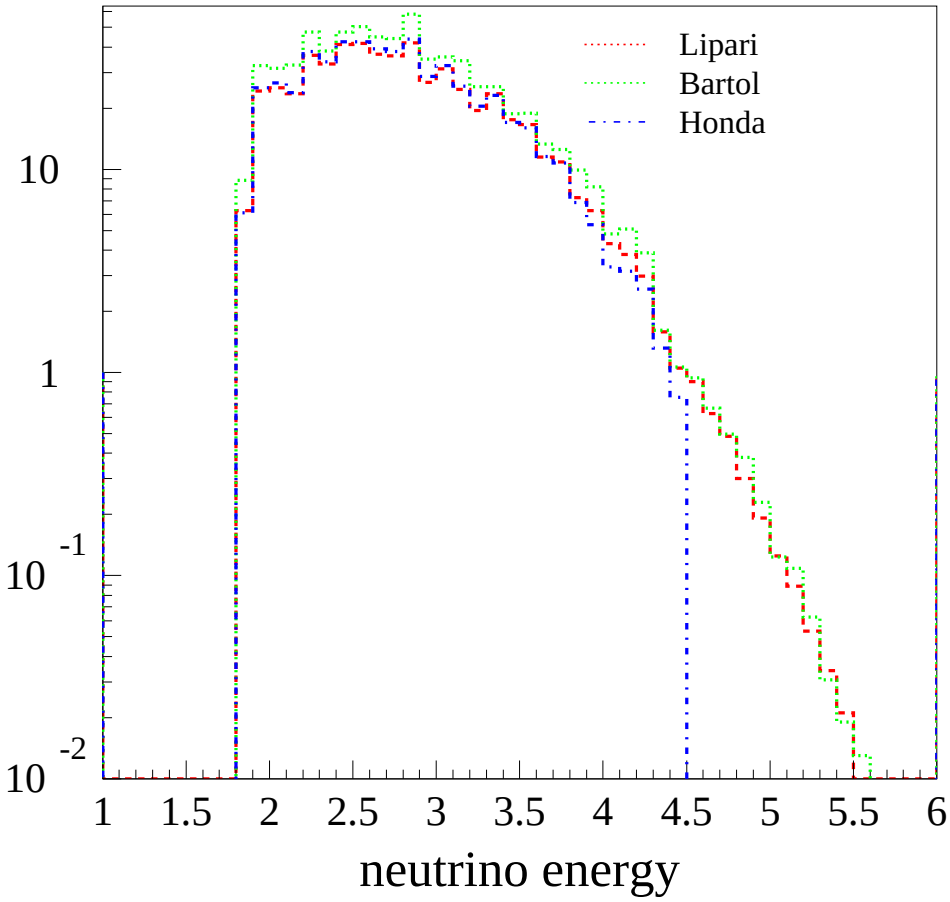

Figure 7.15: Neutrino energy for the three flux predictions used in this analysis. Below 31 TeV the Lipari and Honda fluxes agree to within 2.3 % while the Bartol flux predicts 23.9 % more neutrinos than the Lipari flux.

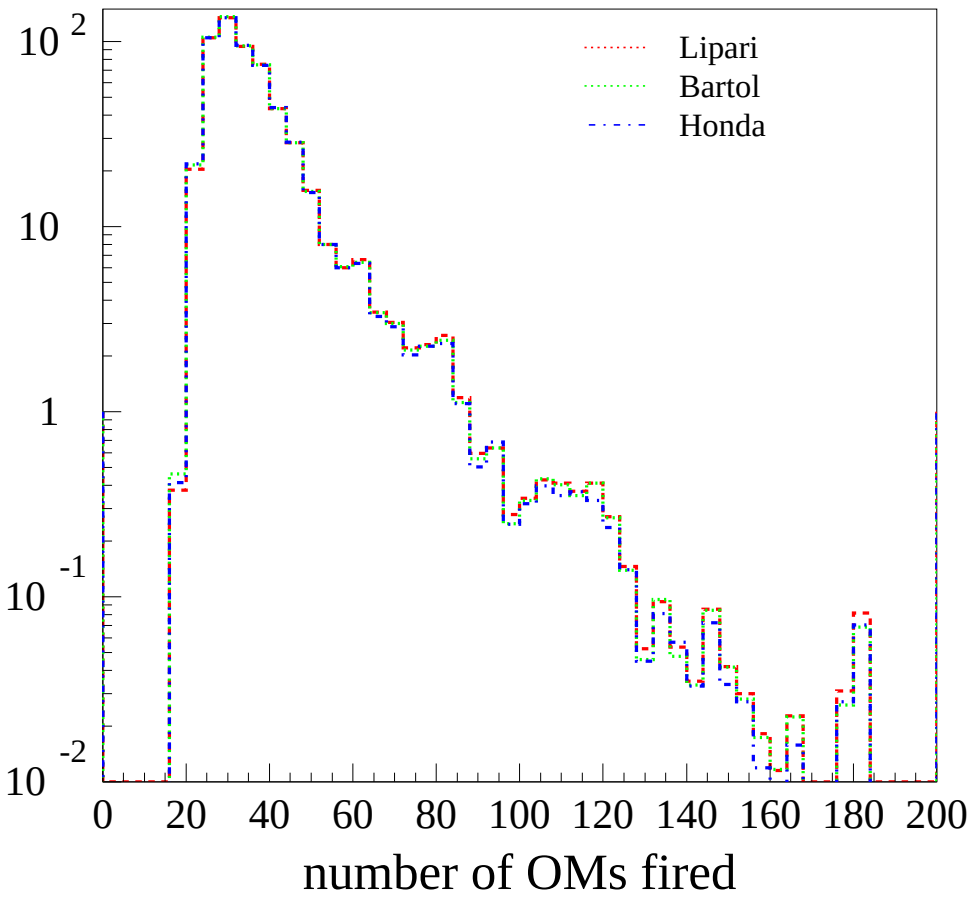

Figure 7.16: The number of optical modules fired for each event for energies less than 31 TeV plotted for the three models tested, Lipari, Bartol and Honda. The number of events for each model has been normalized to the Lipari model.

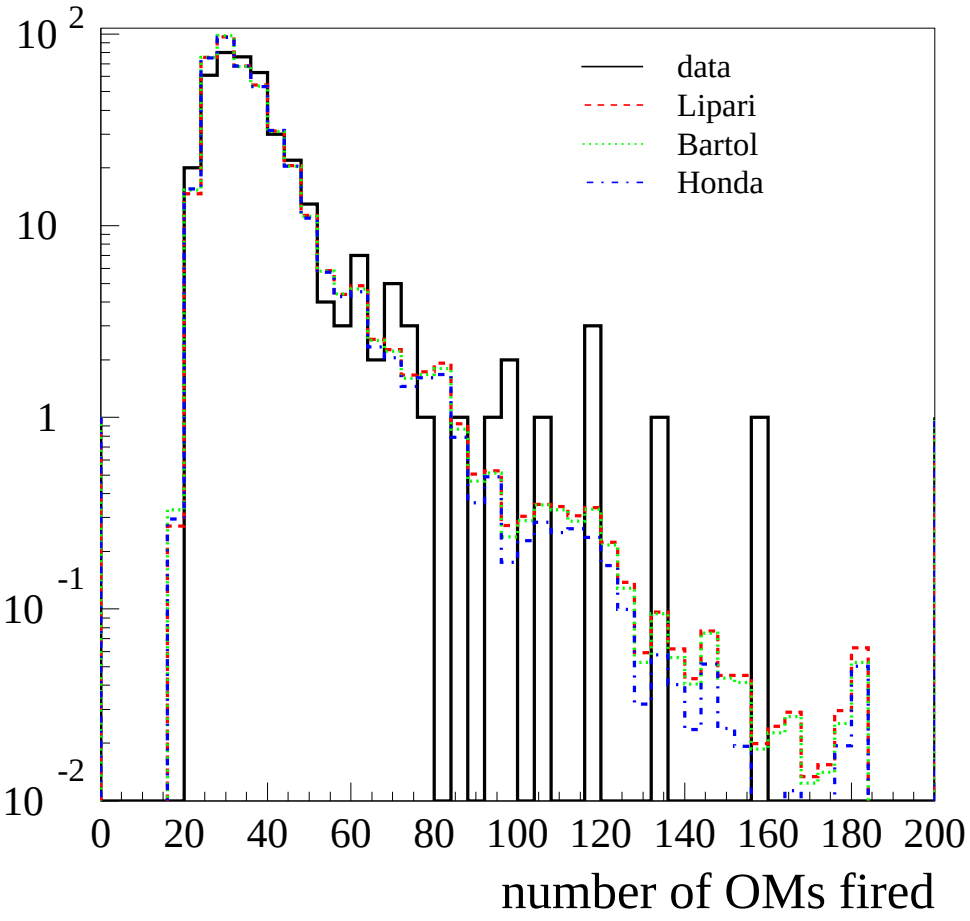

Figure 7.17: The number of optical models fired during each event plotted for data and the three models tested. The models have been normalized to the number of data events.

Chapter 8

Searching for a Diffuse Flux of High Energy Neutrinos

The search for neutrinos from diffuse astronomical sources was done using a blinded analysis technique. This technique required that an unblinded sample (50% of the year 2000 data in this case) be used for developing cuts and analysis techniques, while the remaining 50%, the blinded sample, be untouched until after all cuts and techniques were fixed. The unblinded sample is used for the final analysis and the final result will then be free of any bias introduced by the scientist.

Before presenting the final results, one last review and check on the backgrounds to this analysis will be given as a firm understanding of the backgrounds is crucial for analyses that search for small signals. Then the final cut on energy will be optimized and the sensitivity of the experiment calculated. An effective area will be shown based on the final cut selection and the systematic uncertainties will be discussed. Finally, results will be shown for the assumed E^{-2} neutrino

spectrum followed by a discussion of the results and limits on other high energy neutrino flux models.

8.1 Background Rejection

There are three main backgrounds to this analysis. Two of the backgrounds are muonic in origin - cosmic ray muons and coincident cosmic ray muons. The third background is the atmospheric neutrino background.

8.1.1 Cosmic Ray Muons

Single muons from cosmic rays are rather easy to remove from the E^{-2} signal sample. This analysis used the techniques described in chapter 7 to remove single muons from cosmic rays. At the final cut level there is no contamination expected from single cosmic ray muons.

8.1.2 Coincident Muons

Coincident muons, which occur when two muons from independent air showers enter the detector at the same time and accidentally trigger the detector, are a little more tricky to remove. Using the cuts described in chapter 6, at the level chosen for this analysis (level 5.5), 1.7 events from coincident muons are expected to remain in the sample according to Monte Carlo simulations of these events. However, in the energy range of particles considered in this analysis (see section 8.1.3), no coincident muon particles were observed.

The difficulty in concluding that this background would not affect the final

sample is that it is based on limited statistics. Coincident muon Monte Carlo simulations have been generated for 83.1 days of live-time using approximately 200,000 CPU hours of computation time.

A procedure to extrapolate to larger statistics was developed. This procedure is demonstrated in Fig 8.1. As the selection criteria are tightened, the number of events expected from coincident muons diminishes. In the region of interest for this analysis, an exponential function with a slope of -0.06 can be fit to level 3 and level 4 Monte Carlo simulations of coincident muon events. An assumption was made that this slope would remain constant as the cuts continued to be tightened. Extrapolating to level 5.1 still showed agreement with the simulations. Extrapolating further to level 5.5 gave an expectation of less than a hundredth of an event each year in the signal region. Thus, for this analysis it is assumed that the signal region of high energy neutrinos will not be contaminated by coincident muons.

8.1.3 Background Atmospheric Neutrinos

Atmospheric neutrinos are created during cosmic ray showers in the upper atmosphere. To the AMANDA detector, these neutrinos seem identical to the high energy E^{-2} signal neutrinos in every way except their energy spectra.

This analysis uses an energy parameter to separate diffuse signal neutrinos from the diffuse atmospheric neutrino background. Figure 8.2 uses Monte Carlo simulations to show the energy spectrum of the muon as measured at the center of the detector for signal neutrinos and background atmospheric neutrinos. This

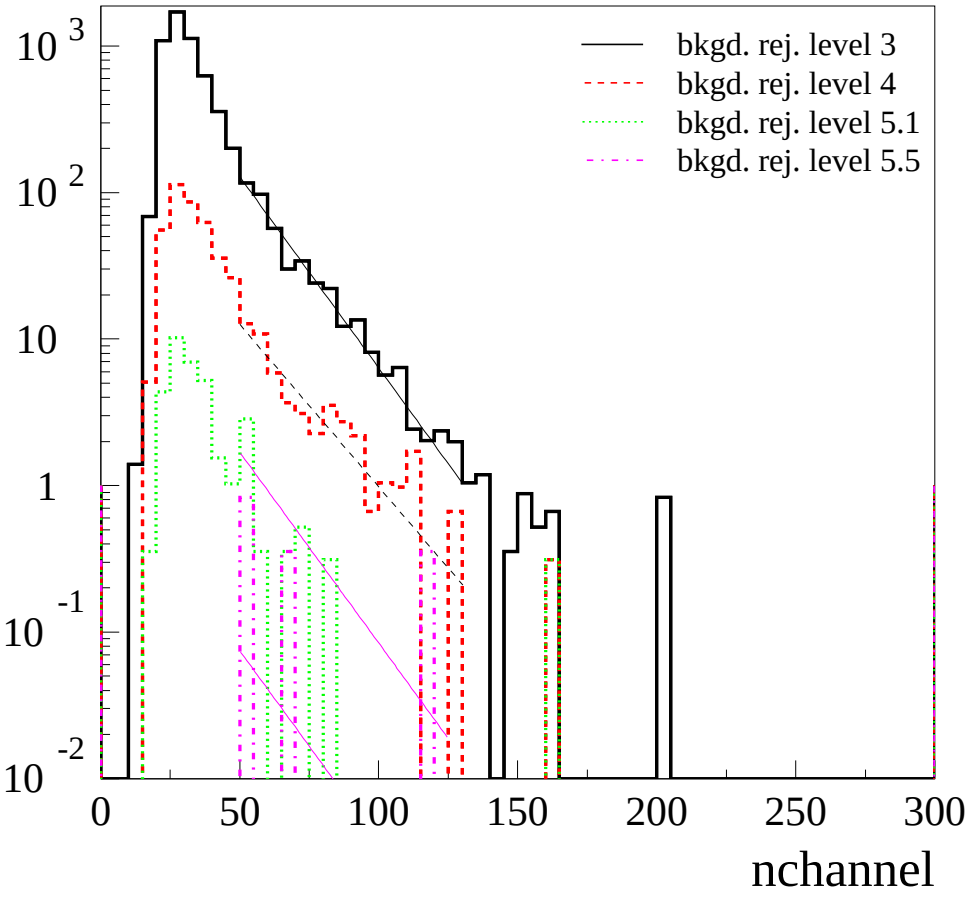

Figure 8.1: As selection criteria are tightened, the number of coincident muon events for a year diminishes. In the region where the number of optical modules fired in events is between 50 and 125, an exponential function can be fit to levels 3 and 4. Extrapolating this function to level 5.1 still shows agreement. Extrapolating to level 5.5 shows an expectation of less than a hundredth of an event each year in the signal region (nch $>$ 80).

plot shows that not only do the signal neutrinos have higher energy than the atmospheric neutrinos, the signal neutrinos have a different spectrum.

A very simple, but effective, energy parameter is to count the number of optical modules fired during an event. This parameter is known as *nchannel*. Figure 8.3 demonstrates the relationship between muon energy at the center of the detector and nchannel using Monte Carlo simulations of neutrino events. Figure 8.5 demonstrates that nchannel is an effective parameter for separating atmospheric neutrinos for E^{-2} signal neutrino events.

8.2 Sensitivity

After deciding how to separate the atmospheric neutrino background from the E^{-2} signal neutrinos, the detector sensitivity can be calculated. The method chosen for this analysis is that of the model rejection potential as described in section 5.4. Sensitivities and cuts based on the number of optical modules fired during an event were calculated. The results of the model rejection potential are outlined in table 8.1.

Table 8.1: Sensitivities and best number of optical modules fired cut for various detector live-times.

Live-time [days]	Best # OMs Fired Cut	Sensitivity [$\mathrm{cm}^{-2}\,\mathrm{s}^{-1}\,\mathrm{sr}^{-1}\,\mathrm{GeV}$]
98.6	80	3.8×10^{-7}
197	87	2.4×10^{-7}
400	89	1.5×10^{-7}
1000	95	0.9×10^{-7}

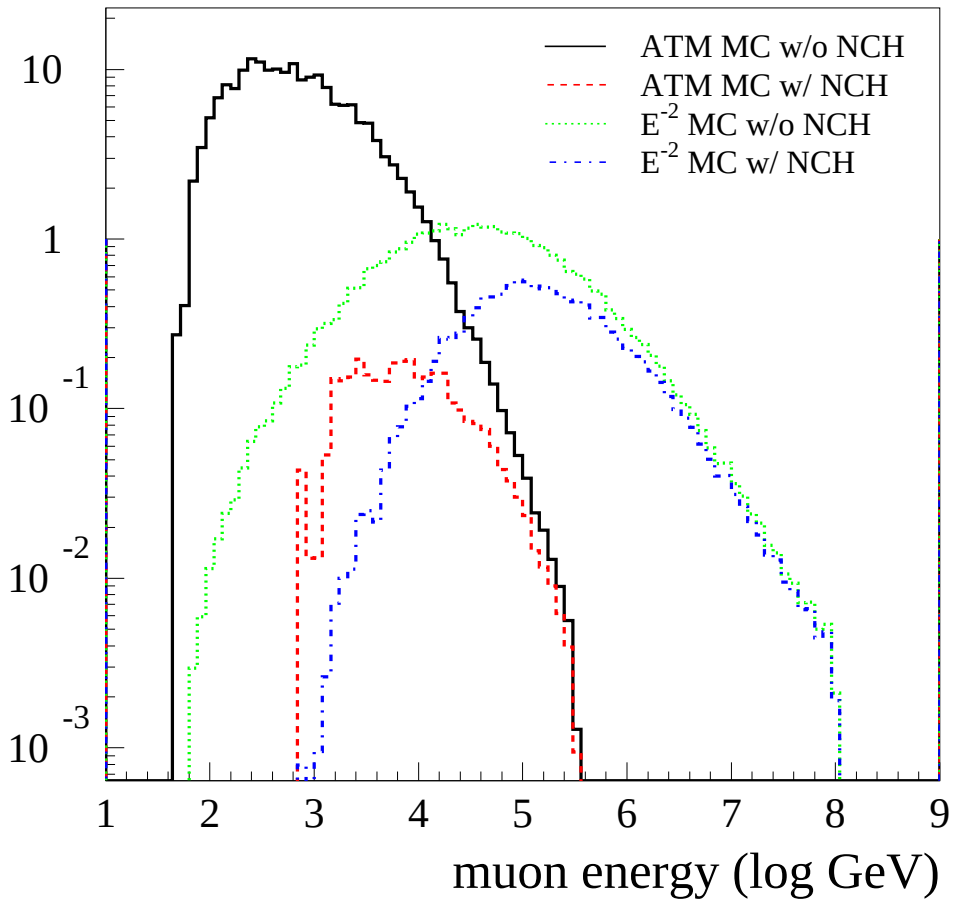

Figure 8.2: The muon energy at the center of the detector for atmospheric neutrinos (background) and E^{-2} neutrinos (signal) before and after the nchannel cut.

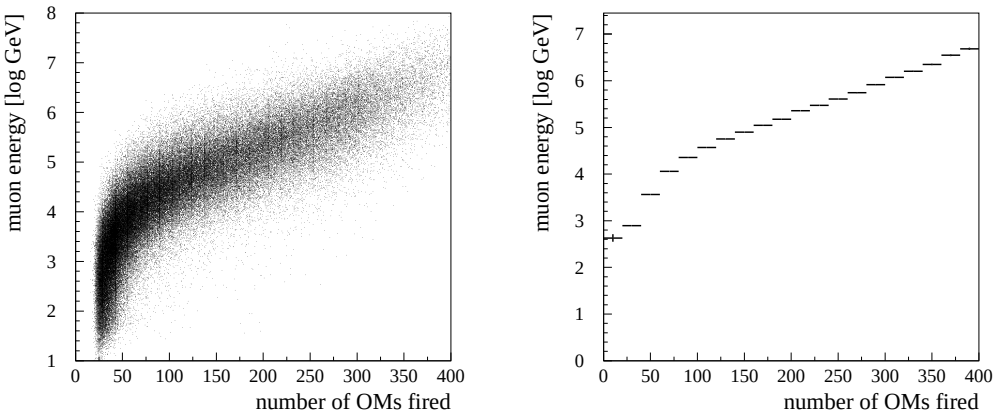

(a) Scatter plot of number of OMs fired versus muon energy at the center of the detector.

(b) Profile plot of number of OMs fired versus muon energy at the center of the detector.

Figure 8.3: The above plots demonstrate a relationship between the number of OMs fired during an event and the reconstructed muon energy at the center of the detector.

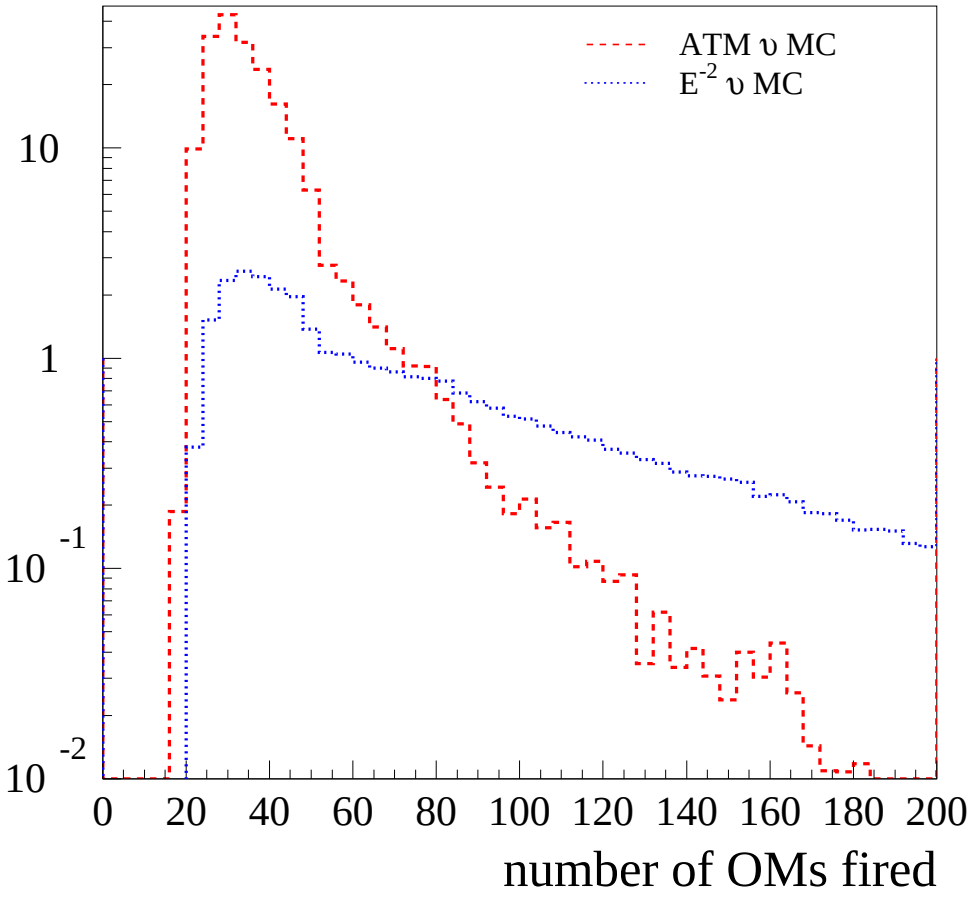

Figure 8.4: The number of optical modules fired during events. The dashed line represents the background atmospheric neutrino Monte Carlo and the dotted line represents the signal Monte Carlo.

8.3 Effective Area

Based on the selection criteria described in chapter 7 and the number of optical modules fired cut described above, it is possible to define an effective area for this analysis. The effective area is defined as

$$A_{eff} \equiv \left\langle \frac{N_{cuts}}{N_{gen}} A_{gen} \right\rangle \tag{8.1}$$

where N_{cuts} is the number of events remaining in the sample after selection criteria are applied, N_{gen} is the number of events generated in the sample, and A_{gen} is the generation area of the events. An effective area given in this fashion is useful for comparison of theoretical predictions.

8.4 Systematic Uncertainties

The systematic uncertainties associated with the AMANDA detector are quite large when compared to other high energy detectors. This is due in part to the fact that neutrino telescopes such as AMANDA use natural media, i.e. ice, as a detector medium. The optical properties of the ice used by AMANDA are difficult to measure precisely. The process of deploying the optical modules requires a melting-refreezing process that may drastically affect the properties of the ice. Once deployed, the OMs are inaccessible. Thus, reasons for strange behavior in any OM after deployment can only be deduced from signals received by the surface electronics. The theoretical uncertainties associated with neutrino-nucleon interactions are higher for AMANDA compared to those of accelerator experiments, due to the higher energy particles the AMANDA detector investigates.

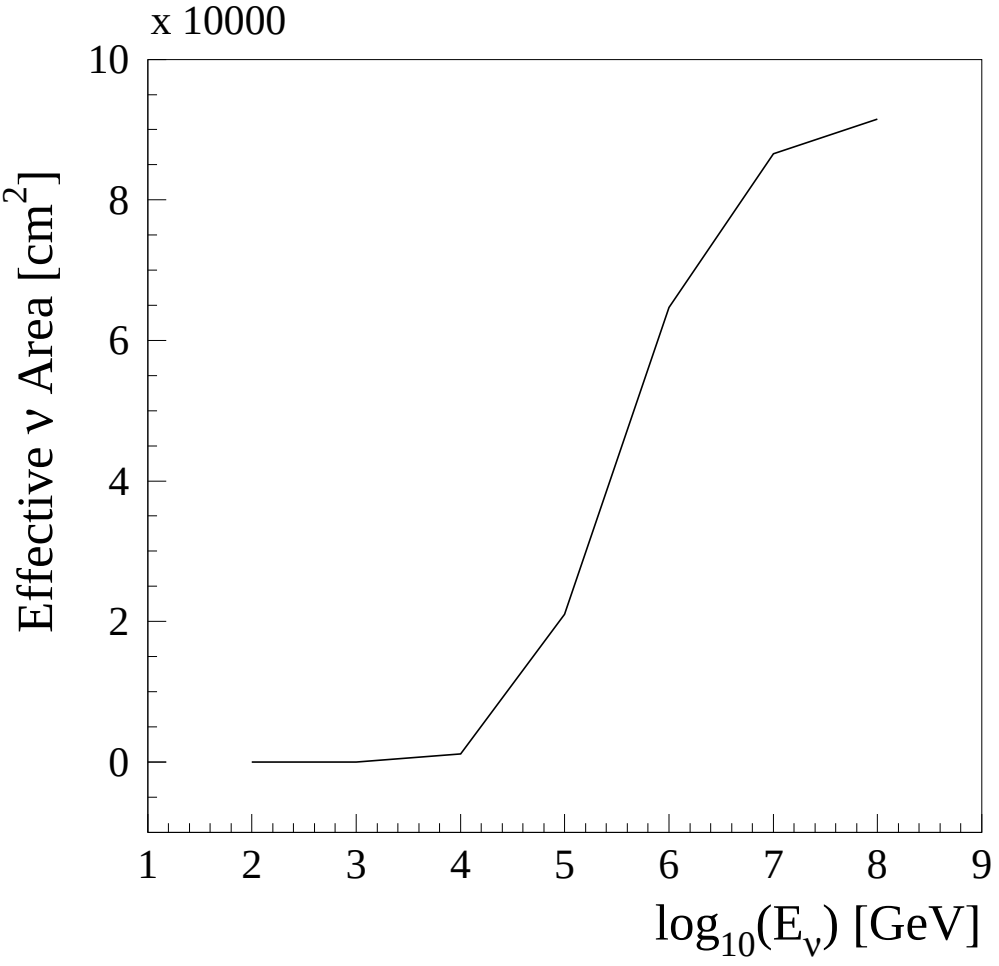

Figure 8.5: Effective area for the cuts used in this analysis.

The flux of atmospheric neutrinos is a convolution of the primary cosmic ray spectrum with the yield of the neutrinos produced by hadronic interactions of the cosmic rays in the atmosphere. Uncertainties in the primary cosmic ray spectrum and properties of relevant hadronic interactions affect the uncertainty of the atmospheric neutrino flux. This effect has been studied in [58] and is estimated to be approximately 30%.

The rate of energy loss in ice is not precisely known. The propagation code `MMC` used in the AMANDA-II simulations uses the formulas for cross sections which are valid within 1% [54, 55]. For the energy range from 20 GeV to 10^{11} GeV, the coefficients a and b from formula 3.9 have an average deviation from the linear formula between 3% and 5% [36].

Approximations are made by `PTD` in the implementation of the measurements of the optical properties of the ice. This can be seen by comparing analysis results using the KGM ice model, where direct measurements of the optical properties were used by `PTD`, to the results of the MAM ice model, which is an evolution of the KGM model. However, the MAM model corrects the error introduced by the approximations made by PTD by adjusting the absorption coefficient of the ice. The absorption coefficient in the MAM ice model was derived from fits to the data.

The optical properties of the ice melted during deployment and then re-freezed in the week following are difficult to measure. This quick refreezing process introduces many air bubbles in the ice nearest the optical modules. A camera

was deployed with one of the strings in the 1997-98 season. It indicated that there was very strong scattering near the optical modules. However, the issue could not be entirely settled as there was the possibility that the equipment simply failed. The lasers used for calibration purposes do not have a good line-of-sight through the bubbly ice to nearby modules. Thus, there are no direct measurements of the optical properties of hole ice.

Most of the uncertainties described above are absorbed by the normalization of the Monte Carlo simulations to the atmospheric neutrino flux. Thus, in the final analysis, only the atmospheric neutrino spectrum remains as the systematic uncertainty.

8.5 Results

As previously mentioned, this analysis was done using a blindness technique. As previously described, this technique required that 50% of the data be "blinded", meaning that this sample would not be touched until all cuts were refined. The remaining 50% would be used to develop cuts and the analysis technique. The final result would then be reported using only the blinded 50% sample.

The unblinded sample had a total of 222 neutrino candidates and a live-time of 98.4 days. Using the model rejection potential method described in 5.4, the number of optical modules fired cut was placed at 80. The predicted number of high energy signal neutrino events was 11.8 and the predicted atmospheric background was 3.3 above the cut. After applying the cut to the data, 6 events

remained in the sample. This yielded a limit of $7.0 \times 10^{-7}\,\mathrm{cm}^{-2}\,\mathrm{s}^{-1}\,\mathrm{sr}^{-1}\,\mathrm{GeV}$ without systematic uncertainties. Figure 8.6 shows the Monte Carlo distributions for atmospheric neutrinos and E^{-2} neutrinos along with the distribution in data for the number of optical modules fired parameter.

The blinded sample had a total of 178 neutrino candidates and a live-time of 98.6 days. The model rejection potential method yielded an optimal cut of the number of optical modules fired be greater than 80. Again, the predicted number of neutrino signal events was 11.8 and predicted number of background events was 3.3 above the cut. After applying the cut to the data, 4 events remained in the sample giving a limit of $4.5 \times 10^{-7}\,\mathrm{cm}^{-2}\,\mathrm{s}^{-1}\,\mathrm{sr}^{-1}\,\mathrm{GeV}$ without systematic uncertainties. Figure 8.7 shows the Monte Carlo distributions for atmospheric neutrinos and E^{-2} neutrinos along with the distribution in data for the number of optical modules fired parameter.

Although it does not follow a strict blinding procedure, combining the samples together and running the analysis yields interesting results. The combined sample has 197 days of live-time and contains 400 neutrino candidates. The optimal number of optical modules fired cut is 87 according to the model rejection potential method. Above this cut, there are 21.0 predicted signal high energy neutrino events and 4.5 predicted atmospheric background neutrino events. There were 9 events observed above the cut. This yields (without systematic uncertainties) a two sided confidence band with boundaries of $0.9 \times 10^{-7}\,\mathrm{cm}^{-2}\,\mathrm{s}^{-1}\,\mathrm{sr}^{-1}\,\mathrm{GeV}$ on the bottom side and $4.9 \times 10^{-7}\,\mathrm{cm}^{-2}\,\mathrm{s}^{-1}\,\mathrm{sr}^{-1}\,\mathrm{GeV}$ on the high side. Figure

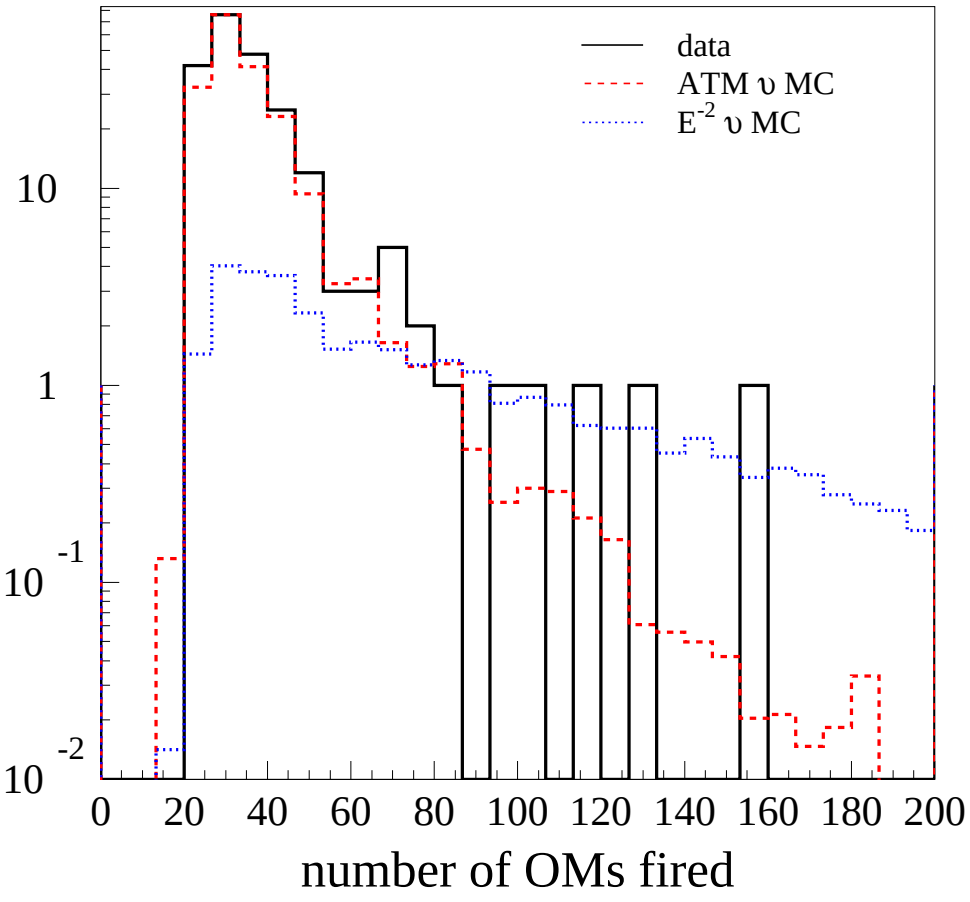

Figure 8.6: Number of channels fired for the unblinded data sample.

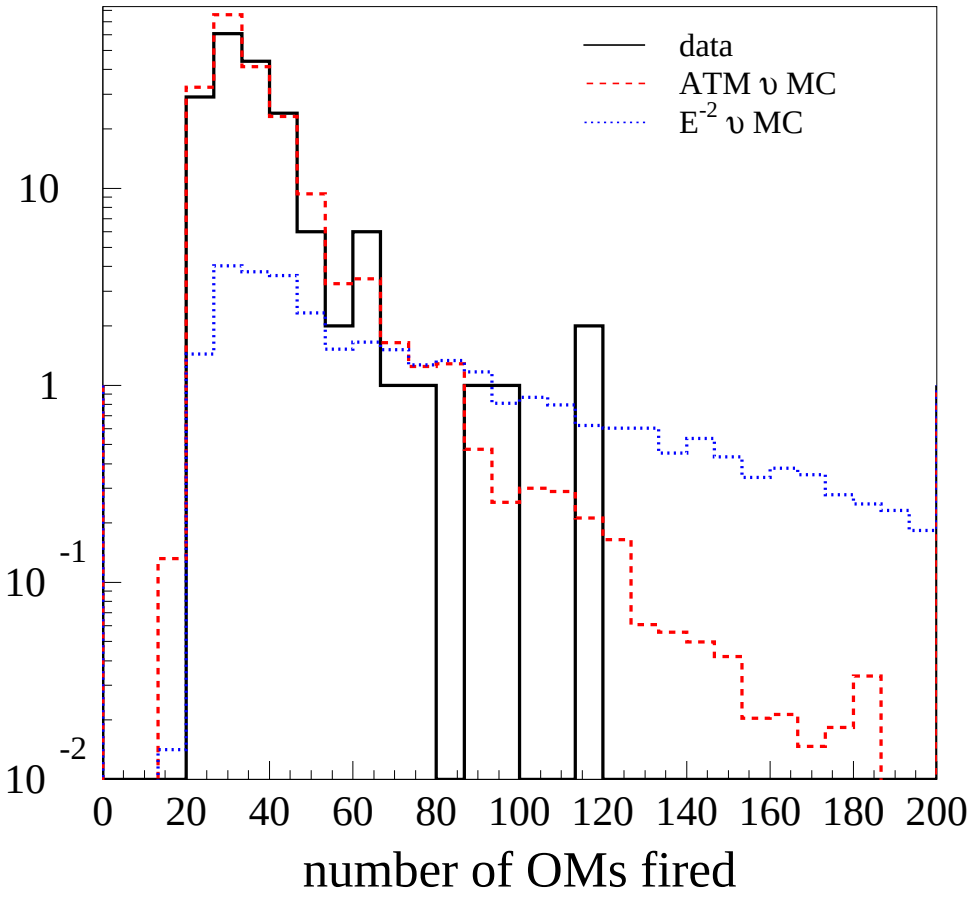

Figure 8.7: Number of channels fired for the blinded data sample.

8.8 shows the Monte Carlo distributions of atmospheric neutrinos and E^{-2} neutrinos along with the distribution in data for the number of optical modules fired parameter.

The Poisson error on the observed rate of atmospheric neutrinos is combined with the theoretical flux uncertainty to compute the correlations between background and efficiency for use in the probability distribution function used in the confidence interval construction. The theoretical flux uncertainty is taken about the best-fit flux $\hat{\Phi}$ and extended to $\pm 0.25 \times \Phi$. To incorporate these systematic uncertainties in the efficiencies into the limit calculations the prescription of Cousins and Highland [64], as implemented by Conrad *et al.* [65] with the unified Feldman-Cousins ordering and improved by a more appropriate choice of likelihood test [66] was used. Results from the three data samples are shown in 8.2.

Table 8.2: Results for the three different data samples.

Sample	Predicted Background	Predicted Signal	No. Obs. Events	Limit w/o Sys. $[\mathrm{cm}^{-2}\,\mathrm{s}^{-1}\,\mathrm{sr}^{-1}\,\mathrm{GeV}]$	Limit w/ Sys. $[\mathrm{cm}^{-2}\,\mathrm{s}^{-1}\,\mathrm{sr}^{-1}\,\mathrm{GeV}]$
unblinded	3.25	11.80	6	7.0×10^{-7}	7.2×10^{-7}
blinded	3.26	11.82	4	4.5×10^{-7}	4.8×10^{-7}
combined	4.47	21.04	9	$0.5 - 5.1 \times 10^{-7}$	$0.4 - 5.4 \times 10^{-7}$

8.6 Discussion of Results

The six remaining events in unblinded sample were scanned using the AMANDA event viewer. All six events appeared to be of high quality and consistent with a high energy muon track. Six events is an upward fluctuation from the predicted

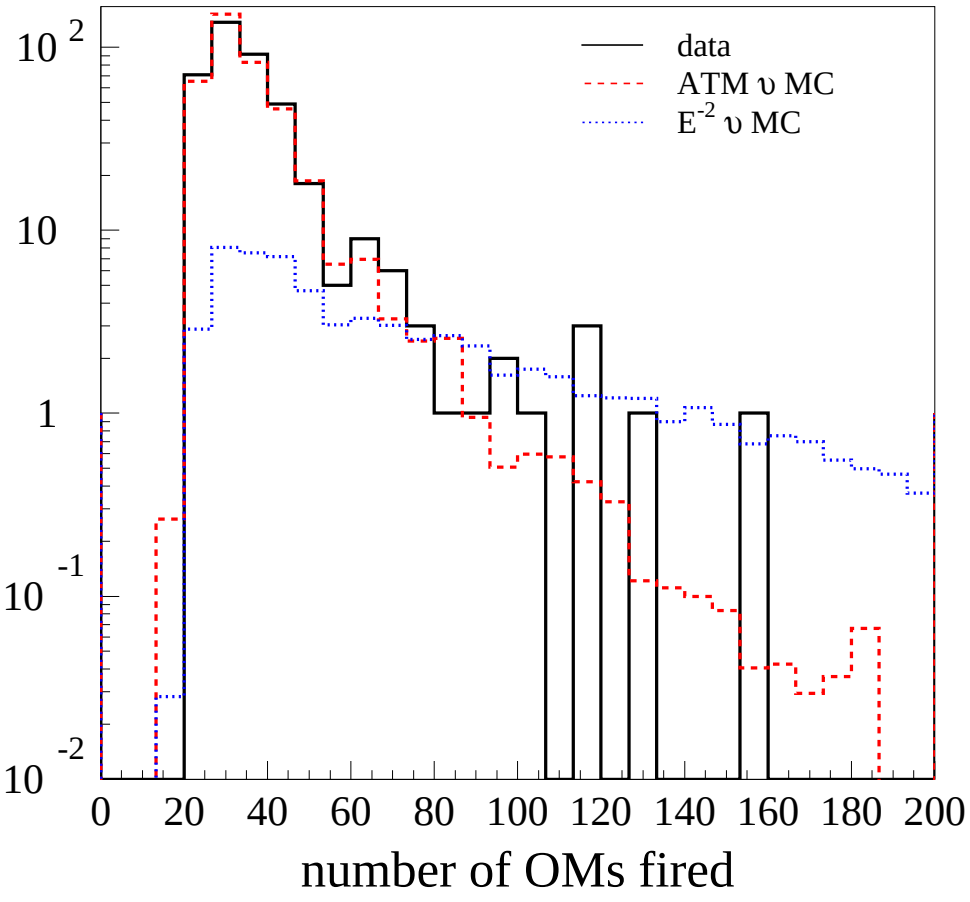

Figure 8.8: Number of channels fired for the combined data sample.

3.25 background events that gives an upward fluctuation in the final limit.

Scanning the four events that remained in the blinded analysis, which is the final result of this thesis, reveals one event that appears to be due to a coincident muon event, while the remaining three appear to be of good quality and consistent with a high energy muon track. This leads to the conclusion that either the extrapolation chosen in 8.1.2 is not valid, or we just happened to have an upward fluctuation of the background from nearly zero to one. To further test these hypotheses, more coincident muon background will need to be generated.

A positive outcome of these analyses is the fact that both the blinded and unblinded samples gave similar results, within statistical fluctuations. This suggests that the cuts chosen were good in the sense that they did not remove single, isolated background events, but whole classes of events.

Perhaps the most interesting of the results comes from the of the analysis that combined the blinded and unblinded data sets together. That analysis appears to give an excess of data events. At face value, it appears that a signal has been observed with a chance probablility of 3.7%. However, one must be very cautious of interpreting this result. Firstly, scanning the remaining nine events revealed one event that appeared to be caused by a coincident muon event entering the detector. Taking that event out of the equation leaves eight events on a background of 4.5, which leads to a chance probablity of 8.2%. At the 95% confidence level, this results in an upper limit of $5.1 \times 10^{-7}\,\mathrm{cm}^{-2}\,\mathrm{s}^{-1}\,\mathrm{sr}^{-1}\,\mathrm{GeV}$.

There are three possible explanations for this result. First, it could be

unsimulated background. Scanning the signal candidates revealed that one event appears to be from coincident muons. Futher studies could rule this out. Secondly, it could be a fluctuation in the data. Analysis of more data will reveal whether this is the case. The final possibility is that a signal has been observed.

In conclusion, although the results do not offer enough evidence to claim signal at this time, they do offer tantalizing hope that AMANDA-II may be close to a discovery.

8.7 Other Models

Four other models of high energy neutrinos were tested for this thesis. Two of these models SDSS [67, 68] and SSQC [23] are for core models of neutrino production in AGN. One model, SSBJ [23], makes a prediction for neutrino production in the jets of AGN. The final model, CharmD [69], is an optimistic model for production of charm neutrinos in the atmosphere. The sensitivities of these analyses are recorded in table 8.3 and the experimental results are recorded in table 8.4. Figure 8.9 compares Charm D and SDSS model predictions to the limits found in this analysis. Also shown in figure 8.9 is a comparsion of published AMANDA-B10 results to the results of this analysis.

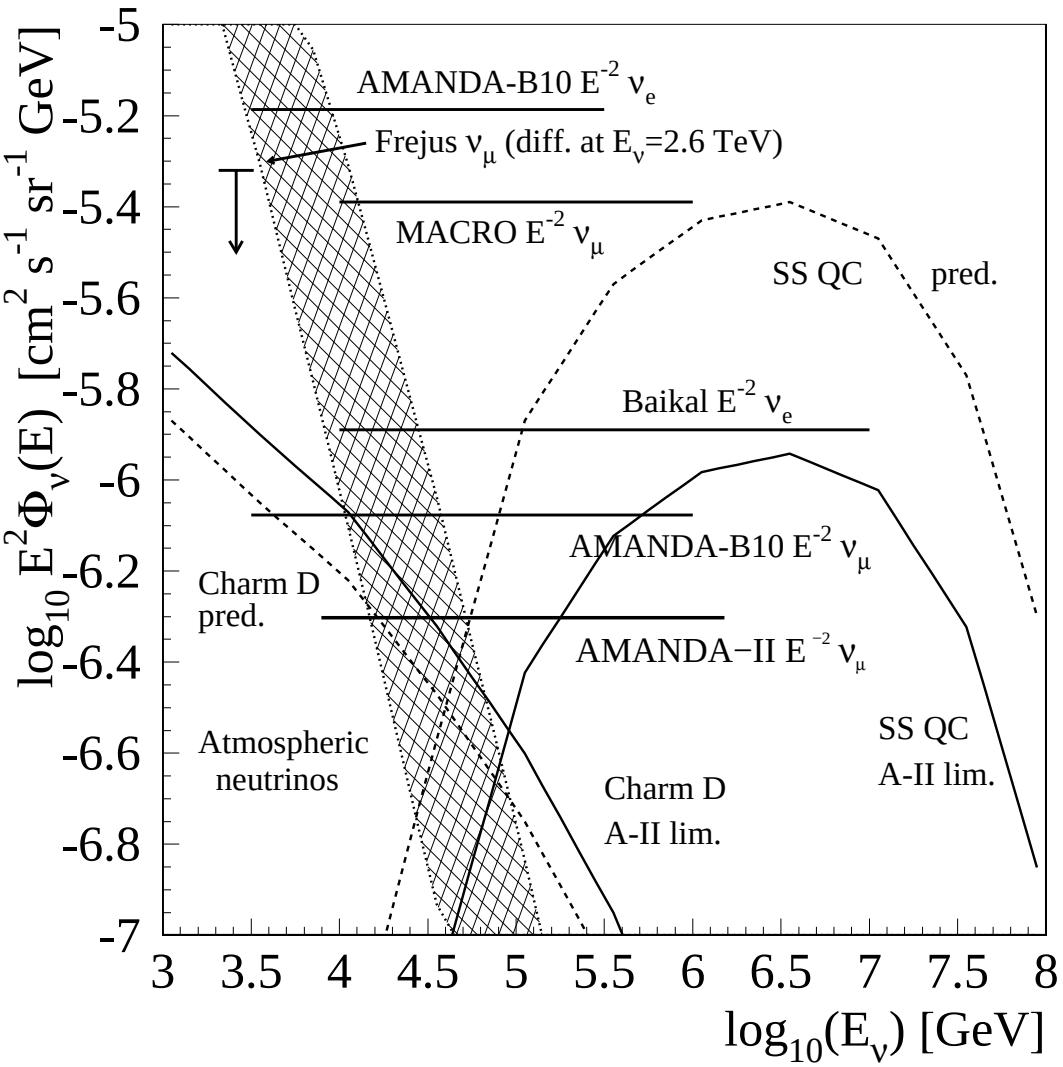

Figure 8.9: Comparison of predictions of Charm and the SDSS model of AGN to the results of this analysis. Also plotted are the AMANDA-B10 results and the AMANDA-II results (this work) for an assumed flat E^{-2} spectrum.

Table 8.3: Sensitivities for other models of high energy neutrinos. The optimal nchannel cut, predicted number of background events, and predicted number of signal events are shown. The average upper limit ($\bar{\mu}(n_b)$) and average model rejection factor are shown with and without the inclusion of systematic uncertainties.

Sample	nchannel cut	Predicted Background	Predicted Signal	$\bar{\mu}(n_b)$ w/o Sys.	$\bar{\mu}(n_b)$ w/ Sys.	MRF w/o Sys.	MRF w/ Sys.
SDSS	112	0.85	7.49	3.15	3.24	0.42	0.43
SSQC	101	1.30	17.0	3.49	3.57	0.21	0.21
SSBJ	80	3.25	9.87	4.51	4.69	0.46	0.47
Charm	50	16.2	4.85	8.19	8.85	1.69	1.82

Table 8.4: Experimental results for other models of high energy neutrinos. The number observed, the predicted number of background events, and the predicted number of signal events are shown. The experimental limits (event limit $\mu_o \equiv \mu(n_o, n_b)$) are given with and without the inclusion of systematic uncertainties.

Sample	Number Observed	Predicted Background	Predicted Signal	$\mu(n_o)$ w/o Sys.	$\mu(n_o)$ w/ Sys.	MRF w/o Sys.	MRF w/ Sys.
SDSS	2	0.85	7.49	5.06	5.28	0.68	0.70
SSQC	2	1.30	17.0	4.61	4.68	0.27	0.28
SSBJ	4	3.25	0.87	5.34	5.66	6.14	6.50
Charm	15	16.2	4.85	6.41	6.82	1.32	1.41

Chapter 9

Conclusions

A search for neutrinos from diffuse astronomical sources has been performed with the AMANDA-II neutrino detector using the data taken in year 2000. After reducing the background of $\sim 10^9$ down-going cosmic ray induced muons, 4 events remain in the sample. Monte Carlo simulations predict 3.25 atmospheric neutrino (background) events and 11.82 high energy E^{-2} neutrino (signal) events for 98.6 days of live-time of the AMANDA-II detector. This yields a limit, including systematic uncertainties, at the 90% confidence level of

$$\Phi_{90\%} \leq 4.8 \times 10^{-7}\,\mathrm{cm}^{-2}\,\mathrm{s}^{-1}\,\mathrm{sr}^{-1}\,\mathrm{GeV}. \tag{9.1}$$

This is a considerable improvement over the current published result based on the 1997 diffuse flux analysis which included 130 days of AMANDA-B10 detector live-time and produced a result of $\Phi_{90\%} \leq 8.4 \times 10^{-7}\,\mathrm{cm}^{-2}\,\mathrm{s}^{-1}\,\mathrm{sr}^{-1}\,\mathrm{GeV}$.

This thesis has also investigated the uncertainty introduced by simulation of the atmospheric neutrino flux by studying three different atmospheric neutrino models (Lipari, Bartol and Honda). The result of this analysis shows virtually no

difference in the energy parameter, number of optical modules fired, used by this diffuse flux analysis.

With a further investigation of coincident muons in the detector, this analysis can be easily extended using the 2001 and 2002 AMANDA-II data.

Looking toward the future, the construction of the IceCube detector is scheduled to begin in 2004 and end in 2010. IceCube will be a considerable upgrade from the AMANDA-II detector as it will instrument $1\,\mathrm{km}^3$ of ice and contain $\sim$ 4000 optical modules on 81 strings. After three years of operation, IceCube will be sensitive to a diffuse flux limit of $\Phi_{90\%} \leq 4.2 \times 10^{-9}\,\mathrm{cm}^{-2}\,\mathrm{s}^{-1}\,\mathrm{sr}^{-1}\,\mathrm{GeV}$ [70]. Figure 9.1 compares the limit found in this work with the IceCube sensitivity after 3 years of operation.

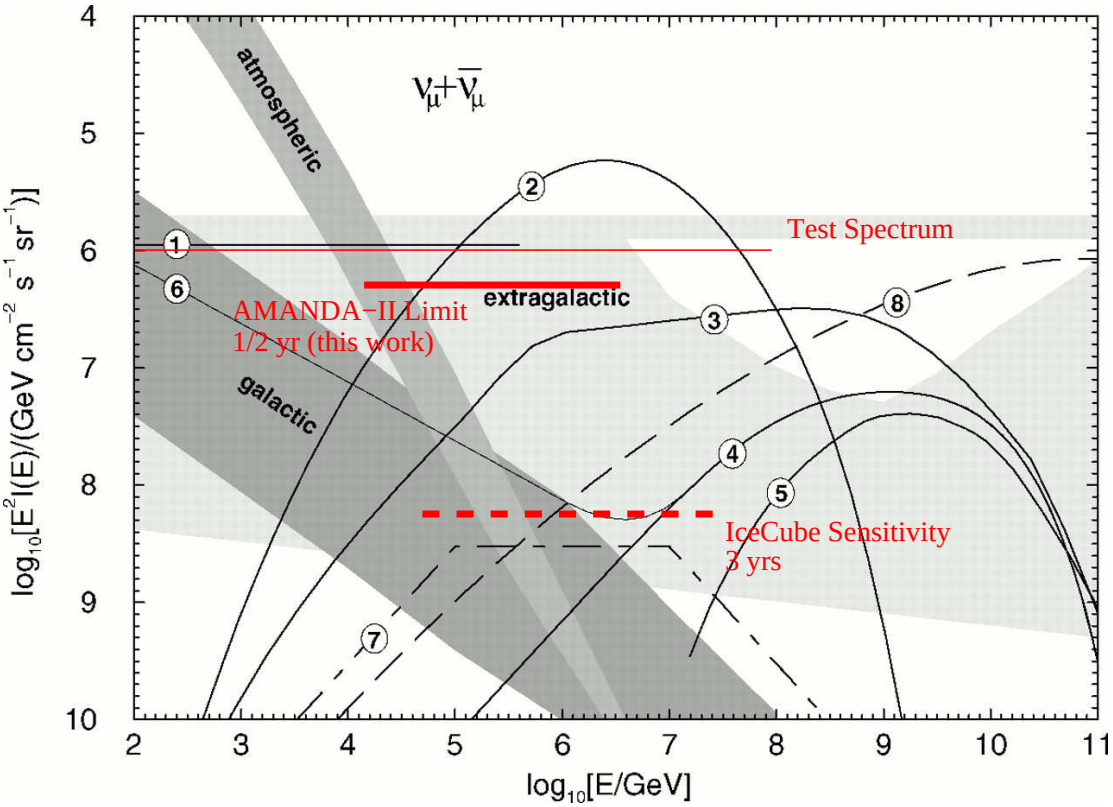

Figure 9.1: Comparison of IceCube sensitivity after 3 years of operation to the limit set with this work.

Bibliography

[1] R. Svensson and A. A. Zdziarski. *Astrophys. J.* 349, (1990), 415-28.

[2] F. Reines. *Ann. Rev. Nucl. Science*, 10, (1960), 1.

[3] K. Greisen. *Ann. Rev. Nucl. Science*, 10, (1960), 63.

[4] M. A. Markov and I. M. Zheleznykh. *Nucl. Phys.*, 27, (1961), 385.

[5] J. Babson et al. (the DUMAND Collaboration). *Phys. Rev. D*, 42, (1990), 3613-20.

[6] E. Andres et al. (the AMANDA Collaboration). *Nature*, 410, (2001), 441-443.

[7] J. Aherns et al. (the AMANDA Collaboration). *Astrophys. J.*, 583, (2003), 1040.

[8] J. Aherns et al. (the AMANDA Collaboration). *Phys. Rev. Lett.*, 90, (2003), 251101.

[9] J. Aherns et al. (the AMANDA Collaboration). *Phys. Rev. D*, 67, (2003),012003.

[10] J. Aherns et al. (the AMANDA Collaboration). *Phys. Rev. D*, 66, (2002), 032006.

[11] J. Aherns et al. (the AMANDA Collaboration). *Astropart. Phys.*, 16, (2002), 345.

[12] http://astroparticle.uchicago.edu/announc.htm

[13] E. Fermi. *Phys. Rev.*, 75 (1949) 1169-1174.

[14] E. Fermi. *Astrophys. J.*, 119 (1954) 1-6.

[15] T. Gaisser. *Cosmic Rays and Particle Physics*, Cambridge University Press, 1990.

[16] F. Halzen. Private communication.

[17] F. Halzen. *Neutrinos in Physics and Astrophysics* (*Proc. Theor. Advanded Staudy Inst. at Boulder*), P. Langacker, ed. (World Scientific, Singapore, 1998) pp. 524-69.

[18] G. Sigl *Towards the Millenium in Astrophys., Problems and Prospects. Int. School of Cosmic Ray Astrophys. 10th Course, Erice, Italy, June 16-23, 1996*, ed. M.M. Shapiro, R. Silberberg, J.P. Wefel, p31. Singapore: World Sci. (1998)

[19] M. Birkel and S. Sarkar. Extremely High Energy Cosmic Rays from Relic Particle Decays. hep-ph/9804285, June 1998.

[20] P. Sreekumar, et al. (EGRET Collaboration). *Ap. J.*, 494 (1998) 523-534.

[21] J. Learned and K. Mannheim. *Annu. Rev. Nucl. Part. Sci* 50 (2000) 679-749.

[22] L. Nellen, K. Mannheim, and P. Biermann. *Phys. Rev. D* 47 (1993) 5270-5274.

[23] F. Stecker and M. Salamon. *Space Sci. Rev* 74:341 (1996).

[24] K. Mannheim, R. Protheroe, and J. Rachen. On the Cosmic Ray Bound for Models of Extragalactic Neutrino Productrion. astro-ph/9812398, July 2000.

[25] K. Mannheim. *Astroparticle Phys.* 3 (1995) 295-302.

[26] R. Protheroe and P. Johnson. *Astroparticle Phys.* 4 (1996) 253-269.

[27] J. Rachen and P. Biermann. *Astron. Astrophys.* 272 (1993) 161-175.

[28] E. Waxman and J. Bachall. *Phys. Rev. Let.* 78 (1997) 2292-2295.

[29] S. Fukuda, et al. (Super-Kamiokande Collaboration). *Phys. Rev. Let.*, 85 (2000) 3999-4003.

[30] Q. Ahmad et al. (SNO Collaboration). *Phys. Rev. Let.*, 87 (2001) 071301

[31] C. Athanassopoulos et al. (LSND Collaboration). nucl-ex/9709006, September 2003.

[32] V. Barger, S. Pakvassa, T. Weiler, and K. Whisnant. *Phys. Let. B* 437 (1998) 107-116.

[33] R. Gandhi, C. Quigg, M. H. reno, and I. Sacevic. *Astroparticle Phys.* 5 (1996) 81-110.

[34] D. E. Groom et al. *European Phys. J.*, C15 (2000) 1. (The Particle Data Book.) http://pdg.lbl.gov

[35] C. H. V. Wiebush. *The detection of Faint Light in Deep Underwater Neutrino Telescopes*. Ph.D. thesis, Physikalisches Institut, Technishe Hochschule, Aachen (1995).

[36] T. R. DeYoung. *Observation of Atmospheric Muon Neutrinos with AMANDA*. Ph.D. thesis, University of Wisconsin-Madison, (2001).

[37] K. Woschnagg et al. (AMANDA Collaboration). In *Proc. 26th Int. Cosmic Ray Conf.*, D. Kieda, M. Salamon, and B. Dingus, eds. (August 1999) HE.4.1.15. http://krusty.physics.utah.edu/ icrc/proceedings.html

[38] http://amanda.berkeley.edu/kurt/ice2000/plots/

[39] P. Desiati, personal communication.

[40] P. Steffen. *Direct-Walk: A Fast Track Search Algorithm Without Hit Cleaning*, Int. Rep. 20010801

[41] P. Steffen. *Direct-Walk II*, Int. Rep. 20020201

[42] J. Ahrens et al. (AMANDA Collaboration). Submitted to *NIM*, (August 2003).

[43] A. Karle. In *Proc. Zeuthen Workshop on Simulation and Analysis Methods for Large Neutrino Telescopes*, C. Spiering, ed. (July 1998) pp. 174-185.

[44] W. H. Press, S. A. Teukolsky, W. V. Vetterling, B. P. Flannery, *Numerical Recipies in C - The Art of Scientific Computing*, 2nd Edition, Cambridge University Press, 1997.

[45] T. R. DeYoung et al. (AMANDA Collaboration). In *Durham 2002: Advanced Statistical Techniques in Particle Physics*, pp. 235-241

[46] G. Feldman and R. Cousins, A Unified Approach to the Classical Statistical Analysis of Small Signals, physics/9711021 (December 1999).

[47] G. C. Hill and K. Rawlins. Unbiased Cut Selection for Optimal Upper Limits in Neutrino Detectors: The Model Rejection Potential Technique, astro-ph/02 09350 (September 2002).

[48] I. J. Taboada. *Search for High Energy Neutrino Induced Cascades with the AMANDA-B10 Detector*, Ph. D. thesis, University of Pennsylvania, (2002).

[49] http://www.fis.usb.ve/ itaboada/private/amanda/xtalk/xtalk.html

[50] S. Boser. *Separation of Atmospheric Neutrinos with the AMANDA-II Detector*, Diploma thesis, Technische Universitat Munchen, (2002).

[51] D. Heck. *CORSIKA: A Monte Carlo Code to Simulate Air Showers*, Tech. Rep. FZKA 6019, Forshungszebtrum Karlsruhe (1998).

[52] G. Hill. *Experimental and Theoretical Aspects of High Energy Neutrino Astrophysics*, Ph. D. thesis, University of Adelaide, Adelaide, Australia (1996).

[53] W. Lohmann, R. Kopp, and R. Voss. *Energy Loss of Muons in the Range 1-10000 GeV*, Yellow Report 85-03, CERN (1985).

[54] D. Chirkin and W. Rodhe. In *Proc. 27th Int. Cosmic Ray Conf.* eds. K.H. Kampert, G. Hainzelmann, and C. Spiering, (2001), pp.1017-1020.

[55] http://amanda.berkeley.edu/ dima/stuff

[56] S. Hundertmark. In *Proc. of 1st Workshop Methodical Aspects of Underwater/Ice Neutrino Telescopes*, Zeuthen Germany, (1998) pp. 276-286.

[57] S. Hundertmark. *Verticle Ice Properties for AMANDA Simulation*, AMANDA Internal Rep. 20001001, (2000).

[58] T. K. Gaisser. *Uncertainty in Flux of Atmospheric Neutrinos: Implications for Upward Muons in AMANDA B10*, AMANDA Internal Rep. 20001201, (2000).

[59] P. Lipari. *Astroparticle Phys.*, 1, (1993), 195-227.

[60] M. Honda, T. Kajita, K. Kasahara, S. Midorikawa. *Phys. Rev. D*, 52, (1995), 4985-5005.

[61] V. Agrawal, T. K. Gaiser, P. Lipari, and T. Stanev. *Phys. Rev. D*, 53, (1996), 1314-1323.

[62] T. K. Gaisser, R. J. Protheroe, and T. Stanev. In *Proc. of the 18th International Cosmic Ray Conference*, ed. N. Durgaprasad et al. (Tata Institute of Fundamental Research, Colaba, Bombay), Vol. 5, (1983), pp. 174

[63] T. K. Gaisser. Personal communication.

[64] R. D. Cousins and V. L. Highland. *Nucl. Ins. Meth. Phys. Res.*, A320, (1992), 331.

[65] J. Conrad, O. Botner, A. Hallgren, and C. Perez de los Heros. *Phys. Rev. D.*, 67 (2003) 012002.

[66] G. C. Hill, *Phys. Rev. D*, 67, (2003), 118101.

[67] F. W. Stecker, C. Done, M. H. Salamon, and P. Sommers. *Phys. Rev. Lett.*, 66, (1991), 2697-2700

[68] F. W. Stecker, C. Done, M. H. Salamon, and P. Sommers. *Phys. Rev. Lett.*, 69, (1992), 2738.

[69] E. Zas, F. Halzen, and R. A. Vazquez. *Astropart. Phys.*, 1, (1993), 297.

[70] J. Aherns et al. (the IceCube Collaboration). Accepted to *Astropart. Phys.*, (September 2003). astro-ph/0305196.

Appendix A

Reconstruction Chain

Table A.1: Outline of reconstruction chain.

Level 1		
reco 1	direct walk	
reco 2	maximum likelihood	16 iterations
cut 1	$\Theta_{reco2} > 70°$	
Level 2		
cut 2	$\Theta_{reco2} > 80°$	
reco 3	multi-photoelectron	16 iterations
reco 4	Bayesian likelihood	16 iterations
reco 5	line fit	
reco 6	dipole moment	
reco 7	tensor of inertia	amplitude weight = 1
reco 8	cascade likelihood	
Level 3		
xt-filter		
reco 9	maximum likelihood	16 iteration
reco 10	Bayesian likelihood	16 iteration
Level 4		
cut 4	$(\Theta_{reco9} - \Theta_{reco10}) < 18(ndirc_{reco9} - ndirc_{reco10})$	
Level 5		
cuts 5-11	quality cuts level 5.5	
reco 11	maximum likelihood	64 iterations
reco 12	Bayesian likelihood	64 iterations

Appendix B

Quality Levels

Table B.1: List of cuts defining each quality level. The two dimensional cuts in the two rows are defined by their slope and intercept.

Quality Level	$L_{dir}^{[-15:25]}$	$-\mathcal{L}_{u/d}$	$\lvert S_{P_{hit}} \rvert$	$N_{dir}^{[-15:75]}$	$L_{dir}^{[-15:75]} < m * -\mathcal{L}_{t/s} - b$ (m,b)	$-\mathcal{L}_{t/s} > m * cogz - b$ and cogz < 150 (m,b)
1	100.0	30	0.400	5	(4.3,-25)	(-0.22,-5.5)
2	110.0	31	0.370	6	(4.3,-35)	(-0.44,-11.0)
3	120.0	32	0.350	7	(4.3,-45)	(-0.67,-16.75)
4	130.0	34	0.330	8	(4.3,-55)	(-0.89,-22.5)
5	155.0	35	0.275	10	(4.3,-65)	(-1.1,-27.5)
6	170.0	37	0.250	12	(4.3,-70)	(-1.32,-33.0)
7	200.0	40	0.200	15	(4.3,-75)	(-1.54,-38.5)
8	210.0	42	0.180	17	(4.3,-85)	(-1.77,-44.25)

Appendix C

Atmospheric Neutrino Event Candidates

Table C.1: List of atmospheric neutrino events.

Event No.	Day	Zenith	Azimuth	Right Asc.	Declin.	Gal. Long.	Gal. Lat.
2142814	160	123.301	320.828	15.2945	33.301	53.0652	57.9794
3185887	182	157.48	313.104	1.99119	67.481	129.394	5.46677
3593604	226	171.038	355.539	20.9636	81.038	114.693	22.1963
423496	269	121.552	118.105	1.29468	31.552	129.453	-30.9872
481414	84	126.515	75.4717	23.666	36.516	107.249	-24.1695
1332216	157	160.908	100.636	12.8708	70.907	122.836	46.2211
1760779	188	162.309	259.04	18.1623	72.308	102.969	28.905
1567697	300	128.435	170.983	4.7038	38.435	164.594	-5.1114
2078330	150	148.356	349.003	13.8531	58.357	108.528	57.0691
938626	151	157.079	41.7212	5.49294	67.079	145.411	17.3849
866	154	168.069	226.651	7.74847	78.069	136.26	29.2533
2412706	159	138.845	176.048	0.654423	48.844	120.869	-13.979
672095	164	143.794	212.819	11.9026	53.795	140.655	61.318
3914785	164	141.591	227.981	0.323957	51.592	117.879	-10.9655
938476	177	129.698	334.05	14.2338	39.697	74.445	68.7569
3432923	179	152.855	165.484	12.7188	62.854	124.554	54.2481
1957663	187	171.513	258.842	18.6472	81.513	113.389	27.2718
4974272	201	132.437	52.7352	20.918	42.436	83.6236	-1.70357
3282703	207	165.333	110.991	6.85558	75.332	139.32	26.1691
2135873	216	163.605	300.849	20.3077	73.605	106.718	20.141
955188	218	132.478	332.528	12.8398	42.479	123.662	74.6478
3336654	218	153.976	45.6379	18.925	63.975	94.2921	23.7548
3790473	218	156.349	197.532	10.8865	66.35	139.717	46.738

continued on next page

Table C.1: *continued*

Event No.	Day	Zenith	Azimuth	Right Asc.	Declin.	Gal. Long.	Gal. Lat.
2089774	222	149.334	342.856	15.2368	59.334	95.6363	49.5412
3055268	222	130.835	157.585	7.97706	40.835	179.276	29.521
5392785	62	122.563	90.9242	14.7564	32.563	52.2915	64.7812
4953315	236	158.247	34.3877	21.1709	68.246	104.66	13.6336
1697	236	148.436	62.0133	22.1297	58.437	102.87	2.09094
4683242	241	155.039	33.0419	22.0432	65.039	106.304	7.77119
831360	259	128.149	74.2357	15.0015	38.15	63.3937	60.9445
2200836	264	136.095	31.8114	14.9069	46.096	79.1172	59.2005
28561	272	173.878	345.289	8.47128	83.879	129.347	29.4919
3002342	272	150.309	147.378	11.3483	60.309	141.586	53.4168
4839112	273	143.019	41.6718	3.20105	53.02	143.255	-4.21166
2700849	285	134.222	5.96017	20.1339	44.223	80.0084	6.24693
3520175	67	127.734	50.6807	11.27	37.734	179.007	67.3704
215224	292	154.451	190.286	20.9048	64.452	100.618	12.4372
5331635	69	138.732	290.263	1.73171	48.731	131.777	-13.2376
1896065	302	154.624	355.666	19.2475	64.623	95.5759	21.9064
3277996	307	148.84	76.7077	3.83664	58.84	144.316	3.60131
3948769	69	158.846	144.439	6.65749	68.845	146.188	24.1082
898909	72	144.404	62.0627	0.976479	54.405	123.984	-8.45215
1229568	77	169.206	107.723	23.8249	79.207	119.94	16.6968
2851464	78	125.122	30.2293	11.0935	35.123	186.88	66.0701
2377102	88	174.298	312.258	15.2546	84.297	119.	31.6893
4567259	89	146.837	292.785	0.916248	56.836	123.418	-6.03241
715221	90	128.641	331.188	7.77793	38.64	181.109	26.7859
4717507	99	176.852	18.3145	14.1549	86.852	121.72	30.0911
597394	104	143.799	6.95995	23.6347	53.8	112.128	-7.52582
2495921	106	154.377	304.518	10.6756	64.377	143.098	47.3006
2928444	106	163.767	13.0684	7.71865	73.767	141.188	29.5665
3374821	106	144.659	79.0094	5.00195	54.659	153.998	7.56312
471928	108	141.284	78.1579	11.3117	51.284	152.6	60.1678
488352	114	150.548	234.38	4.59569	60.549	147.315	8.79178
224809	121	136.436	261.797	2.43239	46.437	139.425	-13.3861
5726476	53	156.085	15.6118	21.5908	66.084	104.81	10.3767
4384033	136	120.157	184.128	8.67769	30.157	193.819	35.5975
4819501	137	123.046	144.115	13.1171	33.047	94.2192	83.1897
5929236	137	142.154	180.975	15.1854	52.153	86.3581	53.8816
1329751	138	146.12	319.734	11.4465	56.121	144.783	57.2696
5281309	139	139.485	221.383	10.2231	49.485	165.624	52.439

continued on next page

Table C.1: *continued*

Event No.	Day	Zenith	Azimuth	Right Asc.	Declin.	Gal. Long.	Gal. Lat.
698547	139	129.877	134.497	21.3088	39.878	84.6945	-6.69083
441286	140	135.683	91.4076	23.2315	45.683	105.646	-13.8893
5303086	144	170.711	90.5342	18.2611	80.712	112.511	28.1859
1326220	147	156.324	253.651	16.5058	66.324	98.1264	38.6074
1355187	147	169.176	279.881	14.8774	79.175	116.178	36.312
2165291	148	168.978	188.852	0.624797	78.977	122.238	16.1241
2159840	150	155.558	334.368	15.179	65.557	103.103	45.8421
5046057	151	156.956	163.441	14.9526	66.957	105.91	45.795
1259101	152	148.04	239.72	17.6913	58.039	86.4415	31.9002
4121944	154	144.777	43.8361	19.7658	54.777	87.5412	14.57
4724656	56	150.867	134.574	10.1481	60.866	150.438	46.6437
4382518	156	164.71	125.773	14.4205	74.709	114.947	40.9323
4132334	158	128.583	4.93843	7.56419	38.583	180.434	24.3551
1451412	158	161.949	152.949	9.931	71.949	139.031	39.2177
1654509	165	163.482	164.479	19.2804	73.481	104.89	24.1542
2116222	165	145.461	236.572	16.4147	55.46	84.7647	42.5894
3681545	165	126.586	65.6443	10.359	36.586	186.78	57.0264
3910453	170	158.705	48.9174	0.123911	68.705	118.935	6.17543
2842511	171	163.534	244.9	6.68018	73.534	141.166	25.188
4576434	177	144.577	258.661	10.7645	54.577	154.075	54.2833
5194469	178	130.772	281.183	12.4235	40.771	142.754	75.3397
2419051	179	151.518	44.3909	16.3034	61.517	92.9051	41.5974
3521648	179	127.045	271.042	6.07552	37.044	174.953	7.48809
2049092	180	176.657	97.4777	11.1914	86.658	124.564	30.1479
475650	182	169.497	12.0137	10.0743	79.497	131.422	34.7077
1796076	183	121.582	225.448	2.00246	31.581	139.658	-29.0493
4895669	185	129.333	13.9474	6.22779	39.332	173.747	10.141
1021126	188	156.129	58.1021	5.53369	66.128	146.405	17.1366
1580120	188	120.343	203.431	21.376	30.343	78.2904	-13.8983
5955415	188	165.616	20.5008	21.5408	75.616	111.473	17.3874
573627	190	143.264	227.942	18.2724	53.265	81.5809	26.5271
5276912	200	142.607	287.681	6.88337	52.608	163.664	21.4671
2137011	202	173.463	328.557	18.956	83.464	115.61	26.7695
967389	203	146.052	234.65	19.9791	56.053	89.5763	13.5559
2658001	59	160.213	254.579	17.7397	70.214	100.699	31.0613
2491556	213	137.589	198.883	4.36925	47.59	155.381	-1.56085
1283256	60	131.393	121.708	21.6951	41.392	88.9558	-8.63567
3368601	60	132.827	260.446	20.0593	42.826	78.3839	6.19648

continued on next page

Table C.1: *continued*

Event No.	Day	Zenith	Azimuth	Right Asc.	Declin.	Gal. Long.	Gal. Lat.
332303	224	146.28	212.38	16.0317	56.281	87.1848	45.4234
4844368	226	144.917	77.1417	21.0874	54.916	94.1441	5.22988
332712	234	142.157	16.8533	6.7287	52.158	163.656	19.9813
3373864	234	164.451	188.451	8.8699	74.451	139.162	34.0048
3533809	239	122.233	1.66995	18.687	32.232	61.3614	16.0666
1331839	62	150.488	13.1948	5.32518	60.488	150.675	13.041
2762494	242	130.105	176.537	3.63934	40.104	154.347	-12.3735
1501705	245	142.478	192.181	21.1552	52.479	92.7413	3.14568
1608536	249	122.409	152.723	0.621733	32.408	119.474	-30.3688
2843674	249	136.579	162.221	5.88369	46.579	165.449	10.1921
389600	250	153.437	279.557	10.4432	63.438	145.631	46.799
3014760	250	139.583	30.6523	15.5662	49.584	79.9625	51.7251
3349658	63	138.652	98.9554	7.29776	48.651	168.945	24.2021
4106905	254	131.003	23.7858	21.395	41.003	86.1963	-6.60053
1505225	255	153.091	155.948	0.227849	63.092	118.674	0.532882
1545291	256	130.297	204.843	21.2403	40.296	84.4509	-5.83414
3300293	259	124.642	135.963	22.4683	34.641	92.1952	-19.5373
486914	262	155.036	183.321	20.7263	65.037	100.386	13.7004
2922333	262	165.608	262.665	2.83529	75.608	130.231	14.4459
730347	263	142.868	128.872	1.61213	52.869	129.831	-9.39499
2845681	263	131.118	320.542	22.7049	41.117	98.2515	-15.4844
2957667	263	157.184	175.965	8.86973	67.184	147.552	36.4295
1172768	264	140.891	210.276	22.2424	50.892	99.342	-4.65065
4140788	265	123.744	209.957	12.4412	33.745	160.515	81.4751
2032341	269	152.954	92.715	10.5472	62.953	145.501	47.6486
3415232	269	120.08	359.039	23.2524	30.08	99.2908	-28.3338
1035338	65	154.838	310.995	8.51513	64.839	150.98	34.8786
2880198	276	146.659	66.9023	16.5711	56.66	85.9205	41.0362
3290529	276	146.046	160.172	12.2568	56.045	133.118	60.3651
2469576	277	149.12	217.346	4.60807	59.12	148.457	7.91186
3638945	277	163.501	115.012	16.8253	73.502	105.671	34.4309
2395528	278	165.341	113.902	10.9153	75.34	132.137	39.6347
2828443	279	135.854	153.399	10.3956	45.854	170.334	55.3592
745094	280	156.428	118.967	3.40547	66.429	137.399	7.95208
3618665	280	166.802	4.0705	0.410794	76.802	121.359	14.0121
2783371	66	132.613	272.037	17.8482	42.612	68.8669	28.6687
122072	282	170.758	18.4628	7.336	80.758	133.319	27.9001
1535236	285	133.78	34.7887	12.8876	43.781	121.788	73.3432

continued on next page

Table C.1: *continued*

Event No.	Day	Zenith	Azimuth	Right Asc.	Declin.	Gal. Long.	Gal. Lat.
3407046	285	150.139	255.815	6.69194	60.139	155.404	22.1027
3686412	285	146.604	238.912	9.09088	56.604	160.14	40.6245
5212833	288	158.925	188.753	19.0549	68.925	99.7584	24.1381
1630711	294	122.09	35.9698	13.6043	32.09	62.6181	79.0758
2756856	295	163.899	233.49	5.4356	73.9	138.929	20.3861
1546608	296	122.909	77.7734	10.5021	32.908	193.507	59.0175
1320443	297	164.498	203.14	1.21961	74.499	124.413	11.6898
5032179	300	127.737	189.698	18.8912	37.738	67.649	15.8337
2401616	301	136.381	277.629	1.31719	46.38	127.882	-16.2263
1553304	305	137.521	188.737	13.261	47.521	111.434	69.0629
2783736	71	159.939	225.74	20.8142	69.939	104.794	16.1807
5949917	75	128.221	44.9787	21.0613	38.22	81.501	-5.70026
3569875	79	130.102	202.569	2.01478	40.103	137.07	-20.8545
2308452	82	144.615	164.583	0.842262	54.616	122.8	-8.25552
5509929	85	146.403	253.014	7.42531	56.403	160.794	26.9219
5850961	85	122.263	47.632	22.4788	32.263	90.9006	-21.5874
2863674	91	180.	333.446	16.0122	90.	122.932	27.1283
3994675	50	147.359	211.138	2.45243	57.36	135.587	-3.14128
4436099	50	138.402	74.9444	13.1403	48.402	115.234	68.4716
1782730	96	140.309	229.382	12.4651	50.309	132.337	66.3873
2839606	96	143.223	58.7723	3.82969	53.224	147.786	-0.816065
5736570	97	149.732	151.515	8.88832	59.732	156.604	38.4087
2897298	102	146.631	197.718	19.4076	56.631	87.9974	18.0911
3871583	51	133.214	272.339	23.1064	43.214	103.366	-15.631
1208393	111	137.175	20.748	21.6788	47.176	92.6722	-4.18003
545025	115	143.808	113.705	12.83	53.808	123.47	63.3185
1747483	116	167.387	201.448	12.0469	77.387	126.344	39.4173
4294055	117	152.1	43.968	9.2771	62.099	152.669	40.505
4438509	120	170.291	325.107	15.1039	80.29	116.368	35.053
6014534	121	133.209	32.3442	16.5537	43.208	67.9635	42.8522
1349324	122	158.705	359.934	0.387539	68.705	120.365	5.97387
4929757	123	125.609	60.3763	10.7296	35.608	187.596	61.6041
1654462	125	143.525	336.005	8.77144	53.524	164.621	38.3773
2341138	52	132.901	254.129	16.7311	42.901	67.5518	40.9082
2310094	127	123.167	1.08217	10.2397	33.167	193.071	55.7164
1056477	129	122.112	20.9622	3.03159	32.112	152.692	-23.1147
1864962	53	161.971	158.096	21.4393	71.972	108.448	15.1455
2309938	141	158.697	210.139	22.9407	68.698	112.766	8.12682

continued on next page

Table C.1: *continued*

Event No.	Day	Zenith	Azimuth	Right Asc.	Declin.	Gal. Long.	Gal. Lat.
2718534	141	157.395	10.4207	13.8557	67.396	114.274	48.713
5391306	145	123.447	338.131	2.03713	33.447	139.492	-27.1381
1567237	145	142.3	26.1094	8.35667	52.299	166.332	34.679
3123122	54	135.79	187.858	0.230789	45.79	116.109	-16.5832
4953648	309	93.1463	178.728	8.16302	3.1463	219.227	18.8395
4833861	179	98.6532	7.95422	5.33362	8.6538	194.196	-15.8506
826017	183	114.913	274.009	18.3395	24.914	52.4777	17.5277
787075	269	100.09	1.08217	10.8143	10.091	237.583	56.4851
1735409	292	117.646	28.7132	14.3782	27.646	39.679	69.7658
610793	152	146.961	9.33852	6.28661	56.962	157.478	18.0611
70296	275	155.234	300.36	11.8441	65.233	132.917	50.7004
372857	126	124.389	10.8272	1.51721	34.39	132.158	-27.7714
1053797	150	122.096	185.512	20.3426	32.096	71.2429	-2.49706
3819978	151	133.192	186.99	8.41382	43.193	177.434	34.6978
4211145	152	130.055	357.352	22.7799	40.056	98.4899	-16.8271
2954433	152	135.142	24.7306	15.2372	45.142	74.8616	56.411
3926431	156	124.787	18.2815	19.6837	34.788	69.183	5.92664
3670860	158	176.157	357.468	6.03699	86.158	127.118	26.2476
4607462	164	129.998	35.6072	16.0199	39.997	63.6869	48.9583
1363912	166	139.995	216.736	14.4161	49.996	91.2074	60.9765
885675	173	166.465	206.238	22.3586	76.466	114.407	16.1432
399490	175	141.693	251.629	17.3146	51.694	78.7892	35.0723
1097197	176	167.594	197.697	23.9262	77.594	119.854	15.0574
408176	177	123.104	354.545	10.569	33.104	193.071	59.8534
5220970	58	153.045	84.629	14.2542	63.044	107.819	51.5545
913071	179	137.595	138.737	3.358	47.596	147.43	-8.0117
2171437	179	149.639	271.833	0.0453062	59.638	116.803	-2.65279
417433	182	171.043	24.434	8.98882	81.043	131.851	31.5872
2202190	182	125.29	330.485	20.4728	35.291	74.7933	-1.98939
2002836	184	154.896	23.2145	16.5194	64.896	96.3761	39.0398
3059438	185	146.129	189.682	9.78907	56.128	158.423	46.3043
425222	188	128.405	79.4708	2.48962	38.405	143.23	-20.5758
4894298	59	123.299	201.003	5.7198	33.298	176.009	1.83768
4075572	201	156.25	45.7807	17.3728	66.249	96.3534	33.5862
4138556	201	138.067	324.629	23.0636	48.066	104.988	-11.0206
2854432	59	137.534	223.96	20.4876	47.534	84.8377	5.02673
64253	207	143.11	235.106	8.6283	53.11	165.264	37.1289
4111686	210	150.249	307.375	23.8308	60.248	115.357	-1.71488

continued on next page

Table C.1: *continued*

Event No.	Day	Zenith	Azimuth	Right Asc.	Declin.	Gal. Long.	Gal. Lat.
2087472	214	120.195	24.368	14.3604	30.195	47.0933	70.0133
3997456	60	161.111	272.602	21.4773	71.111	107.941	14.4146
4145067	216	153.852	155.865	15.2623	63.852	100.751	46.5788
856749	218	140.844	62.9911	6.35342	50.844	163.622	16.2402
5110864	222	149.488	56.1135	23.9809	59.488	116.294	-2.70438
4243847	222	171.491	28.3012	21.9981	81.492	116.75	20.7624
2709871	224	176.473	250.805	0.302282	86.472	122.375	23.6364
3867415	224	165.116	148.894	12.355	75.115	125.524	41.8612
4222511	61	148.683	30.5095	14.4665	58.683	101.591	54.2615
1853106	226	133.986	17.3587	11.8046	43.985	155.858	68.8861
64573	227	136.021	108.244	21.9858	46.021	94.3862	-7.08417
2337283	240	120.53	32.9705	11.0818	30.53	198.272	66.4772
6098983	63	124.971	41.919	20.9042	34.971	77.7819	-6.37433
520134	242	143.055	326.37	7.23868	53.054	164.099	24.6923
1433197	242	150.6	14.3978	8.25326	60.601	156.329	33.6004
1475367	243	160.515	32.8441	7.30951	70.516	144.901	27.7059
2533885	243	121.846	207.008	0.640916	31.847	119.717	-30.9437
3184282	244	133.994	70.1213	13.1146	43.994	113.479	72.8497
2901500	245	169.415	218.291	2.15779	79.414	126.612	17.104
361286	249	166.849	146.637	19.1691	76.848	108.404	25.3096
1565795	251	133.659	252.689	17.9315	43.66	70.2445	27.9906
2608500	252	131.398	37.3156	13.3543	41.398	101.612	74.4727
3739618	253	151.265	65.919	16.8298	61.264	91.1583	38.056
2669207	254	137.968	120.066	8.14955	47.968	171.384	32.4432
2683260	262	149.29	41.8146	16.4415	59.29	89.6505	41.3539
3208799	262	124.04	117.457	13.8539	34.041	64.8501	75.414
2084416	263	165.734	157.953	6.00622	75.734	138.086	23.17
2517339	263	137.743	228.179	3.32563	47.743	147.072	-8.06635
3220315	264	161.142	259.754	4.38172	71.141	138.401	14.9419
44693	268	132.511	85.3651	1.62047	42.512	131.864	-19.5642
2324445	269	129.858	129.8	9.43899	39.859	182.527	46.0237
2258153	271	168.887	163.375	6.71026	78.888	135.322	26.1571
3480654	271	134.321	22.9178	21.7268	44.321	91.1674	-6.6618
3136000	273	164.347	125.861	13.6555	74.347	118.587	42.3748
2861464	276	174.331	50.2852	17.5915	84.33	116.81	28.8398
3671632	277	134.486	137.172	15.4986	44.486	72.2844	53.9604
4008483	279	139.526	86.3648	20.2842	49.527	85.3427	7.81967
2651168	280	162.562	323.052	22.6534	72.563	113.304	12.2111

continued on next page

Table C.1: *continued*

Event No.	Day	Zenith	Azimuth	Right Asc.	Declin.	Gal. Long.	Gal. Lat.
1857451	66	147.826	33.3165	6.31646	57.826	156.728	18.6075
3427166	282	127.943	193.846	10.9902	37.944	181.114	64.164
1096311	283	121.318	119.473	5.19273	31.319	173.936	-4.81381
1418387	284	159.005	205.53	0.995744	69.005	123.68	6.14532
1725932	284	126.853	194.835	3.13426	36.853	151.192	-18.4115
3374037	285	140.405	258.216	6.38258	50.404	164.157	16.3225
3874632	285	147.389	62.8537	21.6829	57.39	99.4284	3.4848
1664954	289	134.027	69.7203	11.2595	44.026	165.415	64.3758
3466077	289	151.402	13.6342	22.9863	61.401	109.913	1.39969
1310392	290	160.573	159.837	3.77554	70.574	136.563	12.4912
4382458	290	138.902	129.102	19.6751	48.901	81.7555	12.6684
5410121	294	121.747	149.504	22.5761	31.746	91.7093	-22.7004
2536284	296	126.207	325.892	22.3071	36.207	91.4141	-17.1325
6429891	69	146.453	180.277	13.1512	56.453	117.982	60.5054
4110705	302	130.748	75.1751	23.563	40.747	107.411	-19.7726
57191	70	158.269	41.6663	23.3167	68.268	114.514	6.92005
2509774	70	124.938	82.1295	5.7004	34.938	174.486	2.49464
6282589	71	154.629	18.7704	23.6704	64.629	115.395	2.80451
5920919	73	143.135	66.9792	18.7044	53.134	82.3995	22.7164
5698902	75	145.349	15.1174	22.1048	55.349	100.897	-0.293644
1609785	75	149.191	123.065	0.126581	59.192	117.335	-3.20246
2232184	75	159.834	321.926	13.2423	69.834	120.007	47.1629
4810010	78	149.455	215.072	6.01239	59.456	154.174	17.0664
2072549	78	159.076	106.921	3.0403	69.075	134.215	9.12375
5472179	81	170.453	109.519	16.3453	80.454	113.961	32.6759
1999164	82	120.813	2.15335	10.4443	30.813	197.517	58.2569
3524743	83	130.231	12.6894	15.889	40.231	64.2143	50.4391
5596961	84	143.014	284.446	6.00704	53.013	160.189	14.2421
4082255	85	128.548	317.197	21.4621	38.547	85.0109	-8.89183
2412334	85	143.407	147.669	2.32781	53.406	135.974	-7.21681
5035326	86	155.626	247.46	5.74957	65.626	147.514	18.0782
3797071	89	123.532	52.5594	14.1132	33.532	59.0376	72.5579
1295968	98	154.338	44.8634	23.1966	64.337	112.401	3.52183
5696224	99	146.038	47.3298	16.0931	56.038	86.6121	45.0236
4406198	99	156.654	66.2376	9.7716	66.655	145.409	41.4812
3147292	100	158.939	41.3477	7.24898	68.94	146.646	27.2751
177109	101	123.505	184.441	9.84895	33.505	192.254	50.8329
4439572	102	129.676	131.997	5.52849	39.676	169.381	3.30214

continued on next page

Table C.1: *continued*

Event No.	Day	Zenith	Azimuth	Right Asc.	Declin.	Gal. Long.	Gal. Lat.
5333094	102	142.091	279.244	23.0533	52.092	106.565	-7.30658
3664277	103	126.814	174.141	23.7658	36.815	108.604	-24.228
1299152	108	152.243	187.336	7.15014	62.243	153.981	25.8019
3162260	109	123.859	301.343	6.83024	33.858	181.954	14.4071
4527543	114	157.568	14.7274	11.0817	67.568	137.314	46.4733
3273134	115	137.238	79.2676	1.79792	47.237	132.778	-14.5529
4693634	52	131.124	12.3214	20.0266	41.125	76.7353	5.61608
5817674	118	139.43	131.618	9.6798	49.429	168.199	47.4097
2163722	119	138.996	125.817	19.0891	48.996	79.4179	17.981
5528885	120	127.795	194.466	4.24304	37.795	161.305	-9.50765
2085362	121	159.648	312.461	6.31243	69.647	144.819	22.5513
2905292	121	143.555	122.203	22.2365	53.556	100.803	-2.4207
4285190	123	125.971	226.02	21.1822	35.972	80.7908	-8.27848
5637104	123	146.497	100.812	10.7725	56.496	151.467	53.1408
1947477	125	139.734	59.6402	4.35191	49.735	153.743	-0.164507
5619504	126	129.597	32.6574	20.4216	39.598	77.9467	1.00716
1590528	128	158.527	91.5669	1.31642	68.526	125.461	5.78961
3465006	133	121.085	156.634	6.57829	31.086	183.189	10.3588
2846119	134	160.903	267.56	20.8551	70.904	105.731	16.5861
3385603	135	155.989	210.342	2.79084	65.989	134.369	5.72736
2719596	136	131.242	64.3973	9.91933	41.241	179.877	51.3916
4144367	137	154.042	52.8725	16.6696	64.042	94.9384	38.3964
5157441	138	125.1	140.605	14.9128	35.1	57.4674	62.5522
1530546	139	134.104	255.227	16.5842	44.105	69.1732	42.5018
4563241	143	166.371	318.581	0.2129	76.37	120.598	13.6738
2072713	145	123.969	39.2383	9.47048	33.97	191.038	46.1585
509647	156	147.296	108.069	23.065	57.295	108.775	-2.59088
1218145	162	142.613	155.97	17.9482	52.612	80.3379	29.3212
2533762	162	123.01	12.9421	9.09552	33.011	191.56	41.3864
129583	202	132.494	82.7558	2.27611	42.495	139.244	-17.6644
2248138	207	136.647	278.096	15.2755	46.647	77.1187	55.5009
3878658	154	107.64	250.316	4.93773	17.64	183.096	-15.684
1614328	55	98.233	246.564	14.7083	8.2336	2.40421	57.6405
4234847	260	94.2779	235.798	10.8853	4.278	246.694	53.6928
3187840	275	107.69	211.182	8.21673	17.689	205.338	25.721
1468281	87	106.451	1.69741	8.16384	16.451	206.281	24.5465
1695899	130	105.704	138.737	21.9214	15.705	72.6765	-29.503
2410775	175	104.149	255.26	1.77024	14.15	142.462	-46.6341

continued on next page

Table C.1: *continued*

Event No.	Day	Zenith	Azimuth	Right Asc.	Declin.	Gal. Long.	Gal. Lat.
4275575	177	111.038	242.994	10.5184	21.037	216.003	57.5039
1157143	58	110.335	359.308	5.40023	20.336	184.639	-8.75464
1958212	191	115.18	244.796	23.5113	25.18	100.748	-34.1891
2785061	191	114.482	9.49783	18.8892	24.483	55.1812	10.4982
3844587	59	102.902	237.665	23.1287	12.902	87.4741	-42.7173
3494149	218	117.069	67.8471	18.1695	27.069	53.7034	20.4522
89496	224	103.056	6.28428	4.69685	13.057	184.833	-21.1998
1573409	245	110.56	184.853	21.9905	20.56	77.3061	-26.6974
151289	63	103.682	96.5878	19.5542	13.682	49.8647	-2.81127
4345784	253	103.625	73.8732	19.1937	13.625	47.3358	1.7953
1025334	64	95.4781	46.7915	2.19093	5.4768	156.588	-52.0878
1368619	267	111.406	57.2781	9.52643	21.405	208.782	44.382
2511909	65	108.915	6.08652	10.3121	18.915	217.877	54.0619
1339798	272	108.599	229.173	22.3178	18.598	79.7922	-31.2274
466376	276	92.965	29.0428	7.85537	2.9645	217.177	14.6661
4061847	285	113.15	53.8064	23.1375	23.151	94.1161	-33.8825
3341036	292	112.202	96.5054	16.9966	22.202	42.5524	33.919
722405	78	119.118	155.778	18.6944	29.119	58.4208	14.7763
5398463	80	116.902	18.0288	21.0216	26.901	72.4634	-12.6923
5779172	83	108.961	253.134	8.69341	18.962	206.82	32.5042
2500629	83	107.072	208.59	22.7537	17.073	84.602	-36.2357
6034289	48	106.926	24.5054	0.791221	16.926	121.568	-45.9352
168983	85	116.767	27.241	1.69792	26.766	136.656	-34.758
2906243	85	107.019	251.371	21.2837	17.02	66.9352	-21.8076
2915911	85	113.801	355.43	14.3834	23.801	28.8846	69.0969
2969523	94	101.578	149.334	22.3898	11.578	75.1625	-37.2059
1133276	110	116.193	149.493	12.507	26.193	223.009	85.2126
2613026	112	103.375	267.95	11.0051	13.375	235.298	60.6348
2070666	121	100.491	204.552	13.4486	10.492	331.284	71.3839
1619568	123	101.221	215.951	11.0698	11.22	239.991	60.2093
3071680	126	108.714	282.529	18.4233	18.714	47.0441	13.997
5329687	128	109.357	218.532	8.19678	19.356	203.501	26.0776
3279091	129	101.059	192.747	0.590046	11.06	116.588	-51.6141
5696095	141	104.512	25.9007	0.248638	14.511	109.808	-47.428
1974873	143	108.255	195.406	22.3983	18.256	80.5738	-32.22

Appendix D

High Energy Neutrino Candidates

Table D.1: List of high energy neutrino events for the blind sample.

Event No.	Day	Zenith	Azimuth	Right Asc.	Declin.	Gal. Long.	Gal. Lat.
3878658	154	107.64	250.316	4.93773	17.64	183.096	-15.684
1614328	55	98.233	246.564	14.7083	8.2336	2.40421	57.6405
1157143	58	110.335	359.308	5.40023	20.336	184.639	-8.75464
70296	275	155.234	300.36	11.8441	65.233	132.917	50.7004

Table D.2: List of high energy neutrino events for the unblind sample.

Event No.	Day	Zenith	Azimuth	Right Asc.	Declin.	Gal. Long.	Gal. Lat.
4953648	309	93.1463	178.728	8.16302	3.1463	219.227	18.8395
1735409	292	117.646	28.7132	14.3782	27.646	39.679	69.7658
234639	266	100.749	258.897	14.8255	10.748	8.11754	57.7666
3593604	226	171.038	355.539	20.9636	81.038	114.693	22.1963
1760779	188	162.309	259.04	18.1623	72.308	102.969	28.905
1355187	147	169.176	279.881	14.8774	79.175	116.178	36.312

Table D.3: List of high energy neutrino events for the combined sample.

Event No.	Day	Zenith	Azimuth	Right Asc.	Declin.	Gal. Long.	Gal. Lat.
4953648	309	93.1463	178.728	8.16302	3.1463	219.227	18.8395
1735409	292	117.646	28.7132	14.3782	27.646	39.679	69.7658
234639	266	100.749	258.897	14.8255	10.748	8.11754	57.7666
3593604	226	171.038	355.539	20.9636	81.038	114.693	22.1963
1760779	188	162.309	259.04	18.1623	72.308	102.969	28.905
3878658	154	107.64	250.316	4.93773	17.64	183.096	-15.684
1614328	55	98.233	246.564	14.7083	8.2336	2.40421	57.6405
1157143	58	110.335	359.308	5.40023	20.336	184.639	-8.75464
70296	275	155.234	300.36	11.8441	65.233	132.917	50.7004